

MODELLING ULTRAFAST
DEMAGNETIZATION:
A REAL-SPACE TIGHT-BINDING APPROACH

Dissertation

zur Erlangung des Doktorgrades der Naturwissenschaften
(Dr. rer. nat.)

der

Naturwissenschaftlichen Fakultät II
Chemie, Physik und Mathematik

der Martin-Luther-Universität
Halle-Wittenberg

vorgelegt von

Franziska Ziolkowski

Erstgutachterin: Prof. Dr. Ingrid Mertig
Zweitgutachter: Prof. Dr. Steffen Trimper
Drittgutachterin: Prof. Dr. Bärbel Rethfeld

Datum der öffentlichen Verteidigung: 12.06.2024

Abstract

Ultrashort laser pulses impinging on magnetic materials generate a quenching of the magnetization on a subpicosecond time scale. To explain this rapid demagnetization various spin flip and spin transfer mechanisms are discussed in literature.

This work introduces a versatile computational approach to investigate such ultrafast magnetization dynamics by tuning the underlying mechanisms. The presented approach is based on a real-space tight-binding model and includes optical excitation as well as coupling to an external heat bath. The occupation matrix yields the system's observables and is evolved in time by the Lindblad equation.

The present study examines factors that promote efficient demagnetization: In the magnetic/nonmagnetic bilayer systems the demagnetization is dominated by the spin transport across the interface, while in homogeneous ferromagnetic systems spin transport from the front to the backside as well as initial disorder of the spin alignments yield important contributions to ultrafast demagnetization.

Ein ultrakurzer Laserpuls verursacht in einem magnetischen Material eine Entmagnetisierung innerhalb von weniger als einer Pikosekunde. In der Literatur werden verschiedenen Spin-Flip und Spin-Transport Mechanismen zur Erklärung dieses Phänomens diskutiert.

In der vorliegenden Arbeit wird ein flexibles Berechnungsverfahren vorgestellt, welches es ermöglicht diese ultraschnelle Magnetisierungsdynamik durch Manipulation der zugrundeliegenden Mechanismen zu untersuchen. Dieser Ansatz basiert auf der Tight-Binding-Methode im Realraum und beinhaltet sowohl optische Anregung als auch Kopplung an ein externes Wärmebad. Die Besetzungsmatrix enthält die Systemobservablen und wird mithilfe der Lindblad-Gleichung in der Zeit propagiert.

In dieser Arbeit werden verschiedene Einflussfaktoren auf eine ultraschnelle Demagnetisierung herausgearbeitet: In magnetisch-nichtmagnetischen Doppelschichten dominiert der Spintransport über die Grenzfläche die Demagnetisierung, wohingegen in homogenen Ferromagneten Spintransport von der Vorder- zur Rückseite der Probe, sowie eine Störung der kollinearen Ausrichtung der Spins zu Beginn der Simulation die Demagnetisierung begünstigen.

Contents

1. Ultrafast magnetization dynamics	1
1.1. Modelling ultrafast demagnetization	2
2. Constructing the system: electronic structure and density matrix	5
2.1. A real-space tight-binding approach	5
2.2. Optical excitation	10
2.3. Effective single-particle density matrix	20
3. Time evolution of a density matrix	31
3.1. Unitary time evolution and time evolution in open quantum systems .	31
3.2. Geometric derivation of the Lindblad equation	33
3.3. Microscopic derivation	38
3.4. The Lindblad equation for a d -level system	43
3.5. Charge and spin currents	47
4. Results	51
4.1. Technical and numerical details	51
4.2. Ferromagnetic/nonmagnetic heterostructures	53
4.3. Other material combinations	80
4.4. Ferromagnetic systems - extending the model	90
5. Summary	105
A. Additional derivations	107
A.1. Influence of the envelope function	107
A.2. Modifying the Rfield equation	108
B. Additional results	109
B.1. Polarization dependence	109
B.2. Frequency dependence	110
B.3. Interface currents	110
B.4. Noncollinear setups	111

1. Ultrafast magnetization dynamics

In recent years and especially in the last decade huge interest in ultrafast magnetization dynamics emerged. A wide palette of experiments was and is performed on this topic. Likewise, a multitude of explanatory approaches and simulations was delivered from the theory side. But what is so fascinating about this topic?

Magnetization dynamics is of general interest in information technology because it is linked to magnetic storage devices. The recording time of such a device is limited by the time for switching a magnetic subsystem. With magnetic field pulses switching times in the regime of several hundred picoseconds can be achieved [1]. Applying novel mechanisms this limit can be reduced only slightly farther until it reaches its ultimate limit of about 100 ps [2], [3].

Manipulation by optical pulses is a promising new method to overcome this time limit of magnetic switching. By using an ultrashort laser pulse a demagnetization can be achieved in less than a picosecond. This was first demonstrated in the famous experiment by Beaurepaire [4] in 1996. His results caught a lot of attention and lead to intense research in ultrafast demagnetization.

Just a few works shall be named here to represent the multitude of investigations. By utilizing ultrashort laser pulses also a reversal of an antiferromagnetic state can be achieved, as demonstrated by Radu et al. [5]. In ferromagnetic layers, switching of magnetic order within 7 ps by only one single laser pulse was achieved by Gorchon et al. in 2017 [6].

The generation of spin currents and spin torques is another promising field of ultrafast spin dynamics [7]. To this end magnetic/nonmagnetic bilayers are constructed. The interface acts as a source of spin current which is then converted into a transversal charge current via the inverse spin Hall effect. The transversal charge current emits a pulse of terahertz radiation [8]–[10]. This effect facilitates not only the detection of spin currents but is also the foundation for the development of new types of terahertz emitters [11], [12].

Ultrafast magnetization dynamics are not only interesting with respect to potential technical applications. They are also a worthwhile topic in order to understand fundamental physical processes [13]. The label “ultrafast” refers to the subpicosecond time regime. A typical ultrafast laser pulse has a duration from 10 fs up to 100 fs. Those are just slightly longer times than the period of visible light. And even more important: also microscopic processes and involving quasiparticles hap-

pen on those timescales. Therefore experiments on ultrafast magnetization dynamics deliver the necessary time resolution to open up the window towards observing and distinguishing those microscopic interactions.

Optical excitation and subsequent dynamics of demagnetization and relaxation towards the initial state cover multiple scales in terms of time as well as of space. This complicates simulations and theoretical models as they often apply only to their individual regime of time span and spatial extent. The discussion and understanding of ultrafast magnetization dynamics has to include different approaches and provides no simple answers. After a decade of intense research it still remains a highly interesting topic.

In this work a simulation scheme for the dynamics of heterogeneous systems will be presented. To this end a real-space tight-binding model will be introduced in Chapter 2, which includes the coupling to an electromagnetic field as a main ingredient for ultrafast optical excitation. An occupation matrix will be used to track the system's temporal evolution.

Chapter 3 deals with the actual time evolution of the occupation matrix. The Lindblad equation will be derived and adapted to the problem. Furthermore, we will formulate charge and spin currents within the model.

In Chapter 4 finally the results will be presented.

The remainder of Chapter 1 gives an overview over processes during optical excitation, how they result in ultrafast demagnetization and how they can be simulated and described theoretically.

1.1. Modelling ultrafast demagnetization

To describe the events during optical excitation, at first we examine the energy changes in the electronic subsystem. This consideration does not explain the observed phenomena but provides an initial image and overview about laser-induced changes. A laser pulse excites electrons from lower to higher energy levels according to selection rules. This excitation process happens as long as the pulse irradiates the sample - for 10 fs up to 100 fs. Directly during and shortly after the laser excitation this results in a highly unthermal distribution of the electrons. The demagnetization sets in as soon as electrons are excited by the laser pulse. It reaches its maximum between several femtoseconds and about 1 ps after the pulse peak. After laser excitation the excited electrons thermalize towards a high temperature Fermi-Dirac distribution. Depending on the system this can take from 15 fs up to 150 fs [14]. The increase of electronic temperature corresponds to the energy transferred from the laser to the electronic system. By electron-phonon interactions energy is transferred from the electrons to the lattice. The lattice and the electron temperatures equilibrate. Subsequently both systems cool down again and the electronic occupation returns to its initial ambient temperature Fermi-Dirac distribution. During these events also the lattice is heated up locally before it cools down again together with the remagnetization of the electronic system. The remagnetization depends on the

excited material, the applied laser fluence and the electric field but takes at most 1 ns [15].

Pathways of demagnetization

The timescale of demagnetization, setting in directly with the laser pulse, inspires the question, whether the laser light directly manipulates the electronic spin state. Indeed, the coupling between electron spin and the magnetic field associated with the laser pulse is by far too weak to be responsible for just a fraction of the observed demagnetization (cf. Section 2.2.1). Other pathways have to be responsible for the angular momentum change during ultrafast demagnetization.

Two main questions arise with respect to the demagnetization and their answers differ from material to material and also between the different modeling approaches: Is the demagnetization governed mainly by spin flip or spin transfer processes [16], [17]? And second, is the quenching of magnetization better described by a reduction of exchange splitting or by magnon generation [18], [19]? While the first mechanism belongs to itinerant magnetism, the second one belongs to the localized magnetism in the Heisenberg picture. In the studied materials itinerant as well as localized magnetic moments are present and both mechanisms are not easy to disentangle. In the context of itinerant magnetism spin flips reduce the magnetization. This quenches a magnetization dependent exchange splitting, which further reduces the magnetization resulting in a feedback effect [20]. These local spin flips are explained by the occupation profile after excitation, which enables the impact of spin-orbit coupling. The spin momentum is thereby transferred to the orbital angular momentum of the electron. The orbital angular momentum is then ultimately transferred to the lattice by interaction of electrons with the crystal potential [21]. The spin-orbit coupling is thus the main ingredient of global demagnetization.

Nevertheless, spatial redistribution and spin transport are discussed as dominant and fastest processes of local demagnetization. Globally the angular momentum is quenched more slowly by subsequent spin flip processes. In this context, redistribution means an exchange of angular momentum between neighboring sites with different spin polarization for example in alloys or at interfaces [22], [23], whereas spin currents describe this relocation of momentum on a larger length scale. They are often discussed in connection with spin-flip scattering events in which the spin momentum is transferred to phonons or magnons [24], [25].

In the Heisenberg picture the magnetic moments are localized. The demagnetization manifests in an enhanced tilting of the moments with respect to the global magnetization axis. The orientation of localized moments is perturbed either in form of a collective excitation, a magnon [19], [26]–[28]; or as random spin fluctuations connected with a breakdown of nearest neighbor spin correlation [21].

This diversity of mechanisms is hard to be united in a single theoretical framework. Therefore a theoretical model usually concentrates on only some of the mentioned mechanisms. For example it captures the dynamics of either local processes or spin currents in a better way. All the more it is important to regard the scope and

approximations included in the respective approach.

Approaches to model ultrafast magnetization dynamics

The multitude of possible mechanisms of demagnetization complicates the choice of a theoretical framework and also reversely the applied framework affects the possibility to observe a certain mechanism.

A descriptive approach is the three-temperature model (3TM). It focuses on the energy transfer between the subsystems. The 3TM describes the electronic, phononic and spin system and their interactions by means of temperatures and transfer rates [29]. The 3TM is also used in connection with atomistic spin dynamics simulations. They describe the dynamics of the spin system via the Landau-Lifshitz-Gilbert equation and are also used in connection with semiclassical transport equations [28]. With this method large inhomogeneous systems can be treated and demagnetization rates can be reproduced very accurately, if realistic approximations of heat transfer rates calculated from microscopic scattering rates are available. However, the concept of temperature is highly questionable during excitation and shortly after due to the nonthermal distribution of electronic occupation. Furthermore both approaches do not address the microscopic pathways of the angular momentum.

Semiclassical approaches are focused on propagation and scattering by applying the Boltzmann transport equation [14], [30], a wave-diffusion equation [31] or a superdiffusive transport equation [32], [33]. The dynamics of hot carrier density is used to calculate spin currents and changes of magnetization. Spin-dependent scattering rates and spin-dependent reflectivity of the interface is taken into account. Therefore these methods are suitable for large systems and in materials with a strong contribution from spin transport to demagnetization. Also interfaces can be treated realistically. Due to a coarse resolution of the electronic distribution in \mathbf{k} -space and of the optical excitation which is included as an effective source term, these methods yield only limited microscopic insights.

A microscopically detailed treatment is realized by time-dependent density functional theory [34] and by exact many-body time propagation [21], [35]. Both methods include the coupling to laser light explicitly, offer insights into microscopic processes and are almost parameter-free. On the other hand they are computationally demanding and hence limited with respect to accessible system size and time span. Therefore they are optimal to reproduce local processes in small systems, but less favorable to simulate extended phenomena like magnons or spin currents.

The method of choice in this work is a real-space tight-binding Hamiltonian. Contrary to TDDFT and many-body calculations it is not parameter-free but it offers insights into microscopic processes as well as the access to spin currents through inhomogeneous systems composed of up to 100 atoms. With the coupling to an external heat bath relaxation is included into the time evolution of the system, which can be calculated for up to several picoseconds.

2. Constructing the system: electronic structure and density matrix

It is one goal of this work to simulate the time evolution of electrons in a metallic heterostructure subsequent to manipulation by a laser beam. Due to the optical excitation the electron system is elevated to a higher energy state, which is displayed by a change in the electronic structure. Within our model we will not account for the excited energy levels explicitly but rather track their changes in terms of a modified occupation of the atomic orbitals (cf. Section 2.2.6). Within the local basis the occupation translates directly into the physical quantities – magnetization and orbital occupation. Moreover the occupation matrix enables to include the coupling to an external heat bath. This allows to simulate the loss of energy and remagnetization after laser excitation. Taken together there are two main foundations of our model: The Hamiltonian and the occupation matrix.

We will study the time evolution of the system in terms of its occupation or density matrix. The propagation in form of a differential equation will be derived in Chapter 3. But beforehand, within the present chapter, some basic concepts will be introduced. We will start in Section 2.1 with describing the electronic structure of the system. In Section 2.2 we will present two different approaches to incorporate the optical excitation. Finally, the concept of the occupation matrix will be introduced in Section 2.3.

2.1. A real-space tight-binding approach

In order to characterize the electronic system with its eigenstates and eigenenergies a real-space tight-binding approach is used. We plan to study magnetization dynamics in extended real-space clusters composed of various atomic species. Furthermore, the approach shall enable a flexible geometry of the system, like chains or flakes, and local inhomogeneities, for example interfaces. Therefore many of the investigated systems will have at least one open boundary¹ and thus a reciprocal space cannot be defined in the corresponding direction. Quantities will just be discussed concerning their spatial dependence. That is why the usual formulation of the tight-binding

¹In this work an open boundary indicates a material-vacuum border, in analogy to open and closed circuits.

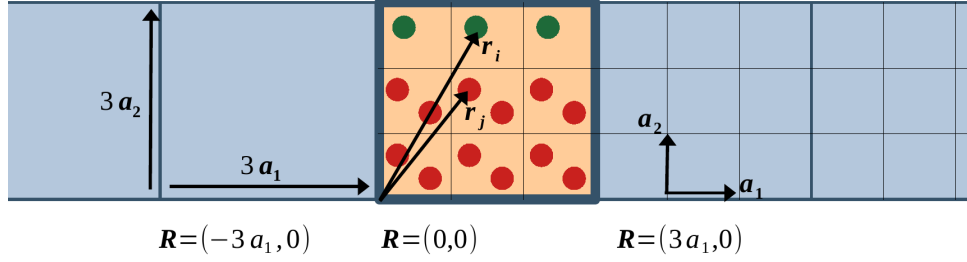


Figure 2.1.: Sketch of a cluster for simplicity in two dimensions. A unit cell is spanned by vectors \mathbf{a}_1 and \mathbf{a}_2 . In this example three times three unit cells form a supercell (highlighted in orange). This supercell at $\mathbf{R} = 0$ is repeated along the directions of periodicity, in the present case just \mathbf{a}_1 .

formalism in reciprocal space is omitted in the following, even though the common introduction is motivated by facilitating the calculation of wave-vector-dependent quantities.

The structure of a cluster is sketched in Figure 2.1. The real-space model contains N atoms at positions \mathbf{r}_i , $i = 1, \dots, N$. These atoms are arranged in unit cells, which form a finite supercell. A unit cell is spanned by the lattice vectors \mathbf{a}_1 , \mathbf{a}_2 and \mathbf{a}_3 . The supercell has an extent of a specified number of unit cells n_1 , n_2 and n_3 along the corresponding lattice vectors. Accordingly the supercell lattice vectors are $n_1\mathbf{a}_1$, $n_2\mathbf{a}_2$ and $n_3\mathbf{a}_3$. If periodicity is applied along a specific direction, the whole supercell together with all the atoms is identically repeated along those supercell vectors. A combination of these new lattice vectors defines the position $\mathbf{R}_i = (i_1 \cdot n_1\mathbf{a}_1, i_2 \cdot n_2\mathbf{a}_2, i_3 \cdot n_3\mathbf{a}_3)$ of a supercell within the superlattice. If open boundaries are applied along a specific direction, the respective factors i_1 , i_2 or i_3 have to be zero. In most simulations the system is finite at least along one of the spatial directions. Our calculations apply to the cluster at $\mathbf{R} = 0$, which in general can also be finite along every direction.

Atomic orbitals $\phi_\alpha(\mathbf{r}) = \phi_{l\sigma}(\mathbf{r} - \mathbf{r}_a)$ are centered at each site within the system. The multi-index $\alpha = (a, l, \sigma)$ comprises their position \mathbf{r}_a within the supercell, their spin character $\sigma = \uparrow, \downarrow$ and their orbital index l . The spin quantization axis is aligned parallel to the z -axis and the orbital index contains information about the geometrical shape and orientation of the orbital. Within the scope of this work s , p and d orbitals are included. This sums up to a basis set of $N_{\text{tot}} = 18 \cdot N$ atomic orbitals within the supercell at $\mathbf{R} = 0$. These atomic orbitals provide an intuitive basis set to express a wave function of the total system

$$\psi_n(\mathbf{r}) = \frac{1}{\sqrt{\tilde{N}}} \sum_{\mathbf{R}_i} \sum_{\alpha} c_{n,\alpha} \phi_\alpha(\mathbf{r} - \mathbf{R}_i) . \quad (2.1)$$

The normalization condition is ensured by the prefactor if the number of supercells \tilde{N} goes to infinity in case of periodicity. An electronic state $|\psi_n\rangle$ within the cluster is localized with the weighting factor $c_{n,\alpha}$ in the respective atomic orbital $|\phi_\alpha\rangle$.

The ansatz (2.1) is therefore a *linear combination of atomic orbitals* (LCAO) and is based on the assumption of strongly attractive core potentials. This justifies the use of localized orbitals as an appropriate basis set, which is required to fulfill the normalization and orthogonality condition

$$\langle \phi_{\alpha, \mathbf{R}_i} | \phi_{\beta, \mathbf{R}_j} \rangle = \delta_{\alpha, \beta} \delta_{\mathbf{R}_i, \mathbf{R}_j} , \quad (2.2)$$

where $|\phi_{\alpha, \mathbf{R}_i}\rangle$ is given by $\phi_{\alpha}(\mathbf{r} - \mathbf{R}_i) = \langle \mathbf{r} | \phi_{\alpha, \mathbf{R}_i} \rangle$.

The number of states in the system coincides with the number of basis orbitals. In excited systems enough high energy orbitals have to be included into the basis set to sufficiently represent higher energy states. The wave functions $|\psi_n\rangle$ are the systems' eigenstates with the corresponding eigenenergy \mathcal{E}_n

$$\hat{H} |\psi_n\rangle = \mathcal{E}_n |\psi_n\rangle . \quad (2.3)$$

The Hamiltonian

$$\hat{H} = \hat{V}_{\text{pot}} + \frac{\hat{\mathbf{p}}^2}{2m} \quad (2.4)$$

describes an electron with momentum $\hat{\mathbf{p}}$ in a crystal potential \hat{V}_{pot} . Its eigenvalues are the eigenenergies

$$\mathcal{E}_n = \frac{1}{\tilde{N}} \sum_{\alpha, \beta} c_{n, \alpha}^* c_{n, \beta} \sum_{\mathbf{R}_i, \mathbf{R}_j} \langle \phi_{\alpha, \mathbf{R}_i} | \hat{H} | \phi_{\beta, \mathbf{R}_j} \rangle . \quad (2.5)$$

Due to the periodicity the summation over \mathbf{R}_i yields \tilde{N} identical contributions and can be omitted. Just the distance vector $\delta \mathbf{R} = \mathbf{R}_i - \mathbf{R}_j$ is relevant. Hamiltonian and atomic orbitals are now condensed into the tight-binding matrix elements

$$\mathcal{H}_{\alpha, \beta}^{TB} = \sum_{\delta \mathbf{R}} \langle \phi_{\alpha, \mathbf{0}} | \hat{H} | \phi_{\beta, \delta \mathbf{R}} \rangle , \quad \alpha, \beta \in \{1, \dots, N_{\text{tot}}\} . \quad (2.6)$$

The weighting coefficients are combined into a coefficient vector

$$\mathbf{c}_n = (c_{n, \alpha})_{\alpha=1, \dots, N_{\text{tot}}} . \quad (2.7)$$

As a consequence of the normalization of the wave functions $|\psi_n\rangle$ and the basis functions $|\phi_{\alpha, \mathbf{R}_i}\rangle$ the set of vectors \mathbf{c}_n as well has to fulfill the orthogonality and normalization condition

$$\mathbf{c}_n^\dagger \cdot \mathbf{c}_m = \delta_{n, m} \quad \text{and} \quad \sum_{\alpha} |c_{n, \alpha}|^2 = 1 \quad \text{for all } n, m \in \{1, \dots, N_{\text{tot}}\} . \quad (2.8)$$

By using the tight-binding matrix, the equation of energy eigenvalues (2.5) is transformed to

$$\sum_{\alpha \beta} c_{n, \alpha}^* \mathcal{E}_n c_{n, \beta} - c_{n, \alpha}^* \mathcal{H}_{\alpha \beta}^{TB} c_{n, \beta} = 0 \quad (2.9)$$

and can finally be mapped to the following matrix eigenvalue problem

$$\mathcal{H}^{TB} \mathbf{c}_n = \mathcal{E}_n \mathbf{c}_n . \quad (2.10)$$

With the knowledge of the tight-binding matrix \mathcal{H}^{TB} this can be solved numerically.

To determine its matrix elements (2.6) is however not a trivial problem. It involves knowledge of the spatial dependence of the atomic orbitals $\phi_\alpha(\mathbf{r})$ to perform the corresponding integration. Therefore Slater and Koster introduced a method to decompose the resulting integrals into several constants, the Slater-Koster parameters [36]. By postulating periodicity and extending the above definitions and equations to \mathbf{k} -space, a tight-binding band structure can be calculated and compared to an *ab initio* band structure at selected \mathbf{k} -points. The Slater-Koster parameters are then optimized to minimize the deviation between *ab initio* and tight-binding energy eigenvalues at selected \mathbf{k} -points.

To reduce the number of necessary parameters several approximations have to be performed. The first one is to consider only a finite number of atomic orbitals ϕ_α , as has been discussed before. In a next step a cutoff radius is introduced to the range of interaction. The atomic orbitals are of Slater-type and their radial part $\sim r^{n-1}e^{-\zeta r}$ decays exponentially at long distances [37]. With this also the summands in (2.6) decay rapidly with increasing distance $\mathbf{d} = (\mathbf{r}_b + \delta\mathbf{R} - \mathbf{r}_a)$. Therefore the interaction between far apart orbitals can be neglected. Usually the sum (2.6) is restricted to include on-site contributions and the interactions between first and second nearest neighbors. These three types of interaction were also taken into account within this work.

Now the orbital symmetry will be exploited to further reduce the number of necessary parameters. For this analysis the Hamiltonian $\hat{H}(\mathbf{r})$ is decomposed into a sum of localized atomic potentials. Different scenarios of relative position between the atomic potential at and orbital centers at \mathbf{r}_a and \mathbf{r}_b are distinguished. If all three are located at the same position the corresponding summand in (2.6) is called an on-site contribution. Such contributions can be expressed by using merely six on-site energies E_s^σ , E_p^σ and E_d^σ for each atomic species in the cluster. Interactions between orbitals of different type $\alpha \neq \beta$ at the same position vanish due to orthogonality. In another configuration both orbitals are centered at different positions but the potential is located at one of those positions. This is called a two-center integral. The three-center integral with both orbital centers as well as the potential located at different positions will be neglected. Also a two-center integral with both orbitals at the same position but the potential at a different position will be neglected.

The left over type of a two-center integral between orbitals α and β is expressed in terms of $(\alpha\beta\gamma)$, the Slater-Koster parameters [38], [39]. In doing so the integral is split into different contributions according to the orientation of the overlap region with respect to the connecting axis \mathbf{d} , the distance vector between both orbitals. This orientation determines the type of the bond $\gamma = \{\sigma, \pi, \delta, \dots\}$. The orbitals α and β are construed into their fractions orthogonal and parallel to \mathbf{d} . Their orientation in relation to this axis can be expressed by the direction cosines

$$k = \mathbf{e}_x \cdot \frac{\mathbf{d}}{|\mathbf{d}|}, \quad l = \mathbf{e}_y \cdot \frac{\mathbf{d}}{|\mathbf{d}|}, \quad m = \mathbf{e}_z \cdot \frac{\mathbf{d}}{|\mathbf{d}|}. \quad (2.11)$$

Different matrix elements (2.6) can now be expressed by combinations of a relatively

small set of parameters. For example it is

$$\langle p_x^\uparrow | \hat{H} | p_y^\uparrow \rangle = kl(p^\uparrow p^\uparrow \sigma) - kl(p^\uparrow p^\uparrow \pi) . \quad (2.12)$$

Tables of those matrix elements in terms of Slater-Koster parameters can be found in [36], [38], [40].

Collinear ferromagnetic materials are usually simulated by spin-split on-site energies. In addition we will also use spin-dependent Slater-Koster parameters. In this way it is possible to simulate not just a rigid energy shift between bands of different spin character but also different band shapes. Applied to the discussed real-space model this translates to spin-dependent group velocities.

Up to this point we considered the interaction of both orbitals within the crystal potential but disregarded any relativistic effects. Spin-orbit coupling (SOC) however introduces spin-mixing to the system by coupling orbitals of opposite spin character and is therefore an essential ingredient for modeling demagnetization. It also significantly affects the electronic band structure and symmetry of the system. In Ref. [41] Jaffe and Singh introduced a method to include a spin-orbit coupling correction to the tight-binding formalism. On this account a term has to be added to the tight-binding Hamiltonian (2.4)

$$\hat{H}_{tot} = \hat{H} + \hat{H}_{SOC} . \quad (2.13)$$

Within the present model only on-site contribution of the SOC will be considered. Furthermore a centrosymmetric potential is assumed, so that the strength of the spin-orbit interaction only depends on the relative orientation of spin and orbital momentum

$$\hat{H}_{SOC} = \lambda \hat{\mathbf{L}} \cdot \hat{\mathbf{s}} . \quad (2.14)$$

In a simple picture, the SOC arises due to the circular motion of the electron inside the gradient of the atomic potential. The parameter λ quantifies this interaction and can be flexibly tuned within this model. Usually it is proportional to the atomic number and increases rapidly for strongly localized orbitals. Therefore a large SOC effect is to be expected especially in d orbitals of heavy atoms, like Cu, Co and Pt - the materials of interest within this work.

The extension of the Hamiltonian yields new matrix elements. In this work all SOC contributions between orbitals located at different sites will be neglected and just matrix elements with both orbitals and the potential centered at the same site will be taken into account. To evaluate the contributions

$$(\mathcal{H}^{SOC})_{\alpha,\beta} = \langle \phi_\alpha | \hat{H}_{so} | \phi_\beta \rangle, \quad \alpha, \beta = 1, \dots, N_{tot} \quad (2.15)$$

the respective orbitals are expressed as a sum of spherical harmonics to evaluate the product $\hat{\mathbf{L}} \cdot \hat{\mathbf{s}}$. All relevant matrix elements for p , d and even f orbitals can be found for example in Ref. [42]. The effect vanishes in case of s orbitals due to their orbital angular momentum of $l = 0$.

The resulting Hamiltonian contains the tight-binding matrix as well as SOC matrix elements (2.15)

$$\mathcal{H}_{tot} = \mathcal{H}^{TB} + \mathcal{H}^{SOC} . \quad (2.16)$$

All matrices are structured with respect to spin and orbital character

$$\mathcal{H}^{\sigma\sigma'} = \langle l\sigma | \hat{H} | l'\sigma' \rangle \in \mathbb{C}^{9 \times 9}, \quad l, l' \in \{s, p_x, p_y, p_z, d_{xy}, d_{yz}, d_{zx}, d_{x^2-y^2}, d_{z^2}\} \quad (2.17)$$

$$\mathcal{H} = \begin{pmatrix} \mathcal{H}^{\uparrow\uparrow} & \mathcal{H}^{\uparrow\downarrow} \\ \mathcal{H}^{\downarrow\uparrow} & \mathcal{H}^{\downarrow\downarrow} \end{pmatrix} \quad (2.18)$$

The eigenvalue problem (2.10) is solved for the extended Hamiltonian (2.16) to get the corresponding eigenvector coefficients.

2.2. Optical excitation

To account for an optical excitation the vector potential $\mathbf{A}(\mathbf{r}, t)$ is a representation of the laser light. The electric field associated with the vector potential yields an additional contribution to the electron's momentum operator whereas the magnetic field component interacts with the electron's spin. An electron exposed to an electromagnetic field is described by the following time-dependent Hamiltonian [43]²

$$\hat{H}(\mathbf{r}, \hat{\mathbf{p}}, t) = V_{pot}(\mathbf{r}, (\hat{\mathbf{p}} - e\mathbf{A}(\mathbf{r}, t))) + \frac{(\hat{\mathbf{p}} - e\mathbf{A}(\mathbf{r}, t))^2}{2m} - \frac{e}{m} \hat{\mathbf{s}} \cdot \mathbf{B}(\mathbf{r}, t) . \quad (2.19)$$

In a first step we will neglect the last term, the interaction of laser light and spin momentum. This omission will be justified in the next section. With this simplification the remainder of the Hamiltonian (2.19) can be expressed in terms of the unperturbed Hamiltonian

$$\hat{H}_0(\mathbf{r}, \hat{\mathbf{p}}) = V_{pot}(\mathbf{r}, \hat{\mathbf{p}}) + \frac{\hat{\mathbf{p}}^2}{2m} . \quad (2.20)$$

It will be the general form of the time-independent Hamiltonian introduced in (2.13) during the course of this and the following sections. By performing

$$\hat{\mathbf{p}} \rightarrow \hat{\mathbf{p}} - e\mathbf{A} , \quad (2.21)$$

the canonical momentum is replaced by the kinetic momentum to account for the field momentum $e\mathbf{A}$. The time-dependent Hamiltonian emerges now from \hat{H}_0 by performing substitution (2.21)

$$\hat{H}(\mathbf{r}, \hat{\mathbf{p}}, t) = \hat{H}_0(\mathbf{r}, \hat{\mathbf{p}} - e\mathbf{A}(t)) = V_{pot}(\mathbf{r}, (\hat{\mathbf{p}} - e\mathbf{A}(\mathbf{r}, t))) + \frac{(\hat{\mathbf{p}} - e\mathbf{A}(\mathbf{r}, t))^2}{2m} . \quad (2.22)$$

This procedure is called minimal coupling [44] or, in the context of a tight-binding framework, the Peierls substitution [45], [46]. It is the most simple way to couple

²The charge of the electron is $e = -|e_0|$.

an electromagnetic field to charged matter while being gauge invariant. Because in the following all higher order interactions between electron and electromagnetic radiation will be neglected, it is indeed a minimal coupling. By omitting the last term of (2.19) we already neglected all magnetic dipole and multipole transitions and in the following we will also neglect electric multipole transitions and solely consider electric dipole transitions. The necessary approximations and premises will be presented in the following section. The derivations presented therein and in Section 2.2.2 are mainly guided by Ref. [47] and Ref. [43] but can be found in many textbooks.

We will introduce two different methods to derive the time-dependent perturbed Hamiltonian (2.22). In the first method the transition from \hat{H}_0 to \hat{H} will be realized by straightforwardly performing the replacement of momenta (2.21). This method can be applied in case of a momentum-independent crystal potential $V_{pot}(\mathbf{r})$. While in the second approach a unitary transformation will be performed to transform \hat{H}_0 allowing also for momentum-dependent potentials like in (2.22). But beforehand the electric dipole approximation will be introduced by some considerations concerning the vector potential of the laser pulse. In the last part of this section the evaluation of the optical transition matrix elements within our model system will be demonstrated and resulting selection rules will be discussed.

2.2.1. The electric dipole approximation

In the following the electric dipole approximation will be derived to express the excitation of the ground state system by the laser pulse. For now we assume monochromatic laser light in vacuum with a well-defined frequency ν and the corresponding radial frequency $\omega = 2\pi\nu$. In that case the wave equation for \mathbf{A} simplifies to the Helmholtz equation

$$\nabla^2 \mathbf{A} + \mathbf{k}^2 \mathbf{A} = 0 . \quad (2.23)$$

A solution of the Helmholtz equation is a set of plane waves with frequency ω travelling in \mathbf{k} -direction. The vector potential can now be written as

$$\mathbf{A}(\mathbf{r}, t) = \frac{A_0 \boldsymbol{\epsilon}}{2} \left(e^{i(\mathbf{k} \cdot \mathbf{r} - \omega t + \phi)} + e^{-i(\mathbf{k} \cdot \mathbf{r} - \omega t + \phi)} \right) , \quad (2.24)$$

with A_0 being the amplitude, $\boldsymbol{\epsilon}$ the polarization vector of the laser field and an arbitrary phase ϕ . The Coulomb gauge $\nabla \cdot \mathbf{A} = 0$ yields $\mathbf{E} = -\partial_t \mathbf{A}$. Therewith the electric field can be written as

$$\mathbf{E}(\mathbf{r}, t) = \frac{i\omega A_0 \boldsymbol{\epsilon}}{2} \left(e^{i(\mathbf{k} \cdot \mathbf{r} - \omega t + \phi)} - e^{-i(\mathbf{k} \cdot \mathbf{r} - \omega t + \phi)} \right) . \quad (2.25)$$

Its amplitude can be expressed in terms of the amplitude of the vector potential $E_0 = i\omega A_0$. Similarly the magnetic field is given by $\mathbf{B} = \nabla \times \mathbf{A}$ and its amplitude is $B_0 = ikA_0$. The comparison of magnetic and electric field amplitudes yields $\frac{B_0}{E_0} = \frac{1}{c}$. The magnetic field amplitude of the laser light scales with the inverse speed of light in comparison with the electric field amplitude. Therefore the interaction of laser light and spin momentum is significantly weaker and is neglected in most simulations

concerning ultrafast demagnetization. This interaction would allow for a change of the spin during the optical transition. However, TDDFT calculations that accounted for a coupling between spin and magnetic field did not show a notable change of the magnetization dynamics due to the additional term [48]. Neglecting the spin of the electron in optical excitation is thus the first important simplification on the way to the electric dipole approximation.

To further simplify the interactions the exponential in (2.24) is expanded to

$$e^{i\mathbf{k}\cdot\mathbf{r}} = 1 + i\mathbf{k}\cdot\mathbf{r} + \mathcal{O}(\mathbf{k}\cdot\mathbf{r})^2 . \quad (2.26)$$

The argument of the exponential can be estimated by means of the Bohr radius and the laser wave length

$$|\mathbf{k}\cdot\mathbf{r}| = \frac{2\pi a_0}{\lambda} \ll 1 . \quad (2.27)$$

Common laser light has a wave length of several hundreds of nm whereas the Bohr radius is just about 0.05 nm. In other words, the spatial variation of the laser field can be neglected on the range of an atom. Even throughout the total cluster within our simulation, which has an extent of less than 10 nm, the laser field can be treated as homogeneous. Therefore the exponential (2.26) can be truncated after the first term. As a consequence the interaction between electric field and all higher multipole moments is neglected. Only a coupling between the electric field and the electric dipole is considered. In pursuance of this approximation the vector potential loses its spatial dependence and becomes

$$\mathbf{A}(t) = A_0\boldsymbol{\epsilon} \cos(\omega t + \phi) . \quad (2.28)$$

Now the matrix elements of $\hat{\mathbf{p}}\cdot\mathbf{A}$, the interaction of the momenta, can be transformed to the electric dipole interaction $\hat{\boldsymbol{\mu}}\cdot\mathbf{E} = e\hat{\mathbf{r}}\cdot\mathbf{E}$, as demonstrated later on in equations (2.33) and (2.34). The resulting electric dipole formulation is eponymous for the presented approximation. The underlying physical process is the interaction of the laser light with the electric charges within an atom. The light induces a dipole moment which again interacts with the electric field component of the laser light. The interacting electric dipole moment has to be generated by the laser light initially, because any initial permanent electric dipole moment is precluded by the symmetry of the atomic wavefunctions. Within the electric dipole approximation the coupling between laser field and higher atomic multipoles is neglected. Therefore the selection rules derived in Section 2.2.4 are just valid in the context of the presented approximations.

2.2.2. Minimal coupling by replacement

To derive an expression for the optical perturbation we start with a simplified version of the time-dependent Hamiltonian (2.22)

$$\hat{H}(t) = \hat{V}_{pot}(\mathbf{r}) + \frac{1}{2m} (\hat{\mathbf{p}} - e\mathbf{A}(t))^2 . \quad (2.29)$$

The dependence of the crystal potential on momentum is omitted, because it lies outside the scope of our model. The expansion of the squared term results in a term that is second-order in the vector potential \mathbf{A} . To estimate the impact of this term we will utilize the amplitudes presented in (2.24) and (2.25). Analyzing the ratio of momentum and vector potential amplitude yields

$$\frac{eA_0}{p} \approx \frac{eE_0a_0}{\hbar\omega} . \quad (2.30)$$

The momentum is estimated based on the ground state of the hydrogen atom as $p = \hbar/a_0$ by means of the Bohr radius a_0 . The denominator represents the energy of the laser light, which is usually larger than 1 eV. The numerator depends on the amplitude of the electric field and can be estimated to about 10^{-2} eV. In comparison with the remainder of equation (2.29) the term $\propto e^2A_0^2$ becomes only important for high laser intensities and in highly excited states with a small energy spacing. Hence it will be omitted in the rest of this work.

To evaluate the remainder of the squared term in (2.29) the Coulomb gauge again proves favorable. Since within this gauge momentum operator $\hat{\mathbf{p}}$ and vector potential \mathbf{A} commute and the mixed terms can be merged. The resulting expression for the time-dependent Hamiltonian is the sum of the ground state Hamiltonian \hat{H}_0 (2.16) and a time-dependent perturbative term $\hat{H}_L(t)$

$$\hat{H}(\mathbf{r}, t) = \underbrace{\hat{V}_{pot}(\mathbf{r})}_{\hat{H}_0} + \underbrace{\frac{\hat{\mathbf{p}}^2}{2m} + \frac{-\hat{\mathbf{p}} \cdot e\mathbf{A}(t)}{m}}_{\hat{H}_L(t)} . \quad (2.31)$$

At this point we apply the result of the electric dipole approximation (2.28) and the matrix elements of the time-dependent term in (2.31) accordingly simplify to

$$\langle \psi_f | \hat{H}_L(t) | \psi_i \rangle = \langle \psi_f | \hat{\mathbf{p}} | \psi_i \rangle \cdot \epsilon \frac{-eA_0}{m} \cos(\omega t + \phi) . \quad (2.32)$$

They describe a transition from an initial state ψ_i to a final state ψ_f in consequence of the optical excitation. With the aid of the Heisenberg equation the momentum operator can be rewritten as

$$\hat{\mathbf{p}} = m \frac{d\hat{\mathbf{r}}}{dt} = \frac{im}{\hbar} [H_0, \hat{\mathbf{r}}] \quad (2.33)$$

to evaluate its matrix elements

$$\langle \psi_f | \hat{\mathbf{p}} | \psi_i \rangle = \frac{im}{\hbar} (\mathcal{E}_f - \mathcal{E}_i) \langle \psi_f | \hat{\mathbf{r}} | \psi_i \rangle . \quad (2.34)$$

The energy spacing defines the transition frequency $\omega_{fi} = (\mathcal{E}_f - \mathcal{E}_i)/\hbar$ between initial and final orbital. With this the matrix elements of the laser perturbation (2.32) are reformulated

$$\langle \psi_f | \hat{H}_L(t) | \psi_i \rangle = -e \frac{\omega_{fi}}{\omega} \langle \psi_f | \mathbf{E} \cdot \hat{\mathbf{r}} | \psi_i \rangle \cos(\omega t + \phi) = -\frac{\omega_{fi}}{\omega} \langle \psi_f | \hat{V}(t) | \psi_i \rangle . \quad (2.35)$$

2.2.3. Minimal coupling by unitary transformation

The transition from an unperturbed Hamiltonian to the expression (2.22) involving the vector potential can also be realized by a unitary transformation. The corresponding procedure is presented and carried out in [49] and will be introduced in the following. In contrast to the previous approach this second approach can be applied to a more general Hamiltonian. Although this property is not needed for our model, the following transformation will also be accurate for a non-local or momentum dependent potential. We will thus obtain a more general expression of coupling between electrons and electromagnetic radiation.

The time-dependent Hamiltonian is generated by performing a unitary transformation

$$\hat{H}(\hat{\mathbf{r}}, \hat{\mathbf{p}} - e\mathbf{A}(t)) = \hat{U}(\hat{\mathbf{r}}, t)\hat{H}_0(\hat{\mathbf{r}}, \hat{\mathbf{p}})\hat{U}^\dagger(\hat{\mathbf{r}}, t) . \quad (2.36)$$

To determine an appropriate unitary matrix $\hat{U}(\hat{\mathbf{r}}, t)$, we use the relation

$$g\left(\hat{\mathbf{r}}, \hat{\mathbf{p}} - \hbar \frac{\partial f(\hat{\mathbf{r}})}{\partial \hat{\mathbf{r}}}\right) = e^{if(\hat{\mathbf{r}})}g(\hat{\mathbf{r}}, \hat{\mathbf{p}})e^{-if(\hat{\mathbf{r}})} \quad (2.37)$$

which can be proven by means of the commutation relation between the conjugate variables $\hat{\mathbf{r}}$ and $\hat{\mathbf{p}}$. To adapt this relation to the left-hand side of equation (2.36), we choose

$$f(\hat{\mathbf{r}}) = \frac{e}{\hbar}\chi(\hat{\mathbf{r}}, t) , \quad (2.38)$$

where $\chi(\hat{\mathbf{r}}, t)$ is a scalar function that fulfills $\nabla\chi(\hat{\mathbf{r}}, t) = \mathbf{A}(t)$. This can be realized for example by

$$\chi(\hat{\mathbf{r}}, t) = \mathbf{A}(t) \cdot \hat{\mathbf{r}} . \quad (2.39)$$

By establishing this definition we assumed the vector potential to be spatially constant, which is synonymous to the electric dipole approximation. The interaction of the electrons with the magnetic field of the laser light was already neglected before. By combining definitions (2.37), (2.38) and (2.39), we identify the unitary matrix

$$\hat{U}(\hat{\mathbf{r}}, t) = e^{\frac{ie}{\hbar}\chi(\hat{\mathbf{r}}, t)} \quad (2.40)$$

to perform the transformation (2.36). The unitary transformation can be explicitly calculated by using the operator property [50]

$$e^{\lambda B}\hat{A}e^{-\lambda B} = \hat{A} + \lambda[\hat{B}, \hat{A}] + \frac{\lambda^2}{2!}[\hat{B}, [\hat{B}, \hat{A}]] + \dots , \quad (2.41)$$

with the scalar factor λ and the operators \hat{A} and \hat{B} as \hat{H}_0 and χ as defined in (2.39). Obviously this expression also includes all terms of higher order with respect to the perturbative field $\mathbf{A}(t)$. If only terms linear in $\mathbf{A}(t)$ are considered, the time-dependent Hamiltonian is given by

$$\hat{H}(t) = \hat{H}_0 + \frac{ie}{\hbar}[\chi(\hat{\mathbf{r}}, t), \hat{H}_0] = \hat{H}_0 + \frac{ie}{\hbar}[\hat{\mathbf{r}} \cdot \mathbf{A}(t), \hat{H}_0] . \quad (2.42)$$

As performed in the previous section, the amplitude of the vector potential can be expressed by the electric field amplitude to calculate the matrix elements

$$\hat{H}(t)_{mn} = (\hat{H}_0)_{mn} + \cos(\omega t + \phi) \frac{eE_0}{\omega \hbar} \sum_l ((\hat{\mathbf{r}} \cdot \boldsymbol{\epsilon})_{ml} (\hat{H}_0)_{ln} - (\hat{H}_0)_{ml} (\hat{\mathbf{r}} \cdot \boldsymbol{\epsilon})_{ln}) . \quad (2.43)$$

Using the transition matrix elements \hat{V}_{ab} between states a and b as defined in (2.35), we get

$$\hat{H}(t)_{mn} = (\hat{H}_0)_{mn} + \sum_n \left((\hat{V}(t))_{ml} \frac{(\hat{H}_0)_{ln}}{\hbar\omega} - \frac{(\hat{H}_0)_{ml}}{\hbar\omega} (\hat{V}(t))_{ln} \right) . \quad (2.44)$$

Similar to (2.31) the time-dependent Hamiltonian is a sum of the equilibrium Hamiltonian and a term representing the optical excitation. However, in contrast to (2.31) the time-dependent excitation matrix $\hat{V}(t)$ is not just added to \hat{H}_0 but the equilibrium Hamiltonian itself enters the excitation term in form of a commutator with $\hat{V}(t)$.

2.2.4. The transition matrix elements

The results of both approaches, 2.2.2 and 2.2.3, involve as essential ingredient (2.35), the time-dependent perturbation $\hat{V}(t) = e\mathbf{E}(t) \cdot \hat{\mathbf{r}}$. Its matrix elements embody the geometric configuration of the electric field's polarization vector and the position operator. Given a specific polarization of laser light they characterize the possibility of a transition between initial and final orbital. The strength of interaction induced by the laser pulse depends on its polarization and its orientation towards the orbitals within the sample. But it also depends on the azimuthal and magnetic quantum numbers of the interacting orbitals.

The laser pulse impinges upon the sample at the polar angle θ_{ph} with respect to the z -axis and the azimuthal angle ϕ_{ph} with respect to the x -axis. The corresponding electric field is divided into its components parallel and perpendicular to the plane of incidence. This plane is defined by the direction of incidence and the surface normal, which is assumed parallel to the z -axis in the following

$$\mathbf{E}(t) = \mathbf{E}_{\parallel}(t) + \mathbf{E}_{\perp}(t) = E_{\parallel}(t) \begin{pmatrix} -\cos \phi_{ph} \cos \theta_{ph} \\ -\sin \phi_{ph} \cos \theta_{ph} \\ \sin \theta_{ph} \end{pmatrix} + E_{\perp}(t) \begin{pmatrix} -\sin \phi_{ph} \\ -\cos \phi_{ph} \\ 0 \end{pmatrix} . \quad (2.45)$$

To model elliptically and circularly polarized light it is necessary to introduce a phase shift between the two orthogonal contributions of the electrical field. For the sake of flexibility in our code each component E_{\parallel} and E_{\perp} is modeled with its individual phase shift ϕ_{\parallel} and ϕ_{\perp}

$$E_{\diamond}(t) = E_{\diamond} \cos(\omega t + \phi_{\diamond}), \quad \diamond = \parallel, \perp . \quad (2.46)$$

We will omit the time dependence during the following derivation for clarity of notation. In the end it will be retrieved as a scalar factor for each component of the

electric field individually. However, for now the time dependence is irrelevant to predict the existence of specific optical transitions.

Based on the geometric decomposition of the electric field, also the transition matrix (2.35) is split into different contributions

$$\hat{V}_{fi}^{\parallel} = e \langle \psi_f | \mathbf{E} \cdot \hat{\mathbf{r}} | \psi_i \rangle_z + e \langle \psi_f | \mathbf{E} \cdot \hat{\mathbf{r}} | \psi_i \rangle_{\parallel} \quad \text{and} \quad \hat{V}_{fi}^{\perp} = e \langle \psi_f | \mathbf{E} \cdot \hat{\mathbf{r}} | \psi_i \rangle_{\perp} . \quad (2.47)$$

The position vector $\hat{\mathbf{r}}$ is expressed in spherical coordinates with the radial distance r and the solid angle $\Omega = (\theta, \phi)$. With this the contributions (2.47) to the electric dipole operator can also be expressed in terms of spherical harmonics [51]

$$\begin{aligned} \langle \psi_f | \mathbf{E} \cdot \hat{\mathbf{r}} | \psi_i \rangle_{\perp} &= \frac{iE_{\perp}}{\sqrt{2}} \sqrt{\frac{4\pi}{3}} \langle \psi_f | \hat{r} (e^{i\phi_{ph}} Y_1^{-1}(\Omega) + e^{-i\phi_{ph}} Y_1^1(\Omega)) | \psi_i \rangle \\ \langle \psi_f | \mathbf{E} \cdot \hat{\mathbf{r}} | \psi_i \rangle_{\parallel} &= \cos \theta_{ph} \frac{E_{\parallel}}{\sqrt{2}} \sqrt{\frac{4\pi}{3}} \langle \psi_f | \hat{r} (e^{i\phi_{ph}} Y_1^{-1}(\Omega) - e^{-i\phi_{ph}} Y_1^1(\Omega)) | \psi_i \rangle \\ \langle \psi_f | \mathbf{E} \cdot \hat{\mathbf{r}} | \psi_i \rangle_z &= -\sin \theta_{ph} E_{\parallel} \sqrt{\frac{4\pi}{3}} \langle \psi_f | \hat{r} Y_1^0(\Omega) | \psi_i \rangle . \end{aligned} \quad (2.48)$$

In the same way the initial and final orbital are described as a product of radial function and spherical harmonics

$$\psi_i(\mathbf{r}) = \varphi_i(r) Y_l^m(\Omega) \quad \text{and} \quad \psi_f(\mathbf{r}) = \varphi_f(r) Y_n^o(\Omega) . \quad (2.49)$$

The integration embodied within the matrix elements is divided into a radial integration and an integration over the solid angle Ω . The former one leads to the radial matrix element

$$R_{fi} = \sqrt{\frac{4\pi}{3}} \int \varphi_f^*(r) r^3 \varphi_i(r) dr . \quad (2.50)$$

It measures the overlap and with it also the probability of a transition between the interacting orbitals. The spherical integration on the other hand yields the Gaunt coefficients [52], [53]

$$C_{nil}^{ojm} = \int Y_n^{o*}(\Omega) Y_i^j(\Omega) Y_l^m(\Omega) d\Omega . \quad (2.51)$$

The indices n and o refer to the azimuthal and magnetic quantum number of the final orbital, while l and m refer to the corresponding quantum numbers of the initial orbital, as introduced in (2.49). The orientation of the position vector is described by the indices $i = 1$ and $j = 0, -1, 1$. Now the components of (2.47) can be expressed as

$$\langle \psi_f | \mathbf{E} \cdot \hat{\mathbf{r}} | \psi_i \rangle_z = -E_{\parallel} \sin \theta_{ph} R_{fi} C_{n1l}^{o0m} , \quad (2.52)$$

$$\langle \psi_f | \mathbf{E} \cdot \hat{\mathbf{r}} | \psi_i \rangle_{\parallel} = \frac{1}{\sqrt{2}} E_{\parallel} \cos \theta_{ph} R_{fi} [-e^{i\phi_{ph}} C_{n1l}^{o1m} + e^{-i\phi_{ph}} C_{n1l}^{o-1m}] \quad \text{and} \quad (2.53)$$

$$\langle \psi_f | \mathbf{E} \cdot \hat{\mathbf{r}} | \psi_i \rangle_{\perp} = -\frac{i}{\sqrt{2}} E_{\perp} R_{fi} [e^{i\phi_{ph}} C_{n1l}^{o1m} + e^{-i\phi_{ph}} C_{n1l}^{o-1m}] . \quad (2.54)$$

The resulting perturbation matrices \hat{V}^{\parallel} and \hat{V}^{\perp} are Hermitian. This property extends to the time-dependent Hamiltonian $\hat{H}(t)$ and guarantees a unitary time evolution.

The symmetry of the integrands represented by the matrix elements (2.47) implies several selection rules [43]. If an integrand exhibits odd symmetry with respect to the position vector the integration yields zero and the corresponding transition does not occur. In the scope of the respective approximation it is then called a forbidden transition.

The presented electric dipole approximation yields the following selection rules: $n = l \pm 1$ and $o = m, m \pm 1$. The azimuthal quantum number has to change with $\Delta l = l_f - l_i = \pm 1$. Possible transitions within our model are therefore just between orbitals $s \leftrightarrow p$ and between orbitals $p \leftrightarrow d$. The magnetic quantum number however does not have to change. Within our simulation we did not consider the influence of the magnetic field associated with the laser light. Therefore the spin quantum number does not change $\Delta s = s_f - s_i = 0$ and transitions only happen between orbitals with the same spin. In view of the desired application of our model it is important to keep in mind that the simulated change of magnetization will never happen as a direct result of the optical excitation, because the laser light itself leaves the electronic spin unchanged. It can however induce a spin polarization in connection with spin-orbit coupling introduced spin-mixing.

If terms of higher order in the perturbation \mathbf{A} are taken into account, also so-called forbidden transitions can occur. For instance the sets of quadrupole and octupole selection rules can be found in common literature. Yet transitions generated by the coupling of the laser field to a higher order multipole take place with a much lower transition rate and would barely change the results.

2.2.5. A finite pulse

To meet the conditions of a real experiment a laser pulse has to be simulated. On that account we have to include its finite temporal duration into the model. In *EVOLVE* the laser beam can be described using a Gaussian or a Lorentzian envelope function,

$$\lambda(t) = \exp\left(\frac{-2(t-t_0)^2}{\tau^2}\right) \quad \text{or} \quad \lambda(t) = \frac{(\tau/2)^2}{(t-t_0)^2 + (\tau/2)^2} . \quad (2.55)$$

The envelope function determines the peak time t_0 and duration of the laser pulse. It reaches its maximum E_0 at t_0 and has a width of τ at half maximum. This envelope function was not taken into account in the course of the above derivations. Nevertheless these derivations still hold if the pulse width is not too short compared to the laser frequency (cf. Sec. A.1 in the appendix). The perturbation matrix as defined in equation (2.35) is now replaced by

$$\hat{V}(t) = \left[(\hat{V}^{\parallel} \cdot \cos(\omega(t-t_0) + \phi_{\parallel})) + (\hat{V}^{\perp} \cdot \cos(\omega(t-t_0) + \phi_{\perp})) \right] \cdot \lambda(t) . \quad (2.56)$$

\hat{V}^{\diamond} are the time-independent components of the interaction matrix as defined in (2.47). Parallel and transversal components are each multiplied by a time dependence with individual phase shifts according to the polarization of the laser light (2.46).

A continuous wave laser is assumed to emit an electromagnetic wave of infinite temporal duration. It exhibits just a single frequency defined by the photon energy

$$E_{ph} = h\nu . \quad (2.57)$$

In order to achieve an excitation the transition frequency ω_{fi} , determined by the level spacing, has to coincide with the laser frequency ω . In case of our model with discrete energy eigenvalues a sharply defined excitation frequency would almost surely not match with an energy spacing and therefore not yield any excitation. However, in case of a laser pulse with a finite temporal duration $\nu = \omega/2\pi$ is the carrier frequency of a broader frequency spectrum. Long pulses exhibit a very sharp peak at the well defined carrier frequency ν . In case of ultrashort laser pulses the pulse duration can be equivalent to only just about 4 optical cycles. This leads to a relatively broad range of frequencies around the primary frequency. Spectral width $\Delta\nu$ and temporal width τ are connected by the Fourier transform. The spectral width is not just determined by the pulse length but also by the shape of the laser pulse. In case of a Gaussian pulse the product of temporal and spectral width is limited by [54]

$$\Delta\nu \cdot \tau \geq 0.44 . \quad (2.58)$$

For example a pulse with a duration of only $\tau = 10$ fs exhibits a spectral width of more than $\Delta\nu = 44$ THz, whereas a pulse width of 100 fs yields a spectral width of only $\Delta\nu = 4.4$ THz. This are 10 % in contrast to 1 % compared to a carrier frequency of $\nu = 400$ THz.

2.2.6. A comment on basis sets

By defining a time-dependent Hamiltonian we also introduced a set of time-dependent eigenenergies. However, we are not primarily interested in these eigenenergies' time evolution but foremost in the time evolution of the corresponding eigenstates' occupation numbers. The occupation is expressed in terms of a density matrix as explained in Section 2.3. To calculate its time evolution and relevant observables the density matrix has to be expressed in terms of a basis set. For this purpose in principle any basis set can be used. In the following lines the choice of the equilibrium eigenbasis shall be discussed.

As described in the preceding sections in equations (2.31) and (2.44) the laser excitation is added to the ground state Hamiltonian in form of a perturbative term resulting in a time-dependent Hamiltonian $\hat{H}(t)$. Nevertheless the ground state Hamiltonian \hat{H}_0 as introduced in Section 2.1 defines the equilibrium basis set, that will be used to perform the time propagation as presented in Chapter 3. The excitation terms in (2.31) and (2.44) containing $\hat{V}(t)$ will merely be treated as a perturbation that is added to the ground state Hamiltonian. Alternatively for every time step the newly defined and fast oscillating eigenlevels of $\hat{H}(t)$ have to be calculated and therewith also in every time step the change of the basis set becomes necessary.

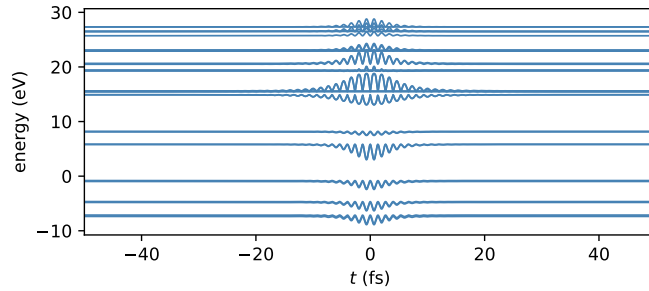


Figure 2.2.: Transient eigenenergies of a 4 four-atomic system with s and p levels located at each site.

Instead of accounting for the change of level energies it is computationally more efficient to represent the changing occupation matrix in terms of the fixed equilibrium eigenstates.

This approach is appropriate as long as the transient basis set can be adequately represented by the fixed basis set. The unperturbed eigenlevels have to cover an energy range sufficiently broad to describe also the transient states excited by the laser pulse. The approach fails if the perturbation is so strong, that extremely high energies become populated, which are badly represented by the ground state eigenbasis. This is however a general issue if a finite basis is applied to describe a system. Furthermore, the chosen approach overlooks effects that go beyond simple shifts of the energy levels. On top of those shifts the optical excitation can also change essential features of the band structure, like band crossings and band gaps. The closing of a band gap for example is crucial for an insulator-metal transition. Since no insulators but metals shall be simulated, luckily this effect is of minor importance in case of the presented model system.

To justify the chosen approach the modification of the electronic structure by the electric field of the laser pulse shall be estimated. Dependent on the strength of the laser field the time-dependent eigenenergies can differ distinctly from the unperturbed band structure. The optical excitation manifests in form of shifted and oscillating eigenenergies synchronous with the applied laser pulse. This effect is illustrated in Figure 2.2 on a system similar to those investigated in Section 4.2.1. Also all excitation parameters, like pulse length and strength, were adopted from this section. However, for reasons of clarity and comprehensibility d orbitals were omitted and just four sites with s and p orbitals were taken into account. Since the d levels are located in a narrow central energy window the overall energy range does not change. In this way the extent of excitation and perturbation on the eigenlevels can still be estimated also for larger systems. The perturbations of the eigenenergies due to the optical excitation are clearly visible. But the modified eigenenergies do not significantly exceed the range of ground state eigenenergies. Therefore the equilibrium basis set proves applicable to also express excited energy states.

From an experimental point of view the transient band structure is represented by a series of time-resolved photoemission spectra which exhibit intensity changes. These changes can be attributed to either the changes of electronic structure or to shifts of the spectral weight - which means to the change in occupation probabilities of the energy levels. Both approaches are not mutually exclusive but complementary. By using a density operator approach we describe the effects of excitation by changing occupation within the fixed ground state eigenlevels which yields an easier interpretation.

While the time propagation of the system is performed in terms of the equilibrium eigenstates we switch back to the basis of local atomic orbitals to express and calculate the system observables. This basis set is favourable to account for local differences which will be of paramount importance in magnetic/nonmagnetic interface systems as investigated in Section 4.2. All relevant system properties such as changes of occupation and magnetization are therefore calculated in terms of the local atomic basis.

As explained above we are interested in the occupation numbers to perform the time evolution. Therefore in the next section the concept of a density matrix will be introduced.

2.3. Effective single-particle density matrix

Throughout the following section the properties of the density operator will be discussed. The density matrix is its representation in a certain basis set. Although strictly speaking the former one describes a quantum mechanical operator and the latter one its specific matrix representation, mostly the designation density matrix will be used synonymously for both objects. Again this topic is covered in many textbooks like [55], [56], but an extensive pedagogical introduction to density matrices especially if in contact with an external bath can be found in the book by Schlosshauer [57].

Up to this point the Hamiltonian of the system was introduced. Each eigenstate of the Hamiltonian represents a specific wavefunction which encodes information like corresponding eigenenergy, spin polarization and localization. Usually such a wavefunction is used to calculate all information that is available about a quantum system. By using a density matrix though the handling of the wavefunction can be avoided. The density matrix is a more general concept to represent information about the system. It comprises all the information that is contained in the wavefunctions of the system but in addition also provides probabilistic information about all possible outcomes of measuring an ensemble of identically prepared systems.

A density matrix is advantageous compared to a wavefunction because it can express a lack of knowledge about the system. If the system can be represented by a single wave function it is in a so-called *pure state*. Sometimes however we cannot find a single wave function to represent the quantum state of the system because there is no complete knowledge about it. In such situations the system is in a *mixed state* and has to be represented by a density matrix. Mixed quantum states can arise

firstly due to lack of information about the preparation of the system. Actually the system is in a pure quantum state, but to the observer it is not known in which. All possible outcomes of a measurement are then described by a statistical ensemble. The density matrix contains the information about this set of pure states and their corresponding probabilities. Secondly, mixed quantum states can describe a situation of entanglement with an external system. A density matrix that only characterizes a subsystem of a composite system is called a reduced density matrix and is associated with a loss of knowledge. This is because information about the interaction with the external system is missing within the reduced density matrix and therefore it describes a mixed quantum state. Such a situation is called an *improper mixture* because the total system could indeed be in a pure quantum state.

The scenario of a reduced density matrix is of importance to describe dynamics with relaxation due to coupling to an external reservoir. Exactly this is the scenario that shall be implemented in our model. Therefore open quantum systems and their time evolution will be further expanded upon in Section 2.3.1 and the following Chapter 3.

These two distinct approaches also historically motivated the introduction of the concept of a density matrix. On the one hand, as evident by the name, the density matrix is considered in analogy to a probability density function to describe statistical ensembles as proposed by Wigner [58] in 1932. But already in 1927 von Neumann introduced the concept of a density matrix in order to describe the statistical aspects of quantum mechanics [59]. On the other hand Landau introduced a density matrix to describe mixed quantum states in a subsystem of a larger system [60].

To summarize, wavefunctions can just express pure quantum states whereas density matrices can express mixed quantum states like in a statistical ensemble. Instead of assigning a single particular state to the system, a density matrix describes a system that can be found in different pure states with corresponding different probabilities. Within the present work the density matrix is needed to describe mixed quantum states due to the coupling to an external bath and to perform the corresponding time evolution by means of a master equation.

To finally give a formal definition, let \mathcal{H} be a Hilbert space. A density operator describes the probability to measure the system in different states $|\Psi_i\rangle \in \mathcal{H}$ in terms of the tensor product

$$\hat{\rho} = \sum_{ij} |\Psi_i\rangle \rho_{ij} \langle \Psi_j| . \quad (2.59)$$

Just like the wave function, the density matrix can be used to calculate the expectation value of a system's observable

$$\langle \hat{A} \rangle_{\hat{\rho}} = \text{tr}(\hat{\rho} \hat{A}) = \sum_{ki} \rho_{ki} A_{ik} , \quad (2.60)$$

with $A_{ik} = \langle \Psi_i | \hat{A} | \Psi_k \rangle$ being the observable's matrix elements. To describe an actual physical system a density operator $\hat{\rho}$ has to comply with several requirements. $\rho(\mathcal{H})$, the space of such density operators on the Hilbert space \mathcal{H} , is a convex set of linear operators on \mathcal{H} and all its elements are

- positive,
- of trace 1
- and as a consequence also Hermitian.

The first requirement ensures, that for no state $|\Psi\rangle \in \mathcal{H}$ the expectation value of $\hat{\rho}$ can be negative:

$$\hat{\rho} \geq 0 \quad \text{if} \quad \langle \Psi | \hat{\rho} | \Psi \rangle \geq 0 \quad \text{for all} \quad |\Psi\rangle \in \mathcal{H} . \quad (2.61)$$

This is equivalent to constrain the probability to measure a specific state to never be less than zero. This condition ensures the physicality of the corresponding occupation number and of the associated measurement's outcome. The second requirement concerns the trace of the density matrix. With its diagonal elements regarded as a probability to measure the corresponding state, this second requirement sets the total probability to measure any state to one, fulfilling a basic principle of probability theory and quantum physics. Finally the Hermiticity, as general property of any physical observable, is simply a consequence of points one and two.

Another consequence of these attributes is the condition

$$\mathcal{P}(\hat{\rho}) = \text{tr} \hat{\rho}^2 \leq 1 . \quad (2.62)$$

This quantity is called the purity of the density matrix ρ and measures the very same on a scale between $\frac{1}{d}$ and 1. The lower boundary is determined by the dimension d of the Hilbert space. It corresponds to a density matrix of minimal purity and a maximal degree of mixedness and is achieved if every state is equally probable. In case of a pure quantum state it is $\hat{\rho}^2 = \hat{\rho}$ and expression (2.62) holds with equality. Moreover, the density matrix of a pure quantum state has rank one – the system is characterized by one single wave function. Whereas the density matrix of a mixed quantum state has to be described by at least two wave functions and has a rank greater than one. At least two of its eigenvalues are nonzero. Independent of the basis set the trace in equation (2.62) is strictly smaller than one in case of a mixed quantum state.

Let's for the moment restrict to a so-called single-electron density matrix to discuss the meaning of its matrix elements $\rho_{ij} = \langle \Psi_i | \hat{\rho} | \Psi_j \rangle$. A diagonal element ρ_{ii} of this density matrix represents the occupation of the corresponding state $|\Psi_i\rangle$. Therefore, a diagonal element of this density matrix describes the probability to find the electron in a specific state. In contrary, the offdiagonal elements are not directly related to physical observables. They are called coherence or interference terms and are far more elusive. The element ρ_{ij} , $i \neq j$ for example describes a coherent superposition of states $|\Psi_i\rangle$ and $|\Psi_j\rangle$. As $\hat{\rho}$ is Hermitian, there is always a basis set in which it takes the diagonal form. The existence of coherences therefore also depends on the representing basis set, what makes them even more difficult to comprehend. For example

$$(\hat{\rho})_{\hat{\sigma}_z} = \begin{pmatrix} 1 & 0 \\ 0 & 0 \end{pmatrix} \quad \text{and} \quad (\hat{\rho})_{\hat{\sigma}_x} = \frac{1}{2} \begin{pmatrix} 1 & 1 \\ 1 & 1 \end{pmatrix} \quad (2.63)$$

are both density matrices representing a spin-up state with respect to the z -axis, first in terms of eigenstates of $\hat{\sigma}_z$ and second in terms of eigenstates of $\hat{\sigma}_x$. Within the second density matrix $(\hat{\rho})_{\hat{\sigma}_x}$, the offdiagonal elements describe a coherent superposition of spin-up and spin-down states with respect to the x -axis. This is necessary to represent a spin-up state with respect to the z -axis within this basis set. At this point it is important to distinguish between mixed and superimposed states. Likewise the existence of coherences does not permit conclusions about the degree of mixedness. Despite the presence of offdiagonal elements in $(\hat{\rho})_{\hat{\sigma}_x}$ both density matrices embody the same pure quantum state.

In Section 2.1 it was demonstrated how to calculate the electronic structure of a realistic material by means of a tight-binding model. Now we seek to simulate the occupation within this structure using a suitable realistic number of valence electrons. The goal is therefore to simulate not just one but N_e electrons, according to the chosen material. A system of N_e electrons is described by the many-body wave function $\Psi(x_1, x_2, \dots, x_{N_e})$. The coordinate x_i represents the i th electron. In the context of many-body theory it is often used to comprise for example spatial and spin coordinates. Already with a discrete basis of M atomic orbitals instead of the continuous coordinates x_i the many-body wave function as well as the corresponding many-body density matrix are enormously large objects of dimensions MN_e and $(MN_e)^2$, respectively. Accordingly the solution of the corresponding master equation is a big computational problem which scales exponentially with the number of electrons.

If the Hamiltonian just contains single-particle or two-particle operators it is possible to reduce the problem tremendously since all electrons in the system are identical. If for the moment the exchange interaction is neglected, then the many-body Hamiltonian can be decomposed into N_e times the same single-particle Hamiltonian $\hat{H}^{(1)}$, each describing one separate non-interacting electron. The energy of the system can now be calculated as the sum of N_e identical one-particle energies

$$E = \langle \hat{H}^{MB} \rangle_{\hat{\rho}^{MB}} = N_e \langle \hat{H}^{(1)} \rangle_{\hat{\rho}^{(1)}} . \quad (2.64)$$

The corresponding expectation value is calculated by means of the one-particle density matrix $\hat{\rho}^{(1)}$. This mean-field-like approximation is comparable to the approach suggested by Pershin et al. [61]. However, they map the many-body problem to N_e different single-electron problems each with its own density matrix and Lindblad operator.

Similarly the one-particle density matrix can be extracted from the many-body density matrix since all electrons are identical. According to the Pauli principle the many-body wave function only changes sign if the positions of two electrons are swapped. Therefore in case of non-interacting electrons it is possible to reduce the problem by integrating over the redundant degrees of freedom

$$\begin{aligned} \hat{\rho}^{(1)}(x, x') &= \int \Psi^*(x', x_2, \dots, x_{N_e}) \Psi(x, x_2, \dots, x_{N_e}) dx_2 \dots dx_{N_e} \\ &= \int \hat{\rho}^{MB}(x', x_2, \dots, x_{N_e}; x, x_2, \dots, x_{N_e}) dx_2 \dots dx_{N_e} . \end{aligned} \quad (2.65)$$

In case of the discrete basis set of atomic tight-binding orbitals introduced before the integration of the many-body density matrix (2.65) takes the form of a summation

$$\left(\hat{\rho}^{(1)}\right)_{mn} = \sum_k \rho_{mk,nk}^{MB}. \quad (2.66)$$

Indices m and n refer to the first electron, while the multi-index k comprises the degrees of freedom of all other electrons. Equations (2.65) and (2.66) are equivalent to perform a partial trace over all electron coordinates but one. Together with the Hamiltonian $\hat{H}^{(1)}$, which is equivalent to the tight-binding Hamiltonian (2.16), the many-body problem can now be reduced to N_e times a single-electron problem. These N_e single-electron density matrices behave completely identical and thus can be summed up to

$$\hat{\mathbf{P}} = N_e \hat{\rho}^{(1)}. \quad (2.67)$$

We will call this object the occupation matrix and treat it as a density matrix that is normalized to $\text{tr} \hat{\mathbf{P}} = N_e$. By doing so the diagonal elements can be interpreted as the mean occupation numbers of the respective states. The trace of $\hat{\mathbf{P}}$ gives the total number of particles in the system and has to be conserved throughout the entire time evolution. To recover the features of a probability density function the occupation matrix has of course to be rescaled by a factor of $1/N_e$. By substituting $\hat{\rho}^{(1)}$ by $\hat{\mathbf{P}}$ not just one but N_e electrons are simulated. But this simplification leads to some problems. By replacing the many-body problem with a single-particle problem we tremendously reduce the computational cost, but we also omit electron-electron interaction and with that we omit correlations between electrons. An electron will not be repelled by another electron, because technically the occupation matrix $\hat{\mathbf{P}}$ still represents just one electron that is scaled up by a factor. As a consequence occupation numbers $\mathbf{p}_{ii} > 1$ bigger than one can arise. This is however forbidden by the Pauli exclusion principle. To ensure physicality of the occupation numbers it is therefore necessary to explicitly implement the Pauli principle. As the diagonal elements of $\hat{\mathbf{P}}$ are representing the orbital occupation numbers the condition

$$0 \leq \mathbf{p}_{ii} \leq 1 \quad \text{for all } i \in \{1, \dots, M\} \quad (2.68)$$

has to be fulfilled. If so, the corresponding single-particle density matrix $\hat{\rho}^{(1)}$ is called ensemble N_e -representable. That means, there exists at least one N_e -particle density matrix that, after contraction, yields the density matrix $\hat{\rho}^{(1)}$. The ensemble N_e -representability conditions were first discussed by Coleman [62]. For a single-particle density matrix they coincide with the Pauli principle (2.68). A special difficulty arises in connection with the time evolution of $\hat{\rho}^{(1)}$ in an open system. The preservation of the ensemble N_e -representability conditions during the evolution is a nontrivial problem and often discussed, especially in connection with a Lindblad-like evolution [63], [64]. We address this problem heuristically by inserting Pauli blocking factors into the bath induced transition rates. This approach will be specified by the time the coupling to an external bath is introduced in Section 3.4.

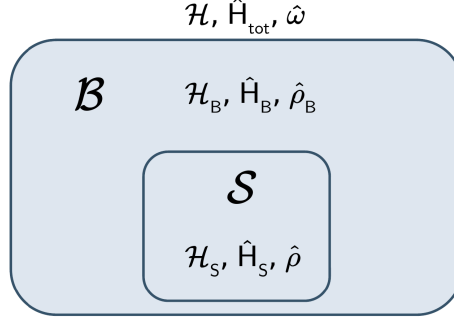


Figure 2.3.: Sketch of system and environment with its respective Hilbert space, Hamiltonian and density matrix.

While the restriction of the occupation numbers is the main and most obvious problem because it disrespects the physicality of the system, electron-electron interaction is also important for magnetism effects. For example the exchange coupling is determined by correlation effects between electrons and can be modified in the process of demagnetization. This issue is however of minor importance in this context, because we use a fixed electronic structure with orbitals that were constructed by fitting to *ab initio* calculations which include correlations in terms of the exchange-correlation functional.

By these presented procedures the many-body problem is now mapped to a set of effective single-particle systems, which are condensed in the occupation matrix. This approach may be understood as a mean-field approximation.

2.3.1. Open quantum systems

In consequence of the laser perturbation high-energy states of the system are populated. Under realistic conditions the energy thus accumulated in the system is lost by interaction with the environment. To account for this loss of energy, we have to introduce coupling to an external system, the environment. Such a scenario is described by a composite system as depicted in Figure 2.3. A small part of the total system represents the actual system of interest - the finite electronic system \mathcal{S} . It is coupled to the environment \mathcal{B} . Adopting the denomination of Breuer and Petruccione [65] we will call this environment a heat bath, if it has infinitely many degrees of freedom and is in a thermal equilibrium state. In the following we will assume this special environment, as it will be very useful to derive the system dynamics. The corresponding Hilbert spaces of system and bath are \mathcal{H}_S and \mathcal{H}_B . The total Hilbert space is the outer product of both $\mathcal{H} = \mathcal{H}_S \otimes \mathcal{H}_B$. Let $\mathcal{B}(\mathcal{H})$ be the space of bounded operators on a Hilbert space \mathcal{H} . Accordingly there are Hamiltonians $\hat{H}_S \in \mathcal{B}(\mathcal{H}_S)$ acting just on the system, $\hat{H}_B \in \mathcal{B}(\mathcal{H}_B)$ acting just on the bath and the Hamiltonian

of the total system

$$\hat{H}_{\text{tot}} = \hat{H}_{\mathcal{S}} \otimes \hat{\mathbb{1}}_{\mathcal{B}} + \hat{\mathbb{1}}_{\mathcal{S}} \otimes \hat{H}_{\mathcal{B}} + \alpha \hat{H}_I, \quad \hat{H}_{\text{tot}} \in \mathcal{B}(\mathcal{H}) . \quad (2.69)$$

The interaction between system and bath is described by the Hamiltonian $\hat{H}_I \in \mathcal{B}(\mathcal{H})$ and the parameter α is a measure of the coupling strength. The system \mathcal{S} is called an open quantum system, if interactions with the environment are allowed. The parameter α will be of importance later on to estimate the validity of the applied approximations. The density matrix of the total system $\hat{\omega} \in \rho(\mathcal{H})$ is a large and complex object that can not be accessed numerically. It is therefore impossible to simulate the full dynamics of the total system. However, within this work we are only interested in the dynamics of the finite system \mathcal{S} , whereas the detailed dynamics and composition of the heat bath are unimportant. Therefore the simulation is restricted to the dynamics of \mathcal{S} , which are embodied in $\hat{\rho} \in \rho(\mathcal{H}_{\mathcal{S}})$. This is the *reduced density matrix* of the system and can be obtained from the total density matrix $\hat{\omega}$ by tracing out the environmental degrees of freedom,

$$\hat{\rho} = \text{tr}_{\mathcal{B}} \hat{\omega} = \sum_i \langle \phi_i | \hat{\omega} | \phi_i \rangle . \quad (2.70)$$

These degrees of freedom are represented by the set $\{|\phi_i\rangle\}$, which is an orthonormal basis of $\mathcal{H}_{\mathcal{B}}$. By restricting the simulation to the reduced density matrix also the computational problem is reduced tremendously and only $\hat{\rho}$ has to be propagated in time.

To analyze the implications of the reduction (2.70) let's revisit the discussion of pure and mixed states launched in Section 2.3. If there is no interaction between the system and the bath, then system and bath states can be separated into a product form. It exists a wavefunction to describe the system and if we knew it we could in principle represent the system by a pure state. For $\alpha \neq 0$ system and bath are entangled and their wavefunctions can no longer be separated. It exists no single well-defined wavefunction to describe the system \mathcal{S} separately because the bath induces correlations between the system states. The system is in a mixed state now and has to be described by a density matrix. That means omitting the bath degrees of freedom involves also a loss of information. It is not possible to ascribe the system with certainty to a particular state but instead the system is with different probabilities in different states. It hence is represented by a probabilistic mixture of states and all possible outcomes of measurements are described by the reduced density matrix $\hat{\rho}$.

The Hamiltonian (2.69) and the scenario as depicted in Figure 2.3 will be the foundation for calculating the time evolution in Chapter 3. Therefore also the nomenclature introduced in this section will further be valid.

2.3.2. Quantum state measures

The irradiation with a laser pulse perturbs the electronic system by excitation of low energy electrons to higher levels. This can also trigger a subsequent local redistribution of occupation before the system finally evolves back to its initial low-energy

state by interaction with an external heat bath. Throughout all these processes the density matrix $\hat{\rho}(t)$ can change significantly. Moreover, the degree of excitation can differ from one system to another though identical laser parameters are applied, or as characterized in experiments - an identical laser fluence. This difference in excitation is explained by the varying absorption of the laser light, which is caused by a different spacing and occupation of the systems' eigenlevels. The laser fluence is thus not sufficient to quantify and compare the degree of perturbation. Therefore it is necessary to introduce some measures of perturbation which only analyze the density matrix and do not regard observables or the source of perturbation. The first two of the following measures, the purity and the von Neumann entropy, quantify the degree of mixedness or disorder within the density matrix. The remaining measures embody a comparison of two density matrices. Thereby they can measure the agreement or deviation of the perturbed density matrix from an initial unperturbed state.

Throughout the simulation we always operate on the occupation matrix $\hat{P}(t)$ in (2.67). The definition of a quantum state measure will therefore be applied to its rescaled counterpart, the reduced one-electron density matrix $\hat{\rho}(t)$. However, due to the condition of N_e -representability in form of the constraint (2.68), the accessible range of the measures is modified in case of an effective one-particle density matrix in comparison to a many-body density matrix.

All presented measures are invariant under unitary transformations. Therefore they are also independent of the applied basis set. Solely the number of excited electrons is defined only in the unperturbed system's eigenbasis as it is expressed in terms of the system's energy eigenlevels.

Purity

The purity of a density matrix was already introduced in (2.62).

$$\mathcal{P}(\hat{\rho}(t)) = \text{tr } \hat{\rho}(t)^2, \quad \mathcal{P}(\hat{\rho}(t)) \in \left[\frac{1}{d}, \frac{1}{N_e} \right]. \quad (2.71)$$

As pointed out above the accessible range has narrowed, its upper bound of $\frac{1}{N_e}$ is decreasing with the number of simulated electrons. In the general case a maximal purity of 1 is possible and equivalent to a pure state which can be represented by a single wavefunction. It is however never possible in our model to represent N_e electrons with a one-electron wavefunction. The decreased range of the purity represents therefore the lack of knowledge by using a single-particle density matrix, an object too small to represent the information of N_e electrons. If the reduced density matrix in our simulation would reach a purity of 1, some state would have an occupation of $p_{ii} > 1$ in contradiction to the Pauli principle (2.68). At equilibrium and at a finite temperature the density matrix starts the time evolution with a purity near to the maximal value of $1/N_e$ which is decreased by the laser perturbation and slowly recovers afterwards.

Von Neumann entropy

Also the von Neumann entropy measures the degree of mixing. In contrast to the purity it increases under perturbation and reaches its maximal value at a perfectly mixed state. The von Neumann entropy can be easily calculated in terms of eigenvalues $\lambda_i(t)$ of $\hat{\rho}(t)$ [65], [66]

$$S(\hat{\rho}(t)) = -\text{tr}(\hat{\rho}(t) \ln \hat{\rho}(t)) = -\sum_i \lambda_i(t) \ln \lambda_i(t) \quad S(\hat{\rho}(t)) \in [\ln N_e, \ln d] . \quad (2.72)$$

In case of a general density matrix a minimal value of 0 is achieved for a pure state. However, for the same reasons as before the accessible range of the von Neumann entropy is modified due to constraint (2.68). The smallest possible von Neumann entropy in our simulation is therefore $\ln N_e$. The maximal entropy of $\ln d$ is unchanged and corresponds to an equipartition of the electrons between all states.

Fidelity

The fidelity measures the agreement between two quantum states. As the reference matrix we choose the rescaled occupation matrix $\hat{\rho}_0 = \hat{P}_0/N_e$, which corresponds to the equilibrium density matrix before the laser perturbation. It represents the initial equilibrium state at the specified ambient temperature. We measure the agreement between $\hat{\rho}_0$ and the evolving occupation matrix $\hat{\rho}(t)$ of the excited system. The fidelity is defined as [67]

$$F(\hat{\rho}(t), \hat{\rho}_0) = \left(\text{tr} \sqrt{\sqrt{\hat{\rho}_0} \hat{\rho}(t) \sqrt{\hat{\rho}_0}} \right)^2, \quad F(\hat{\rho}(t), \hat{\rho}_0) \in [0, 1] . \quad (2.73)$$

For identical matrices the fidelity equals 1 and for density matrices expressing orthogonal states it is 0.

The fidelity is a quantity that is originated in quantum information theory, where it is used to measure the deviation of a qubit while traveling through an operating device. During the course of the time evolution the fidelity starts with a value of 1, indicating perfect agreement. With the laser excitation its value decreases until finally the equilibrium density matrix is recovered by interaction with the external bath and the fidelity reapproaches 1.

Trace distance

Also the trace distance embodies a comparison between two density matrices [68]. In contrary to the fidelity it increases with growing differences between the two matrices. It yields 0 only for identical matrices and reaches a maximum of 1 for matrices of orthogonal states. Again the equilibrium matrix $\hat{\rho}_0$, defined as above, is chosen as a reference. By exploiting the Hermiticity the trace distance can be easily calculated

in terms of eigenvalues $\xi_i(t)$ of $(\hat{\rho}(t) - \hat{\rho}_0)$

$$T(\hat{\rho}(t), \hat{\rho}_0) = \frac{1}{2} \text{tr} \left[\sqrt{(\hat{\rho}(t) - \hat{\rho}_0)^\dagger (\hat{\rho}(t) - \hat{\rho}_0)} \right] = \sum_i \frac{|\xi_i(t)|}{2}, \quad T(\hat{\rho}(t), \hat{\rho}_0) \in [0, 1]. \quad (2.74)$$

Both quantities, the fidelity as well as the trace distance, are used to measure distances in the space of density matrices. However, among the presented measures only the trace distance is a metric according to the mathematical definition, whereas the fidelity can be used to define a metric, but is not a metric itself.

The number of photo-excited electrons

The number of excited electrons is accessible by experiment [69]. For this reason it is a very useful quantity to adjust pulse parameters within the simulation in order to achieve a realistic degree perturbation.

As indicated by the name, the number of electrons above the Fermi energy per atom is calculated via

$$N_{ex}(\hat{P}(t)) = \frac{1}{N} \sum_{\substack{n \\ \mathcal{E}_n > \mathcal{E}_F}} (\rho_{nn}(t) - \rho_{nn}(t_0)). \quad (2.75)$$

The number of atoms N is used to get a comparable, normalized result. Prior to the laser excitation the eigenlevels are populated according to the Fermi-Dirac statistics. At a reasonable temperature there is a very small amount of electrons above the Fermi energy. These thermally excited electrons are subtracted to get the purely photo-excited electrons. During the laser excitation $N_{ex}(t)$ increases rapidly and then returns to its initial value on a timescale according to the interaction with the bath.

3. Time evolution of a density matrix

3.1. Unitary time evolution and time evolution in open quantum systems

The purpose of this work is the observation and investigation of an electronic system after ultrashort laser excitation. To analyze the induced changes it is necessary to simulate and track the time evolution of the respective system. In the previous chapter it was demonstrated how to describe the system's electronic structure by means of a tight-binding Hamiltonian and how to represent its occupation by using a density or occupation matrix. Now we show how to evolve the density matrix in time. In doing so, we simulate the changes of occupation during optical excitation and subsequent relaxation of a system in contact with a heat bath. On this account, we start with the unitary time evolution of $\hat{\omega}$, the density matrix of the total system introduced in Section 2.3.1. As for every closed system its time evolution is given by the von Neumann equation in the Schrödinger picture

$$i\hbar \frac{\partial \hat{\omega}}{\partial t} = [\hat{H}_{\text{tot}}, \hat{\omega}] \quad , \quad (3.1)$$

which follows from the Schrödinger equation

$$i\hbar \frac{\partial}{\partial t} |\psi(t)\rangle = \hat{H}_{\text{tot}} |\psi(t)\rangle \quad . \quad (3.2)$$

The dynamics entailed by the von Neumann equation (3.1) are called unitary, because the evolution of the corresponding density matrix $\hat{\omega}$ can be expressed by a unitary transformation. The time evolution of the total system is given by

$$\hat{\omega}(t) = \hat{U} \hat{\omega}_0 \hat{U}^\dagger \quad , \quad \text{using} \quad \hat{U} = e^{-\frac{i}{\hbar} \hat{H}_{\text{tot}} t} \quad , \quad (3.3)$$

the operator of time evolution. A unitary evolution is isometric, it does not change the norm of the state vectors. Eigenstates of \hat{H}_{tot} only change by an oscillating phase. Consequently, inner products between quantum states are preserved during unitary time evolution and the coherence of quantum states is maintained. This can be considered as the conservation of information under unitary time evolution. A unitary process is therefore always reversible in time.

Since the Schrödinger equation describes the time evolution of pure states, the unitary evolution in Equation (3.3) only holds for the total system. Whereas a subsystem of a composite system has to meet the premise of complete isolation to exhibit a unitary time evolution. This condition is violated if interaction with the environment is permitted. As a consequence information is lost to the environment, the entropy of the system changes and the subsystem exhibits a non-unitary time evolution. This especially concerns the evolution of a reduced density matrix as introduced in (2.70) and is exactly the scenario of interest. Therefore non-unitary dynamics are necessary to describe the evolution of a subsystem with loss of energy and decoherence due to the coupling to an external system. Because non-unitary time evolution can express decay, decoherence and dissipative behavior, like thermalization, it is in general not time-reversible. Since the time propagation of the reduced density matrix cannot be achieved by the von Neumann equation (3.1), the Lindblad equation will be derived in the following sections.

The Lindblad equation is a Markovian quantum master equation. It describes the time evolution of not just one state but of the entire density matrix. Its structure can be deduced by establishing only two demands: Markovianity and the conservation of the density matrix properties defined in Section 2.3. Therefore it describes the time-evolution of a quantum system in the most general way. The Lindblad equation includes the coherent as well as the incoherent time evolution of the density matrix. It thus contains also non-unitary terms which yield irreversible dissipative processes. They describe the loss of energy and information to the environment. The Lindblad equation is therefore an appropriate method to describe the time evolution in an open system, as for example a fermionic system in contact with a thermal heat bath.

The equation which in this work is called Lindblad equation, actually circulates also under other designations, thereof the longest is Gorini-Kossakowski-Sudarshan-Lindblad equation. These other names are based on fundamental works leading up to the final theory. Already since the late 50s the theory of quantum master equations was developed to describe the general time evolution of a reduced density matrix. The Nakajima-Zwanzig equation based on papers published in 1958 [70] and 1960 [71] is such a quantum master equation. It describes the dynamics of a reduced density matrix by projecting on the relevant subsystem of a total system. However, it still contains the exact dynamics of the system and is similarly hard to solve as the original problem.

Another approach to describe the time evolution of a reduced density matrix is the concept of quantum dynamical semigroups. It was established under that name by Kossakowski in 1972 [72]. A quantum dynamical semigroup comprises the total development of a density matrix and the corresponding generator describes its time evolution. Lindblad [73] and Gorini, Kossakowski and Sudarshan [74] published their works on the generator of such a quantum dynamical semigroup almost simultaneously in 1976. While they find the same results about the shape of the generator, they formulate their mathematical proofs based on different preconditions. Gorini et al. assume a finite-dimensional Hilbert space, whereas Lindblad works with a separable Hilbert space of countable dimension but assumes all operators to be bounded.

Therefore the operators in Section 2.3.1 were defined accordingly. Even so in reality this assumption is not fulfilled, unbounded operators can be approximated by a sequence of bounded operators. The above approach derives the Lindblad equation based on structural requirements for the corresponding propagator. It will therefore be called the geometrical derivation.

The Lindblad equation can also be derived by a series of microscopic assumptions and approximations based on the Hamiltonian dynamics of the total system. This microscopic approach is at times complicated and tedious but it delivers clearer insight into the physical implications of the applied approximations, whereas the geometrical approach stays rather abstract. Although the geometrical approach delivers a clear and straight forward derivation it is harder to access for the physical intuition.

In the following sections the geometric as well as the microscopic derivation of the Lindblad equation will be presented. Many reviews and books cover the topics of quantum dynamical semigroups and time evolution in open quantum systems. The following derivations are mostly guided by the book of Breuer and Petruccione [65] and an introductory article by Manzano [75]. The lecture notes of Alicki and Lendi and the review article by Alicki [76] provide an insight into the theory of quantum-dynamical semigroups. In the latter one the approaches to the problem that are called geometric and microscopic in this work are called axiomatic and constructive.

3.2. Geometric derivation of the Lindblad equation

The geometric approach coincides with the historical origins in the mentioned articles by Lindblad and Gorini, Kossakowski and Sudarshan [73], [74]. Therein the Lindblad equation arises due to general and mathematical considerations about the time propagation of a quantum system. Hence the structure of the Lindblad equation is the consequence of some very basic requirements for the time evolution of the density matrix. In [77] Pearle demonstrates very pedagogically how to derive the Lindblad equation based on those structural requirements. He postulates a linear behavior of the form

$$\rho_{ij}(t_0 + t) = \sum_{kl} a_{ij,kl} \rho_{kl}(t_0) \quad (3.4)$$

and analyzes the conditions imposed on the coefficients $a_{ij,kl}$. The above equation already establishes the Markovianity of the time evolution by assuming that the density matrix after a time step t can be written as a linear combination of matrix elements of the density matrix at time t_0 . By demanding Hermiticity and positivity for $\hat{\rho}(t_0 + t)$ and $\hat{\rho}(t_0)$, constraints can be imposed to the structure of $(a)_{ij,kl}$ and the Lindblad equation can be formulated. In the following however the historical pathway of a more abstract view on time evolution shall be reconstructed.

3.2.1. Time evolution - a dynamical map

To perform the time evolution of $\hat{\rho}$ an operator on the space of reduced density matrices $\rho(\mathcal{H}_S)$ is needed, that yields this density matrix at a later time. Such an

operator is called a dynamical map

$$\hat{\Lambda}_t : \rho(\mathcal{H}_S) \rightarrow \rho(\mathcal{H}_S), \quad \text{with} \quad \hat{\Lambda}_t \hat{\rho}(t_0) = \hat{\rho}(t_0 + t) . \quad (3.5)$$

By taking the density matrix $\hat{\rho}_0 = \hat{\rho}(t_0)$ at time t_0 to time $t_0 + t$ the dynamical map $\hat{\Lambda}_t$ performs a time step of length t . To ensure that the result $\hat{\Lambda}_t \hat{\rho}(t_0)$ is again a density matrix, the superoperator $\hat{\Lambda}_t$ has to be

- trace-preserving
- and completely positive.

A positive superoperator $\hat{\Lambda}_t$ maps a positive operator onto a positive operator.

$$\hat{\Lambda}_t \text{ is positive iff } \hat{A} \geq 0 \Rightarrow \hat{\Lambda}_t \hat{A} \geq 0, \quad \forall \hat{A} \in \rho(\mathcal{H}_S) . \quad (3.6)$$

However, in the scenario under consideration, wherein the system is coupled to a bath with arbitrary degrees of freedom, this condition is not enough. To account for the bath we need the stronger condition of complete positivity. Let $n \in \mathbb{N}$ be the dimension of the bath Hilbert space \mathcal{H}_B . We introduce a superoperator $\hat{\Lambda}_t \otimes \hat{\mathbb{1}}_n$, that maps positive operators of the composite system $\mathcal{H}_S \otimes \mathcal{H}_B$ to positive operators.

$$\hat{\Lambda}_t \text{ is completely positive iff } \hat{\Lambda}_t \otimes \hat{\mathbb{1}}_n \text{ is positive } \forall n \in \mathbb{N} . \quad (3.7)$$

If the parameter t is allowed to take variable positive values, $\{\hat{\Lambda}_t | t \geq 0\}$ becomes a one-parameter family of dynamical maps and describes the entire future of the system [78]. A quantum dynamical semigroup is defined as such a one-parameter family $\{\hat{\Lambda}_t | t \geq 0\}$ that additionally fulfills the *semigroup property*

$$\hat{\Lambda}_t + \hat{\Lambda}_s = \hat{\Lambda}_{t+s} . \quad (3.8)$$

This requirement is equivalent to claiming Markovianity for the corresponding system. A quantum dynamical semigroup thus describes systems with Markovian-type behavior. That means, the time evolution at a special time t is solely determined by the state of the system at this time t and does not depend on any earlier state of the system. This is why the time evolution from time 0 to time $t + s$ can be broken down into many shorter time steps in which each $\hat{\Lambda}_{t_i}$ does not contain information about any earlier state. In short, the system has no memory.

At this point already an implicit assumption about the nature of the external bath has been made. The system under consideration exhibits such Markovian-type behavior if the bath correlations vanish very fast compared to the timescale of the systems' time evolution. Only such a system without memory can be described by a quantum dynamical semigroup.

Using now the unitary time evolution of the total system (3.3) we already know the form of $\hat{\Lambda}_t$, which gives the time propagation of the total system density matrix

$$\hat{\rho}(t) = \hat{\Lambda}_t \hat{\rho}_0 = \text{tr}_B \hat{U} \hat{\omega}_0 \hat{U}^\dagger . \quad (3.9)$$

This expression, however, involves calculation within the total space \mathcal{H}_{tot} . Technically it is possible to derive a matrix representation of the map $\hat{\Lambda}_t$ already based on the unitary evolution within the total space given above, as demonstrated in [65]. Instead we follow the approach of [75] to exploit the complete positivity of the map. An extensive result about the exact form of the dynamical map is delivered by the Choi-Kraus theorem [79], [80]. It states that a map, as defined in (3.5), is completely positive and trace-preserving if and only if it can be expressed by Kraus operators $\hat{V}_i(t) \in \mathcal{B}(\mathcal{H}_S)$

$$\hat{\Lambda}_t \hat{\rho} = \sum_l \hat{V}_l^\dagger(t) \hat{\rho}_0 \hat{V}_l(t), \quad \text{with} \quad \sum_l \hat{V}_l(t) \hat{V}_l^\dagger(t) = \hat{\mathbb{1}}_{\mathcal{H}_S} . \quad (3.10)$$

The Kraus operators depend on the time parameter t . They are now expanded in terms of $\{\hat{F}_i\}_{i=1,\dots,d^2}$, an orthonormal basis of $\mathcal{B}(\mathcal{H}_S)$, the space of bounded operators on \mathcal{H}_S

$$\hat{V}_l(t) = \sum_{i=1}^{d^2} \langle\langle \hat{F}_i | \hat{V}_l(t) \rangle\rangle \hat{F}_i . \quad (3.11)$$

The scalar product of operators $\hat{A}, \hat{B} \in \mathcal{B}(\mathcal{H}_S)$ therein is defined as

$$\langle\langle \hat{A} | \hat{B} \rangle\rangle = \text{tr} [\hat{A}^\dagger \hat{B}] . \quad (3.12)$$

By inserting the expansion (3.11) into Equation (3.10) the map $\hat{\Lambda}_t$ becomes

$$\hat{\Lambda}_t \hat{\rho}_0 = \sum_{i,j=1}^{d^2} c_{ij}(t) \hat{F}_i \hat{\rho}_0 \hat{F}_j^\dagger \quad (3.13)$$

The time dependence is now included solely within the coefficients

$$c_{ij}(t) = \sum_l \langle\langle \hat{F}_i | \hat{V}_l(t) \rangle\rangle \langle\langle \hat{V}_l(t) | \hat{F}_j \rangle\rangle = \sum_l \text{tr} [\hat{F}_i^\dagger \hat{V}_l(t)] \text{tr} [\hat{V}_l^\dagger(t) \hat{F}_j] . \quad (3.14)$$

We choose the last element of the basis $\{\hat{F}_i\}_{i=1,\dots,d^2}$ to be proportional to the identity $\hat{F}_{d^2} = \frac{1}{\sqrt{d}} \hat{\mathbb{1}}_d$. As a consequence every other element of this basis has to have a vanishing trace to ensure the orthogonality of the basis elements. Due to the definition of the scalar product and the invariance of the trace upon permutations, the matrix of these coefficients $(c_{ij})_{i,j=1,\dots,d^2-1}$ is Hermitian and thus can be diagonalized. This property allows to find a diagonal representation in the next section.

3.2.2. The generator of a semigroup

Up to this point a dynamical map was established to perform a specific time step. However, the actual goal is to find a set of differential equations that describe the system's time evolution. This is only possible due to the Markovianity implicated by

the semigroup property (3.8). Under this condition one can find the generator $\hat{\mathcal{L}}$ of the semigroup, which gives the time evolution in terms of a differential equation

$$\frac{d}{dt}\hat{\rho}(t) = \hat{\mathcal{L}}\hat{\rho}(t) . \quad (3.15)$$

In the following the time argument of $\hat{\rho}$ will be omitted. Using the generator $\hat{\mathcal{L}}$, the dynamical map can also be expressed by means of an exponential $\hat{\Lambda}_{\Delta t} = e^{\hat{\mathcal{L}}\Delta t}$. But first of all an explicit and preferably simple form of the generator $\hat{\mathcal{L}}$ has to be found. This is achieved by inserting (3.13) into the left-hand side of Equation (3.15)

$$\frac{d}{dt}\hat{\rho} = \lim_{\Delta t \rightarrow 0} \frac{\Lambda_{\Delta t}\hat{\rho} - \hat{\rho}}{\Delta t} = \lim_{\Delta t \rightarrow 0} \frac{1}{\Delta t} \left(\sum_{i,j=1}^{d^2} c_{ij}(\Delta t) \hat{F}_i \hat{\rho} \hat{F}_j^\dagger - \hat{\rho} \right) . \quad (3.16)$$

The dependence on the time step Δt is contained solely in the prefactors and can be eliminated by performing the limit $\Delta t \rightarrow 0$. The new prefactors are

$$b_{ij} = \lim_{\Delta t \rightarrow 0} \frac{c_{ij}(\Delta t)}{\Delta t} . \quad (3.17)$$

Resulting from the construction of the operator basis, the double sum over its elements contains also summands with at least one operator \hat{F}_i or \hat{F}_j proportional to the unity operator. Therefore this sum is split into a sum with no basis element proportional to unity and two sums with either \hat{F}_i or \hat{F}_j proportional to unity. The remaining summand with $i, j = d^2$ is combined with the last term of (3.16) into the new coefficient

$$\tilde{b} = b_{d^2 d^2} - d . \quad (3.18)$$

By applying the specified segmentation, Equation (3.16) is rearranged to

$$\frac{d}{dt}\hat{\rho} = \sum_{i,j=1}^{d^2-1} b_{ij} \hat{F}_i \hat{\rho} \hat{F}_j^\dagger + \frac{1}{\sqrt{d}} \sum_{i=1}^{d^2-1} b_{id^2} \hat{F}_i \hat{\rho} + \frac{1}{\sqrt{d}} \sum_{j=1}^{d^2-1} b_{d^2 j} \hat{\rho} \hat{F}_j^\dagger + \frac{1}{d} \tilde{b} \hat{\rho} . \quad (3.19)$$

The second and third term can be further simplified by splitting into Hermitian and antihermitian parts and introducing an abbreviation

$$\hat{F} = \frac{1}{\sqrt{d}} \sum_{i=1}^{d^2-1} b_{id^2} \hat{F}_i = \frac{\hat{F} + \hat{F}^\dagger}{2} - i \frac{\hat{F}^\dagger - \hat{F}}{2i} = \hat{G} - i\hat{H} . \quad (3.20)$$

As both terms are complex conjugated of one another, their sum transforms to

$$\hat{F} \hat{\rho} + \hat{\rho} \hat{F}^\dagger = \{\hat{G}, \hat{\rho}\} - i[\hat{H}, \hat{\rho}] . \quad (3.21)$$

The last term of (3.19) is inserted into the anticommutator as follows

$$\{\hat{G}, \hat{\rho}\} = \{\hat{G} + \frac{\tilde{b}}{2d}, \hat{\rho}\} . \quad (3.22)$$

As a result the derivative of the density matrix can be expressed as

$$\frac{d}{dt}\hat{\rho} = \sum_{i,j=1}^{d^2-1} b_{ij}\hat{F}_i\hat{\rho}\hat{F}_j^\dagger + \{\hat{G}, \hat{\rho}\} - i[\hat{H}, \hat{\rho}]. \quad (3.23)$$

At this point we exploit the conservation of the trace of $\hat{\rho}$ under time evolution. Since the trace of a density matrix does not change, also the trace of its derivative vanishes $\text{tr}\left[\frac{d}{dt}\hat{\rho}(t)\right] = 0$. By using the cyclic property of the trace $\text{tr}[\hat{A}\hat{B}\hat{C}] = \text{tr}[\hat{B}\hat{C}\hat{A}]$, the commutator can be eliminated and the anticommutator can be simplified to

$$0 = \text{tr} \left[\left(\sum_{i,j=1}^{d^2-1} b_{ij}\hat{F}_j^\dagger\hat{F}_i + 2\hat{G} \right) \hat{\rho} \right]. \quad (3.24)$$

This holds true for every density matrix $\hat{\rho}$. By choosing a series of appropriate density matrices, one iteratively finds that every summand in (3.24) has to vanish separately. This leads to the replacement

$$\hat{G} = - \sum_{i,j=1}^{d^2-1} \frac{b_{ij}}{2} \hat{F}_j^\dagger \hat{F}_i \quad (3.25)$$

with which we arrive at the nondiagonal form of the Lindblad master equation

$$\hat{\mathcal{L}}\hat{\rho} = \frac{d}{dt}\hat{\rho} = \sum_{i,j=1}^{d^2-1} b_{ij} \left(\hat{F}_i\hat{\rho}\hat{F}_j^\dagger - \frac{1}{2}\{\hat{F}_j^\dagger\hat{F}_i, \hat{\rho}\} \right) - i[\hat{H}, \hat{\rho}]. \quad (3.26)$$

The coefficient matrix $B = (b_{ij})_{i,j=1,\dots,d^2-1}$ is the limit of the coefficient matrix (3.14). Therefore B is also Hermitian and diagonalizable and it exists a unitary matrix $U = (u_{ij})_{i,j=1,\dots,d^2-1}$ with

$$\Gamma = UBU^\dagger = \begin{pmatrix} \gamma_1 & 0 & 0 & 0 \\ 0 & \gamma_2 & 0 & 0 \\ 0 & 0 & \ddots & 0 \\ 0 & 0 & 0 & \gamma_{d^2-1} \end{pmatrix}. \quad (3.27)$$

Replacing

$$\hat{F}_i = \sum_{k=1}^{d^2-1} u_{ki} \hat{A}_k \quad (3.28)$$

finally yields the diagonal form of the generator $\hat{\mathcal{L}}$ and the Lindblad equation

$$\hat{\mathcal{L}}\hat{\rho} = \frac{d}{dt}\hat{\rho} = -i[\hat{H}, \hat{\rho}] + \sum_k \gamma_k \left(\hat{A}_k\hat{\rho}\hat{A}_k^\dagger - \frac{1}{2}\{\hat{A}_k^\dagger\hat{A}_k, \hat{\rho}\} \right). \quad (3.29)$$

This is the outcome of this section and the most general Markovian time evolution of a density matrix. The generator $\hat{\mathcal{L}}$ is called the Lindbladian and is a superoperator working on the space of density matrices $\rho(\mathcal{H}_S)$. The resulting time evolution

includes both coherent contributions within the first term, as well as incoherent dissipative contributions in the second term, the dissipator $\mathcal{D}(\hat{\rho})$. We merely imposed the conditions of Markovianity and the preservation of the density matrix' properties - positivity and unit trace. Any time evolution fulfilling these conditions can be written in form of (3.29). The physical meaning is achieved by the choice of appropriate operators \hat{A}_k and prefactors λ_k . They can be understood for example as jump operators and corresponding rates. The operator \hat{H} in (3.29) is not necessarily identical to the equilibrium Hamiltonian \hat{H}_S of the system. It simply describes the coherent part of the time evolution but can also contain contributions induced by interaction with the reservoir. Time evolution of the density matrix $\hat{\rho}_S$ generated by this first term, the commutator, always conserves energy. Whereas the second term, the anticommutator, simulates exchange of energy with an external bath and induces decoherences.

3.3. Microscopic derivation

The Lindblad equation (3.29) can also be derived without introducing the concept of quantum dynamical semigroups and their generators. As mentioned in the beginning of this chapter we start with the unitary time evolution of the total system (3.3) to perform the microscopic derivation. By applying several approximations and assumptions we will step by step receive Equation (3.29). The microscopic approach is more challenging than the geometrical approach with respect to involved mathematical considerations and manipulations. On the other hand the applied assumptions will be linked more directly to the underlying physical processes than within the more abstract geometrical approach. The following derivations can be found in similar form in an introductory article by Manzano [75] and more extensively in the book by Breuer and Petruccione [65].

First of all throughout the following derivation we assume to be in the weak-coupling limit. The interaction parameter α introduced in (2.69) is small compared to other energy scales of the system which corresponds to a relatively weak coupling between system and reservoir. We start the microscopic derivation with the von Neumann equation (3.3). It gives the derivative of the total systems' density matrix within the Schrödinger picture. In the Schrödinger picture the time evolution is entirely contained within the wave functions, whereas the operators do not change.¹ For the sake of simplicity we will change to the interaction picture from now on. In this case operators do change due to individual time evolution of system and bath respectively. Accordingly an operator $\hat{O} \in \mathcal{B}(\mathcal{H})$ written in the interaction picture is $\hat{O}(t) = e^{i(\hat{H}_S + \hat{H}_B)t} \hat{O} e^{-i(\hat{H}_S + \hat{H}_B)t}$. Whereas the state vectors experience a time evolution, which is caused by the interactions between system and reservoir. Within the interaction picture the density matrix changes according to

$$\frac{d}{dt} \hat{\omega}(t) = -i\alpha [\hat{H}_I(t), \hat{\omega}(t)] , \quad (3.30)$$

¹The operators are assumed to exhibit no explicit time dependence.

which after integration yields

$$\hat{\omega}(t) = \hat{\omega}(0) - i\alpha \int_0^t ds [\hat{H}_I(s), \hat{\omega}(s)] . \quad (3.31)$$

All following transformations are aiming at reducing the enormous complexity of this equation. Its intricacy arises firstly due to the calculation in the total Hilbert space and secondly due to the dependence of $\hat{\omega}(s)$ on all former times. To address the second problem we insert Equation (3.31) into Equation (3.30) and receive

$$\frac{d}{dt}\hat{\omega}(t) = -i\alpha [\hat{H}_I(t), \hat{\omega}(0)] - \alpha^2 \int_0^t ds [\hat{H}_I(t), [\hat{H}_I(s), \hat{\omega}(s)]] . \quad (3.32)$$

Repeating this procedure by changing the bounds of integration in (3.31) to t and s yields

$$\frac{d}{dt}\hat{\omega}(t) = -i\alpha [\hat{H}_I(t), \hat{\omega}(0)] - \alpha^2 \int_0^t ds [\hat{H}_I(t), [\hat{H}_I(s), \hat{\omega}(t)]] + \mathcal{O}(\alpha^3) . \quad (3.33)$$

The dependence on all previous states $\hat{\omega}(s)$ is now contained in $\mathcal{O}(\alpha^3)$. In the context of the weak-coupling limit a small interaction between system and bath is assumed and it is justified to neglect these terms of higher order in the interaction parameter. This approximation is a first step toward Markovianity.

As a next step we trace out the reservoir's degrees of freedom in order to avoid calculation in the total Hilbert space

$$\frac{d}{dt}\hat{\rho}(t) = -i\alpha \text{tr}_B [\hat{H}_I(t), \hat{\omega}(0)] - \alpha^2 \int_0^t ds \text{tr}_B [\hat{H}_I(t), [\hat{H}_I(s), \hat{\omega}(t)]] . \quad (3.34)$$

Despite of expression (3.34) being an equation for the reduced density matrix, calculations still have to be performed in the total Hilbert space. To address this problem a next approximation is implemented. We assume that at time $t=0$ there are no correlations between system and bath. At this point of time both subsystems did not yet interact or exhibit only very short-lived interactions. If this is the case the system and the bath are in a separable state

$$\hat{\omega}(0) = \hat{\rho}(0) \otimes \hat{\rho}_B(0) . \quad (3.35)$$

A further initial condition is imposed by assuming the bath to be in a thermal state at time $t=0$

$$\hat{\rho}_B(0) = \frac{e^{-\beta\hat{H}_B}}{\text{tr} e^{-\beta\hat{H}_B}} , \quad (3.36)$$

with the inverse thermal energy $\beta = 1/(k_B T)$. Also the interaction Hamiltonian can be decomposed into system operators $\hat{S}_i \in \mathcal{B}(\mathcal{H}_S)$ and bath operators $\hat{B}_i \in \mathcal{B}(\mathcal{H}_B)$

$$\hat{H}_I(t) = \sum_i \hat{S}_i(t) \otimes \hat{B}_i(t) . \quad (3.37)$$

Both, system and bath types of operators, act on different Hilbert subspaces and therefore each type commutes with one of the separable states of the total density matrix. As a consequence thereof the first term of expression (3.34) can be transformed according to

$$\mathrm{tr}_B [\hat{H}_I(t), \hat{\omega}(0)] = \sum_i \hat{S}_i(t) \hat{\rho}(0) \mathrm{tr}_B [\hat{B}_i(t) \hat{\rho}_B(0)] - \hat{\rho}(0) \hat{S}_i(t) \mathrm{tr}_B [\hat{\rho}_B(0) \hat{B}_i(t)] . \quad (3.38)$$

In a next step the expectation value of every bath operator $\langle \hat{B}_i \rangle = \mathrm{tr}_B [\hat{\rho}_B(0) \hat{B}_i(t)]$ is set to 0. This can be achieved by a simple transformation and is equivalent to shifting the energies scale by a constant amount. As a consequence expression (3.38) and thereby also the first term of Equation (3.34) vanishes. The time evolution of the reduced density matrix is now solely determined by the second term of (3.34), an integration which still contains the total density matrix.

The bath is infinitely large compared to the system, hence its eigenstates are negligibly affected during the interaction with the system. This assumption is justified especially for a very small coupling parameter α . Consequently correlations between system and bath are very short-lived. Excitations of the bath have to relax on a timescale that is very small compared to the characteristic timescale of the system $\tau_B \ll \tau_{\mathrm{sys}}$. Under these conditions the bath stays in its initial thermal state and at every time the total density matrix is separable

$$\hat{\omega}(t) = \hat{\rho}(t) \otimes \hat{\rho}_B(0) . \quad (3.39)$$

This is called the Born or factorization approximation and is a very common concept of quantum Markovianity [81], [82]. The underlying assumption however implies that the system's time evolution can not be resolved for timescales on the order of magnitude of the bath correlations τ_B . In this manner the Born approximation limits the temporal resolution of the simulation such that we can just track processes on a timescale that is rather coarse compared to τ_B .

By applying the previous approximation, Equation (3.34) can be written as

$$\frac{d}{dt} \hat{\rho}(t) = -\alpha^2 \int_0^t ds \mathrm{tr}_B [\hat{H}_I(t), [\hat{H}_I(s), \hat{\rho}(t) \otimes \hat{\rho}_B(0)]] . \quad (3.40)$$

This expression still depends on the complete history of the interaction Hamiltonian and the initial state of the bath. By neglecting higher order terms $\mathcal{O}(\alpha^3)$ already all terms related to the history of $\hat{\rho}(s)$ were eliminated. Proceeding towards Markovianity, we rewrite the integration by substituting the integration variable s by $t - s$ and extending the upper limit of the integration to infinity. This extension is valid only if the integrand vanishes fast enough for $s \gg \tau_B$. This condition is fulfilled under the same circumstances as discussed before, namely that the timescale of variations within the system state is much larger than the timescale of bath correlations. The result is the so-called Redfield equation [83]

$$\frac{d}{dt} \hat{\rho}(t) = -\alpha^2 \int_0^\infty ds \mathrm{tr}_B [\hat{H}_I(t), [\hat{H}_I(t-s), \hat{\rho}(t) \otimes \hat{\rho}_B(0)]] . \quad (3.41)$$

Together the above transformations are called the Born-Markov-approximation. Despite being Markovian now, Equation (3.41) does not necessarily preserve the positivity of the density matrix $\hat{\rho}$ and thus does not describe the generator of a dynamical semigroup. On that account the rotating wave approximation is performed to average over rapidly oscillating terms. To eliminate the dependence on s within relevant system dynamics contained in the system operators \hat{S}_i , the decomposition (3.37) is applied. This allows to separate system dynamics and integration and to condense the latter one into a prefactor. In order to rewrite the interaction Hamiltonian we first define the commutator with the system Hamiltonian as superoperator $\hat{M}\hat{O} = [\hat{H}_S, \hat{O}]$, $\forall \hat{O} \in \mathcal{B}(\mathcal{H}_S)$. The decomposition of the interaction Hamiltonian \hat{H}_I (3.37) is also valid in the Schrödinger picture. To omit the time dependence we take the system operators \hat{S}_i within the Schrödinger picture and decompose them further into eigenoperators of the superoperator \hat{M}

$$\hat{S}_i = \sum_{\omega} \hat{S}_i(\omega) \quad \text{with} \quad \hat{S}_i(\omega) = \sum_{\epsilon' - \epsilon = \omega} \Pi(\epsilon) \hat{S}_i \Pi(\epsilon'). \quad (3.42)$$

ϵ, ϵ' are energy eigenvalues of H_S and $\Pi(\epsilon), \Pi(\epsilon')$ are projections onto the corresponding eigenspaces. Due to this definition the operators $\hat{S}_i(\omega)$ are eigenoperators of the commutator \hat{M} and the energy differences ω are their corresponding eigenvalues. They satisfy the following relations

$$[\hat{H}_S, \hat{S}_i(\omega)] = -\omega \hat{S}_i(\omega) \quad (3.43)$$

$$[\hat{H}_S, \hat{S}_i^\dagger(\omega)] = +\omega \hat{S}_i^\dagger(\omega). \quad (3.44)$$

Transforming these expressions back into the interaction picture yields

$$e^{i\hat{H}_S t} \hat{S}_i(\omega) e^{-i\hat{H}_S t} = e^{-i\omega t} \hat{S}_i(\omega) \quad (3.45)$$

$$e^{i\hat{H}_S t} \hat{S}_i^\dagger(\omega) e^{-i\hat{H}_S t} = e^{+i\omega t} \hat{S}_i^\dagger(\omega). \quad (3.46)$$

These relations are used to rewrite the interaction Hamiltonian and modify Equation (3.41) as demonstrated in appendix A.2. The effect of the bath and the dependence on the integration variable can now be separated into the factor

$$\Gamma_{ij}(\omega) = \alpha^2 \text{tr}_B \int_0^\infty ds e^{i\omega s} \text{tr}_B \left[\hat{B}_i^\dagger(t) \hat{B}_j(t-s) \hat{\rho}_B(0) \right]. \quad (3.47)$$

It contains the dependence of the bath on the history of the time evolution. By inserting (3.47) into Equation (A.7) the Redfield equation (3.41) is transformed to

$$\begin{aligned} \frac{d}{dt} \hat{\rho}(t) = & \sum_{\substack{i,j \\ \omega, \omega'}} \left(e^{i(\omega' - \omega)t} \Gamma_{ij}(\omega) \left[\hat{S}_j(\omega) \hat{\rho}(t), \hat{S}_i^\dagger(\omega') \right] \right. \\ & \left. + e^{i(\omega - \omega')t} \Gamma_{ji}^*(\omega) \left[\hat{S}_j(\omega'), \hat{\rho}(t) \hat{S}_i^\dagger(\omega) \right] \right). \end{aligned} \quad (3.48)$$

The factor Γ_{ij} can be understood as the one-sided Fourier-transform of the reservoir correlation functions $\langle \hat{\mathbf{B}}_j^\dagger(t) \hat{\mathbf{B}}_i(t-s) \rangle = \text{tr}_{\mathbf{B}} \left[\hat{\mathbf{B}}_j^\dagger(t) \hat{\mathbf{B}}_i(t-s) \hat{\rho}_{\mathbf{B}}(0) \right]$. Earlier on we declared $\hat{\rho}_{\mathbf{B}}(0)$ to be a stationary state of the bath. Therefore it commutes with the bath Hamiltonians contained in $\hat{\mathbf{B}}_i(t) = e^{i\hat{H}_{\mathbf{B}}t} \hat{\mathbf{B}}_i e^{-i\hat{H}_{\mathbf{B}}t}$. This implies that the reservoir correlation function is homogeneous in time $\langle \hat{\mathbf{B}}_j^\dagger(t) \hat{\mathbf{B}}_i(t-s) \rangle = \langle \hat{\mathbf{B}}_j^\dagger(s) \hat{\mathbf{B}}_i(0) \rangle$ and does only depend on the time difference s . The heat bath represented by the factor Γ_{ij} is therefore completely independent of the actual time t . Again this conclusion does only hold if the reservoir correlation functions are decaying sufficiently fast, just as postulated when introducing the Born approximation. The presented approximation is exact in the limit of an infinitely large reservoir with a continuum of frequencies. However, in case of discrete frequencies we can not necessarily assume the bath correlations to decay sufficiently fast. To perform the rotating wave approximation we analyze the frequency difference in the exponential of (3.48). In case of unlike values $\omega \neq \omega'$ the terms in (3.48) are oscillating much faster than the typical timescale τ_{sys} of the system and do not contribute to the evolution of the system. Especially in the limit of weak coupling $\alpha \rightarrow 0$ it is $|\omega - \omega'| \gg \alpha^2$ and these terms can be neglected because they are oscillating on the timescale $\tau_{\mathbf{B}}$ of the bath. Since we only keep the resonant, or secular, terms of Equation (3.48), with $\omega = \omega'$, the rotating wave approximation is also called the secular approximation. It yields

$$\frac{d}{dt} \hat{\rho}(t) = \sum_{i,j,\omega} \left(\Gamma_{ij}(\omega) \left[\hat{\mathbf{S}}_j(\omega) \hat{\rho}(t), \hat{\mathbf{S}}_i^\dagger(\omega) \right] + \Gamma_{ji}^*(\omega) \left[\hat{\mathbf{S}}_j(\omega), \hat{\rho}(t) \hat{\mathbf{S}}_i^\dagger(\omega) \right] \right). \quad (3.49)$$

Similar to procedure (3.20) in the geometric derivation, we now separate coherent and non-coherent time evolution of the system by splitting the prefactor (3.47) into Hermitian and antihermitian parts

$$\Gamma_{ij}(\omega) = \frac{1}{2} (\Gamma_{ij}(\omega) + \Gamma_{ji}^*(\omega)) - i \frac{1}{2} (\Gamma_{ij}(\omega) - \Gamma_{ji}^*(\omega)) = \frac{1}{2} \gamma_{ij}(\omega) + i \pi_{ij}(\omega). \quad (3.50)$$

According to this definition the coefficient matrices π_{ij} and γ_{ij} are Hermitian and as the Fourier transform of a positive function the coefficient matrix

$$\gamma_{ij}(\omega) = \gamma_{ji}^*(\omega) = \alpha^2 \int_{-\infty}^{\infty} ds e^{i\omega s} \langle \hat{\mathbf{B}}_i^\dagger(t) \hat{\mathbf{B}}_j(t-s) \rangle \quad (3.51)$$

is also positive. Inserting decomposition (3.50) into (3.49) gives the time evolution in the interaction picture

$$\begin{aligned} \frac{d}{dt} \hat{\rho}(t) = \sum_{i,j,\omega} \left(\gamma_{ij}(\omega) \left(\hat{\mathbf{S}}_j(\omega) \hat{\rho}(t) \hat{\mathbf{S}}_i^\dagger(\omega) - \frac{1}{2} \left\{ \hat{\mathbf{S}}_i^\dagger(\omega) \hat{\mathbf{S}}_j(\omega), \hat{\rho}(t) \right\} \right) \right. \\ \left. - i \pi_{ij}(\omega) \left[\hat{\mathbf{S}}_i^\dagger(\omega) \hat{\mathbf{S}}_j(\omega), \hat{\rho}(t) \right] \right). \end{aligned} \quad (3.52)$$

The above expression can easily be transformed back into the Schrödinger picture by adding the system Hamiltonian $\hat{H}_{\mathbf{S}}$ to $\hat{H}_{\text{LS}} = \sum_{i,j,\omega} \pi_{ij}(\omega) \hat{\mathbf{S}}_i^\dagger(\omega) \hat{\mathbf{S}}_j(\omega)$, the

Hamiltonian-like term within the time evolution. This is allowed due to the definition of the operators $S_i(\omega)$ in (3.42). As a result of the properties (3.43) and (3.44) the Hermitian operator \hat{H}_{LS} commutes with \hat{H}_S . \hat{H}_{LS} is called the Lamb shift Hamiltonian and leads to a renormalization of the initial unperturbed energy levels of the system due to the coupling to the external bath. By thus transforming Equation (3.52) back to the Schrödinger picture and condensing the notation of Hermitian and dissipative time evolution we finally arrive at the well-known form of the Lindblad equation

$$\frac{d}{dt}\hat{\rho}(t) = \hat{\mathcal{L}}\hat{\rho}(t) = -i[\hat{H}_{\text{LS}} + \hat{H}_S, \hat{\rho}(t)] + \hat{\mathcal{D}}(\hat{\rho}(t)). \quad (3.53)$$

The last term of Equation (3.53)

$$\hat{\mathcal{D}}(\hat{\rho}(t)) = \sum_{i,j,\omega} \gamma_{ij}(\omega) \left(\hat{S}_j(\omega)\hat{\rho}(t)\hat{S}_i^\dagger(\omega) - \frac{1}{2} \left\{ \hat{S}_i^\dagger(\omega)\hat{S}_j(\omega), \hat{\rho}(t) \right\} \right) \quad (3.54)$$

contains the noncoherent time evolution and is called the dissipator. In a last step the above expression is diagonalized analogously to the procedure presented in the geometric derivation. This is possible due to the positivity of the coefficient matrix γ_{ij} . Finally only one relevant frequency ω has to be considered and the dependence on the frequency can be omitted. This results, together with the diagonalization, in a Lindblad equation of the standard form (3.29).

3.4. The Lindblad equation for a d -level system

In this section the so far still abstract Lindblad equation shall be adapted to the tight-binding model and the corresponding occupation matrix \mathbf{P} presented in the previous chapter. We will introduce a set of jump operators and corresponding transition probabilities to present a specific numeric form of the dissipator. In our model the object of time evolution will not be a density matrix but an occupation matrix \mathbf{P} . Since both objects only differ by a factor, in principle the same equations as presented before apply also for the occupation matrix. However, as already mentioned, some modifications are necessary to preserve the Pauli principle.

Let us commence now with a dissipator similar to (3.54), but in diagonal form $\gamma_{ij} = \delta_{ij}\gamma_i$ and without frequency dependence. Let furthermore as before d refer to the number of eigenstates in the system, the dimension of the Hilbert space. To describe the equilibration mediated by an external bath we choose jump operators

$$\hat{S}_i = \hat{F}_{nm} = |n\rangle\langle m|, \quad n, m = 1, \dots, d. \quad (3.55)$$

Each operator \hat{F}_{nm} describes a transition of a particle from state m into state n . And each such operator adds a summand to the dissipator. The explicit structure of an individual summand is given by adapting a specific jump operator and the

occupation matrix (2.67) to the parenthesized term in (3.54)

$$\begin{aligned}\hat{L}_{nm} &= \hat{F}_{nm} \hat{P} \hat{F}_{nm}^\dagger - \frac{1}{2} (\hat{F}_{nm}^\dagger \hat{F}_{nm} \hat{P} + \hat{P} \hat{F}_{nm}^\dagger \hat{F}_{nm}) \\ &= p_{mm} |n\rangle \langle n| - \frac{1}{2} \sum_i (p_{mi} |m\rangle \langle i| + p_{im} |i\rangle \langle m|) .\end{aligned}\tag{3.56}$$

The time dependence of \hat{P} is omitted in favor of a compact notation. Written as a matrix \hat{L}_{nm} has just two nonzero diagonal elements ($\hat{L}_{nm})_{nn} = p_{mm} = -(\hat{L}_{nm})_{mm}$

$$\hat{L}_{nm} = \begin{matrix} & \begin{matrix} n & m \end{matrix} \\ \begin{matrix} n \\ m \end{matrix} & \begin{pmatrix} 0 & & & -\frac{1}{2}p_{1m} \\ & \ddots & & \\ & & p_{mm} & -\frac{1}{2}p_{nm} \\ & & 0 & \vdots \\ -\frac{1}{2}p_{m1} & \dots & -\frac{1}{2}p_{mn} & \dots & -p_{mm} & \dots \\ & & & & \vdots & \\ & & & & -\frac{1}{2}p_{dm} & 0 \end{pmatrix} .\end{matrix}\tag{3.57}$$

Since the diagonal elements of the occupation matrix represent the eigenstate occupation numbers, the diagonal elements in the matrix form of the generator $\hat{\mathcal{L}}(\hat{P})$ represent the change of the eigenstate occupations. In the demonstrated case of a jump from state m to state n , the occupation in state m is reduced and the same amount of occupation is added to state n . In this way the dissipator is traceless and the number of particles in the system is conserved.

The offdiagonal elements of the occupation matrix represent coherent superpositions of different states, which are a characteristic feature of quantum mechanical systems. The matrix \hat{L}_{nm} , as contribution of the jump \hat{F}_{nm} to the dissipator, has nonzero offdiagonal elements within the m th column and the m th row, implying decreasing coherence of state m with all other states. This reduction of coherences is called dephasing and involves a reduction of quantum phenomena such as interference effects.

Each summand in (3.54) corresponds to a matrix \hat{L}_{nm} that incorporates a specific jump \hat{F}_{nm} into the time evolution of the quantum system. The total dissipator is the sum of all of these jump contributions each weighted with an individual prefactor γ_{nm} . This weighting factor γ_{nm} of each jump $m \rightarrow n$ indicates the rate or probability of the corresponding process as well as the coupling to the heat bath. The bath is assumed to be composed of bosons, for example phonons or magnons. In the previous section the bath was preassigned to be in a thermal state. Therefore it is characterized by a Bose-Einstein distribution

$$f_{\text{BE}}(\Delta\mathcal{E}, \mu, T) = \frac{1}{e^{(\Delta\mathcal{E}-\mu)/k_{\text{B}}T} - 1} ,\tag{3.58}$$

which also determines the transition probability γ_{nm} . The temperature T of the bosonic heat bath defines the ambient temperature in a simulation. In equilibrium

it coincides with the temperature of the Fermi-Dirac distribution of the electronic occupation numbers. The energy difference $\Delta\mathcal{E}$ is the amount of energy that is exchanged between the system and the heat bath. It corresponds to the energy that is absorbed or emitted during the jump \hat{F}_{nm} and therefore is defined by the energy difference $\Delta\mathcal{E} = |\mathcal{E}_n - \mathcal{E}_m|$ of the corresponding eigenstates. The chemical potential of the bosons is usually set to a value infinitesimally below zero to avoid numerical problems in case of a vanishing energy difference. For a jump with a small energy difference the distribution yields a very high value – there are more bosons available than for jumps between eigenstates with distant eigenenergies. While in the first case the jump F_{nm} happens with a very high probability γ_{nm} , it will hardly ever happen in the latter case.

Now we have to revisit Section 2.3 and the discussion about N_e -representability. As the system is described by the occupation matrix, there is effectively just one particle in the system whose particle number is scaled up to N_e , the total number of particles in the simulation. There is no interaction between the different electrons included in this simulation. Therefore compliance with the Pauli principle (2.68) has to be ensured artificially. Within our model with mean occupation numbers this is realized by an additional scaling factor entering the transition rate γ_{nm} . As well established within e.g. the Boltzmann theory, the probability of a transition is increased with higher occupation of the initial state m and reduced by higher occupation in the final state n . In case of a fully occupied final state the transition is prohibited by the Pauli blocking factor

$$\pi_{nm}(t) = p_{mm}(t)(1 - p_{nn}(t)) . \quad (3.59)$$

Similar blocking factors are used in a Lindblad equation in [84]. The implications of such scattering rates will be briefly discussed in Section 3.4.1.

Finally also the different spin character of states m and n has to be taken into account. To differentiate between spin-flip and spin conserving transitions the spin alignment of both eigenstates has to be incorporated. Therefore two different transition probabilities γ_{sf} and γ_{sc} are introduced. They can be understood as rates for spin conserving or spin-flip scattering events, respectively. The spin-dependent transition probability between two states with s_n and s_m , as degree of spin polarization along z -direction, is defined as

$$\gamma_{\text{spin}} = \frac{1 + s_n \cdot s_m}{2} \gamma_{sc} + \frac{1 - s_n \cdot s_m}{2} \gamma_{sf} . \quad (3.60)$$

Combining these three ingredients - Bose-Einstein distribution, Pauli blocking, and spin-dependent scattering rate yields [23]

$$\gamma_{nm}(t) = \begin{cases} \gamma_{\text{spin}} \pi_{nm}(t) [f_{\text{BE}}(\Delta\mathcal{E}, \mu, T) + 1] & \mathcal{E}_m > \mathcal{E}_n \\ \gamma_{\text{spin}} \pi_{nm}(t) f_{\text{BE}}(\Delta\mathcal{E}, \mu, T) & \mathcal{E}_m < \mathcal{E}_n \\ \gamma_{\text{dp}} & n = m \end{cases} \quad (3.61)$$

This definition includes a distinction between de-excitation and excitation depending on the relation of initial and final energy. In a scattering-process picture this translates into emitting and absorbing a boson. Between both cases the boson occupation factor differs by 1. The first case is associated with a transition from a higher energy level to a lower energy level. Thereby the electron system loses energy which is transferred to the bosonic bath. Vice versa this holds for an excitation process. Both, excitation and de-excitation processes, happen simultaneously but with individual rates differing by the occupation factor and the Pauli blocking. Therefore the coupling to an external bath in form of the dissipator does not just allow to include the loss of the laser energy from the electronic system to the heat bath. Even more it enables an exchange of energy that leads to thermalization of the system. Starting with an arbitrary artificial occupation of the electron system the interaction with the bath will bring the system back to a Fermi-Dirac occupation with a temperature T defined by the heat bath.

The definition (3.61) contains also the rates γ_{nn} , pertaining to the operator \hat{F}_{nn} . In this particular case it does not represent a jump but instead a transition from state n back into state n . As evident from (3.57) the associated matrix \hat{L}_{nn} is traceless, the occupation of the eigenstates is unchanged and the system energy is conserved. However, the offdiagonal elements of the occupation matrix are reduced. As mentioned before this process is called dephasing and since in this case the diagonal elements are not affected it is a pure dephasing. It takes place on an individual timescale defined by the parameter γ_{dp} .

Including all previous definitions the total dissipator is the sum of all real and improper transition processes (3.56) and their individual weighting

$$\hat{\mathcal{D}}(\hat{P}(t)) = \sum_{nm} \gamma_{nm} \hat{L}_{nm} . \quad (3.62)$$

Eventually, the equation of motion is now given by

$$\frac{d}{dt} \hat{P}(t) = -i [\hat{H}(t), \hat{P}(t)] + \hat{\mathcal{D}}(\hat{P}(t)) . \quad (3.63)$$

The optical excitation is included in the time-dependent Hamiltonian $\hat{H}(t)$ according to one of the demonstrated procedures (2.31) or (2.44) and yields a coherent time evolution.

3.4.1. Nonlinear quantum master equations

To enforce the Pauli principle we introduced Boltzmann-like weighting factors (3.59). These depend on the time-dependent occupation numbers $p_{ii}(t)$, and with this the Lindbladian for the time-dependent occupation matrix depends on the occupation matrix itself. Consequently, the generator of the associated time evolution is no longer linear. Instead the generator is of a parametric Lindblad form [65]

$$\frac{d}{dt} \hat{\rho}(t) = \hat{\mathcal{L}}[\hat{\rho}(t)] \hat{\rho}(t) . \quad (3.64)$$

For each fixed density matrix $\hat{\rho}$ this equation is a Lindblad-type master equation and its generator $\hat{\mathcal{L}}$ depends on the density matrix. The existence of a unique solution is discussed by Alicki and Messer [85]. They formulate certain conditions to the boundedness of the generator $\hat{\mathcal{L}}$. As defined in Section 3.2.1 the solutions are represented by a one-parameter family of nonlinear maps. Again these maps have to be trace-preserving, fulfill the semigroup property and be continuous in t for every $\hat{\rho}$.

Nonlinear master equations emerge especially in the context of mean-field approaches. If, like in our case, a many-body system is approximated by a one-particle density matrix, the dynamics of this one-particle density matrix is described by a nonlinear master equation. Also the quantum Boltzmann equation can be expressed in a parametric Lindblad form. For example Rosati et al. [84] derive a Boltzmann-type scattering equation by using a nonlinear Lindblad superoperator.

3.5. Charge and spin currents

To obtain an expression for currents within the presented model we follow a derivation by Mahan [55]. Since there is no direct representation of velocities within the model, we will instead use the polarization operator

$$\hat{\mathbf{P}} = \int d^3r \hat{\mathbf{r}} \hat{\rho}_c(\mathbf{r}) . \quad (3.65)$$

By inserting the continuity equation for the charge density ρ_c

$$\frac{\partial}{\partial t} \rho_c(\mathbf{r}, t) = -\nabla \cdot \hat{\mathbf{j}}(\mathbf{r}, t) \quad (3.66)$$

its time derivative is connected to the particle current

$$\frac{\partial}{\partial t} \hat{\mathbf{P}} = - \int d^3r \hat{\mathbf{r}} \nabla \cdot \hat{\mathbf{j}}(\mathbf{r}, t) = -(\hat{\mathbf{j}}(\mathbf{r}, t) \mathbf{r})|_{-\infty}^{\infty} + \int d^3r \hat{\mathbf{j}}(\mathbf{r}, t) \nabla \mathbf{r} = \hat{\mathbf{j}}(t) . \quad (3.67)$$

The first term vanishes assuming symmetric boundary conditions with equal incoming and outgoing currents into the sample. Within the tight-binding model the polarization operator comprises a sum over sites \mathbf{R}_i , each with its individual mean occupation numbers. Using second quantization the polarization operator and the tight-binding Hamiltonian are defined as

$$\hat{\mathbf{P}} = \sum_i \mathbf{R}_i \hat{c}_i^\dagger \hat{c}_i \quad (3.68)$$

and

$$\hat{H} = \sum_{kl} t_{kl} \hat{c}_l^\dagger \hat{c}_k , \quad (3.69)$$

with the matrix elements $t_{kl} = \langle k | \hat{H} | l \rangle$ and creation and annihilation operators \hat{c}_l^\dagger and \hat{c}_l of an electron at site l . $\hat{c}_l^\dagger \hat{c}_l$ is thus the corresponding number operator. The

current can now be calculated as the time evolution of the polarization operator

$$\begin{aligned}\hat{\mathbf{j}} &= \frac{i}{\hbar} [\hat{\mathbf{H}}, \hat{\mathbf{P}}] = \frac{i}{\hbar} \sum_{kli} \left(t_{kl} \hat{c}_l^\dagger \hat{c}_k \hat{c}_i^\dagger \hat{c}_i \mathbf{R}_i - \mathbf{R}_i \hat{c}_i^\dagger \hat{c}_i \hat{c}_l^\dagger \hat{c}_k t_{kl} \right) \\ &= \frac{i}{\hbar} \sum_{kl} t_{kl} \hat{c}_l^\dagger \hat{c}_k (\mathbf{R}_k - \mathbf{R}_l) .\end{aligned}\quad (3.70)$$

The above summation includes all sites and therefore gives the total current. To obtain the specific current from \mathbf{R}_k to \mathbf{R}_l the summation has to be restricted to the orbitals located at these sites. At this point the single index is replaced by an extended index $k \rightarrow (k i \sigma)$ to represent site, orbital and spin separately. Switching back to Dirac notation the current from site k to site l reads

$$\hat{\mathbf{j}}_{lk} = \frac{i}{\hbar} \sum_{i\sigma, j\sigma'} |li\sigma\rangle t_{li\sigma, kj\sigma'} \langle kj\sigma'| (\mathbf{R}_l - \mathbf{R}_k) . \quad (3.71)$$

Since $t_{kl} = t_{lk}^*$ and $p_{kl} = p_{lk}^*$ due to the Hermiticity of Hamiltonian and occupation matrix, we arrive at the condensed expression

$$\begin{aligned}\mathbf{J}_{lk} = \langle \hat{\mathbf{j}}_{lk} \rangle &= \frac{i}{2\hbar} \left[\sum_{i\sigma, j\sigma'} p_{kj\sigma', li\sigma} t_{li\sigma, kj\sigma'} (\mathbf{R}_l - \mathbf{R}_k) + \sum_{j\sigma', i\sigma} p_{li\sigma, kj\sigma'} t_{kj\sigma', li\sigma} (\mathbf{R}_k - \mathbf{R}_l) \right] \\ &= -\frac{(\mathbf{R}_l - \mathbf{R}_k)}{\hbar} \sum_{i\sigma, j\sigma'} \text{Im} [p_{kj\sigma', li\sigma} t_{li\sigma, kj\sigma'}] .\end{aligned}\quad (3.72)$$

If only spin conserving hoppings are taken into account, which is a reasonable assumption for collinear systems, this expression reduces further to a sum over pure spin-up and spin-down currents

$$\mathbf{J}_{lk} = -\frac{(\mathbf{R}_l - \mathbf{R}_k)}{\hbar} \sum_{ij} \text{Im} [p_{kj\uparrow, li\uparrow} t_{li\uparrow, kj\uparrow} + p_{kj\downarrow, li\downarrow} t_{li\downarrow, kj\downarrow}] . \quad (3.73)$$

From here on we can proceed to formulate spin currents. A proper definition of a spin current and its continuity equation is however not trivial because the spin is not a conserved quantity [86], [87]. Here we will proceed with the common definition of a spin current

$$\mathbf{J}_{lk}^\mu = \frac{1}{2} \langle \Sigma_\mu \hat{\mathbf{j}}_{lk} + \hat{\mathbf{j}}_{lk} \Sigma_\mu \rangle , \quad (3.74)$$

with the Pauli matrices Σ_μ , $\mu = x, y, z$. Using matrix notations

$$\left(\mathbf{p}_{kl}^{\sigma\sigma'} \right)_{\alpha\beta} = p_{k\alpha\sigma, l\beta\sigma'} \quad \text{and} \quad \left(\mathbf{t}_{kl}^{\sigma\sigma'} \right)_{\alpha\beta} = t_{k\alpha\sigma, l\beta\sigma'} \quad (3.75)$$

one arrives at a compact formulation

$$\mathbf{J}_{lk}^\mu = \frac{i}{4\hbar} (\mathbf{R}_l - \mathbf{R}_k) \text{tr} \left(\begin{array}{cc} \mathbf{p}_{kl}^{\uparrow\uparrow} & \mathbf{p}_{kl}^{\uparrow\downarrow} \\ \mathbf{p}_{kl}^{\downarrow\uparrow} & \mathbf{p}_{kl}^{\downarrow\downarrow} \end{array} \right) \left\{ \Sigma_\mu, \left(\begin{array}{cc} \mathbf{t}_{lk}^{\uparrow\uparrow} & \mathbf{t}_{lk}^{\uparrow\downarrow} \\ \mathbf{t}_{lk}^{\downarrow\uparrow} & \mathbf{t}_{lk}^{\downarrow\downarrow} \end{array} \right) \right\}_+ + (k \leftrightarrow l) . \quad (3.76)$$

The trace includes also all orbital indices. The resulting sums contain spin-mixing elements within the occupation $\mathbf{p}_{kl}^{\sigma\sigma'}$ or within the hopping component $t_{kl}^{\sigma\sigma'}$. In particular currents \mathbf{J}_{lk}^x and \mathbf{J}_{lk}^y are composed of such spin-mixed summands.

Throughout this work we maintain a scenario of collinear spins aligned along the z -axis and neglect all spin-mixing contributions $\sigma \neq \sigma'$. As a consequence the spin current vanishes for $\mu = x, y$. This corresponds to the intuitive two-current picture. Results of EVOLVE beyond two-current approximation are published in [88]. However, in the present work the spin current takes a form similar to the charge current (3.73), it is not the sum but the difference of spin-up and spin-down currents

$$\mathbf{J}_{lk}^z = -\frac{(\mathbf{R}_l - \mathbf{R}_k)}{\hbar} \text{Im} \sum_{\alpha\beta} (p_{k\alpha\uparrow, l\beta\uparrow} t_{l\beta\uparrow, k\alpha\uparrow} - p_{k\alpha\downarrow, l\beta\downarrow} t_{l\beta\downarrow, k\alpha\downarrow}) . \quad (3.77)$$

The direction of the current is specified by the sign of the resulting sum and the vector between sites k and l . Expressions (3.73) and (3.77) contain the hopping parameters and the delocalized occupation between orbitals at different sites. In contrast, the more conventional definition of currents uses the velocity instead. Within our model we do not have access to velocities as it is a simulation of occupation at fixed orbitals and not a simulation of moving particles. Nevertheless the above derivation is valid on its own and the connection from hopping and delocalized occupation to velocity is just a question of interpretation.

4. Results

4.1. Technical and numerical details

To construct a system, at first its geometry has to be defined, like illustrated in Figure 2.1. An appropriate number of cells along the respective lattice vectors, the boundary conditions as well as the atomic positions within the cell have to be chosen. In the following mostly an fcc lattice is used to simulate Co or CoCu layers. To model CoCu layers with a (100) interface and magnetization parallel to this interface [89] a tetragonal two-atomic unit cell is applied. Its lattice vectors in terms of the lattice constant a are

$$\begin{aligned} a_1 &= (a, 0, 0), & a_2 &= (0, -a/2, a/2) & \text{and} & & a_3 &= (0, a/2, a/2) \\ \text{with basis atoms at } & b_1 &= (0, 0, 0) & \text{and} & b_2 &= (a/2, 0, a/2) . \end{aligned} \quad (4.1)$$

Next the Slater-Koster-parameters and the number of electrons have to be defined to simulate a specific material. The Slater-Koster-parameters are obtained by fitting the tight-binding to an *ab initio* band structure. This is either realized with home-made data and code or by using values from literature [40]. The interface hopping parameters between orbitals of different atomic character are chosen as the mean values of corresponding neighboring atoms in first approximation.

The parameters for SOC of d orbitals are chosen in comparison to ab-initio calculations for Co and Cu. For other materials parameters from literature were used [40], [90], [91]. The influence of SOC of p orbitals was assumed to be negligible.

The chosen geometry does not just affect the possibility to observe extended phenomena like currents throughout the system. It also directly affects the magnetization, excitation and relaxation. This is due to the increasing number of eigenstates with increasing number of sites. The simulation of just one atom with periodic boundary conditions yields the eigenenergies at the Γ -point of the corresponding band structure. By adding more and more sites new eigenvalues emerge belonging to higher \mathbf{k} -values. This way gradually the band structure is sampled and more eigenenergies become accessible. A dense spectrum of eigenstates is necessary to properly simulate demagnetization and relaxation of large systems. The dynamics can also be affected by exclusion of hoppings between special orbital pairs due to a restriction in the system geometry. For all these reason it is essential to choose an appropriate geometry and a sufficient system size.

The available eigenstates are filled by a fixed number of electrons from lowest to highest energy, according to the Fermi-Dirac distribution. The Fermi-Dirac distribution emerges automatically by interaction with a thermal heat bath of the given temperature.

To include laser excitation the pulse length, strength, polarization, angle of incidence and excited sites or orbitals have to be defined. In general we apply a laser with a pulse width of $\tau = 10$ fs and a photon energy of $\hbar\omega = 1.55$ eV. These values were chosen based on common experimental setups [17], [92]. The electric field amplitudes were chosen as to generate a number of excited electrons compatible to experiments [69]. The electric field amplitudes are in a range of $1.4 \cdot 10^9$ V/m up to $2.8 \cdot 10^9$ V/m and the corresponding fluences $F = \sqrt{\frac{\pi}{8}} c \epsilon_0 \tau E_0^2$ lie in a range of 3 mJ/cm^2 to 13 mJ/cm^2 and sometimes even higher fluences were used. The range of applied fluences includes also very high fluences beyond the scope of most experiments. However, in small model systems with a finite number of sites a different energy absorption is expected than in large model system or in experiment, due to the limited number of discrete energy levels in the small systems in comparison to an (approximately) continuous energy spectrum in larger ones [93]. Therefore in comparison with experiments it is more convenient to measure the degree of excitation in terms of the number of excited electrons.

As a default linearly polarized light is used with the corresponding electric field at an angle of 30° towards the z -axis. This setting was chosen to avoid any loss of generality because it includes components parallel as well as orthogonal to the interface and the magnetization, respectively. The influence of various polarizations will be discussed in detail in Section 4.2.6.

In realistic samples with layer thicknesses of several tens of nm the intensity of the laser is decreased due to absorption in previous layers. In the following simulations nevertheless a constant laser intensity throughout the entire system is applied. The influence of a declining laser intensity and arising additional effects are presented in detail in Section 4.4.1.

The Lindblad parameters as defined in (3.61) are set to approximately reproduce experimental relaxation times. The chosen relaxation rates of $\gamma_{\text{sc}} = 2 \cdot 10^{-4} \text{ fs}^{-1}$, $\gamma_{\text{sf}} = 2 \cdot 10^{-6} \text{ fs}^{-1}$ and $\gamma_{\text{dp}} = 5 \cdot 10^{-2} \text{ fs}^{-1}$ correspond to timescales of 5 ps, 500 ps and 20 fs for spin conserving transitions, spin-flip transitions and dephasing, respectively. The ambient temperature is set to 300 K in all simulations.

To perform the time propagation (3.63) different Runge-Kutta methods are implemented. Mostly the Bogacki-Shampine method is used [94]. This is an adaptive solver of order 3 with flexible time-steps. The local truncation error is estimated with a second order method. In this way both the laser excitation with fast oscillating occupation number as well as the following relaxation can be modeled efficiently with an appropriate step width.

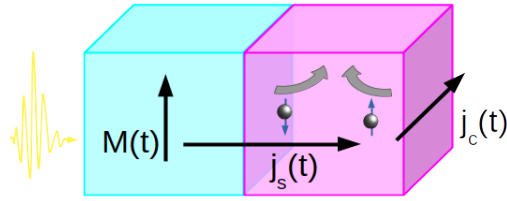


Figure 4.1.: Outline of an ultrafast demagnetization experiment at an FM|NM interface. FM material in cyan and NM material in magenta.

4.2. Ferromagnetic/nonmagnetic heterostructures

The first experiments on ultrafast demagnetization were realized in ferromagnetic bulk systems such as nickel or cobalt. Soon the bulk ferromagnets were complemented by another highly investigated material class: systems containing ferromagnetic/nonmagnetic (FM|NM) interfaces. Such an interface triggers new additional phenomena that are as well interesting for potential device applications as also useful to exert different measurement techniques.

The first experiments on heterogeneous systems did not use FM|NM systems but instead differently aligned ferromagnetic materials separated by a spacer [95]–[97]. The intention was to enhance demagnetization by enabling a flow of angular momentum between layers with an antiparallel alignment of magnetization in contrast to a parallel one. In a similar way demagnetization can be enhanced by an adjacent nonmagnetic layer. In addition to local exchange of angular momentum, a superdiffusive spin transport of hot electrons within the nonmagnetic material was proposed [32] and discussed [98] as an important contribution to demagnetization. Angular momentum is carried away from the ferromagnet by an ultrafast generated spin current. The generation of this spin current is already interesting on its own. Firstly the details of its generation process are still to be comprehended thoroughly. Secondly this mechanism can be utilized to deliberately generate spin currents by laser irradiation, to trigger further spintronic phenomena. For example when reaching the backside of the NM layer, the spin current can exert a spin-orbit torque on an additional ferromagnetic layer. In this way it can be used to rotate the magnetization of the adjacent layer. This mechanism can be utilized for magnon generation within an adjacent layer [7].

While the spin current traverses the nonmagnetic layer, a charge current is generated via the inverse spin Hall effect. As shown in Figure 4.1, the charge current is transversal to both, the directions of the spin current and spins. The inverse spin Hall effect depends crucially on the strength of spin-orbit coupling. Therefore usually $3d$ heavy metal materials are used as nonmagnetic layer. The generated charge current builds up and subsides again together with the spin current on an ultrafast timescale. It induces an oscillating electric dipole which emits radiation with a frequency determined by the built up and subsiding timescales of the spin current. Its frequency

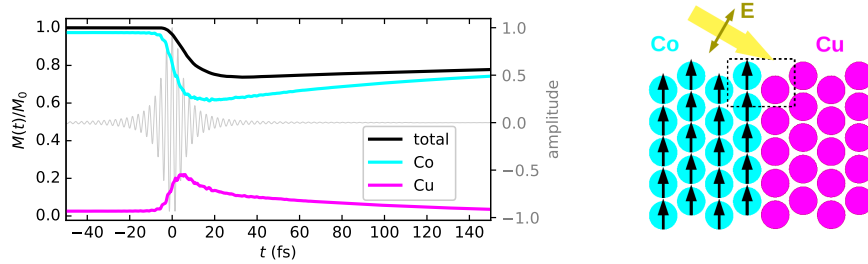


Figure 4.2.: The evolution of normalized magnetization in a two-dimensional CoCu cluster is shown on the left. The result for the entire sample (black) is decomposed into contributions from the Co region (cyan) and Cu region (magenta), respectively. The laser pulse is indicated as a thin grey line in arbitrary units. A schematic outline of the system geometry is shown on the right-hand side.

usually is in the range of several terahertz. This is exactly the so-called terahertz gap. Therefore ferromagnetic nonmagnetic interface system attract attention as possible terahertz sources for diverse applications [11], [12].

Due to the ultrafast timescale, the charge current is hard to measure electrically. Instead the emitted THz radiation can be detected electro-optically. As a result of the ultrafast demagnetization also the FM layer emits a magnetic dipole radiation. The resulting terahertz signal is however one order of magnitude smaller than that emitted by the NM layer [8], [10].

The FM|NM setup allows to access the dynamics of the spin current in the NM and corresponding demagnetization in the FM layer experimentally [9]. The crucial point is the generation of the spin current at the interface. Understanding the mechanisms its generation allows to predict and tune the emitted frequency. This enables to design interfaces made of optimized material combinations, that will yield an amplified and broadened THz radiation [11], [12].

Summarizing, ultrafast dynamics in ferromagnetic/nonmagnetic interface systems are as well interesting for potential applications and also exhibit interesting mechanisms yet to be fully understood. This makes them a worthwhile object for theoretical investigation.

4.2.1. Excitation within CoCu

The results presented in the following two sections are published in [23].

As a first FM|NM model system we study a two-dimensional cluster of Co and Cu atoms. Both layers contain 4×5 atoms forming a magnetic/nonmagnetic (100) interface. Periodicity is applied along the lattice vectors parallel to the interface. The magnetization is aligned along z -direction. This is also parallel to the interface. We assume a uniform fcc lattice for both atomic species. Cobalt usually crystallizes in an hcp lattice. But for a thin Co layer on a Cu substrate the fcc structure chosen for the

simulation is experimentally verified [89]. The time evolution of in total 40 atoms is simulated under the influence of ultrashort laser excitation. The details of the laser excitation and the Lindblad parameters are defined as introduced in Section 4.1. A sketch of the model geometry is presented in Figure 4.2.

At first the time evolution of magnetization under excitation shall be investigated. Within the basis of atomic orbitals the magnetization is defined as the difference of occupation in spin-up orbitals versus occupation in spin-down orbitals normalized to the total number of electrons,

$$M(t) = \frac{N^\uparrow(t) - N^\downarrow(t)}{N^\uparrow(t) + N^\downarrow(t)}. \quad (4.2)$$

The magnetization of the Co or the Cu layer is defined similarly but with the corresponding occupation constrained to just Co or Cu orbitals, respectively.

$$M_x(t) = \frac{N_x^\uparrow(t) - N_x^\downarrow(t)}{N_x^\uparrow(t) + N_x^\downarrow(t)}, \quad x = \text{Co, Cu, tot...} . \quad (4.3)$$

The time evolution of these observables is depicted in Figure 4.2. The magnetization of the individual layers and the total system are all presented in relation to the initial magnetization of the total system $M_0 = M_{\text{tot}}(t=0)$. With the rise of the laser intensity the magnetization of the Co layer starts to decrease down to a minimum of almost 60% at 20 fs after the pulse peak. The demagnetization of the total system follows with a delay of 5 to 10 fs. Its magnetization drops down to around 70% of its initial value 33 fs after the pulse peak. Within the initially almost nonmagnetic Cu layer an increase of magnetization is observed. It reaches its maximum already during the laser pulse 6 fs after peak time. Combined with the delayed demagnetization of the total system this observation already answers the controversy of demagnetization by spin flip versus spin transfer in CoCu. In agreement with experimental results we find that in CoCu spin transport is the dominant contribution to demagnetization [16], [92]. The fast transfer of angular momentum from Co to Cu is indicated by the simultaneous fast decline of magnetization in the Co layer and enhancement of magnetization in the Cu layer. Within this process the global magnetization is not reduced but the magnetic moments are redistributed. The spin flip processes reduce the global magnetization and happen on a slightly longer timescale. Majority spins are converted to minority spins via spin-orbit coupling and the accumulated magnetization in Cu is decreased.

Next the time evolution within the occupation of the system's eigenstates shall be investigated. Figure 4.3 shows snapshots of the discrete distribution based on the eigenstates of the equilibrium Hamiltonian H_0 at four different times: 50 fs prior to the pulse peak at equilibrium, exactly at the pulse peak and at 10 fs and 100 fs after the pulse peak in Panels a,b,c and d. Long before the laser pulse the eigenstate occupation reproduces a room temperature Fermi-Dirac distribution at 300 K.

Under the pulse peak the distribution is strikingly perturbed and differs significantly from a thermal distribution. As expected the occupation is decreased at

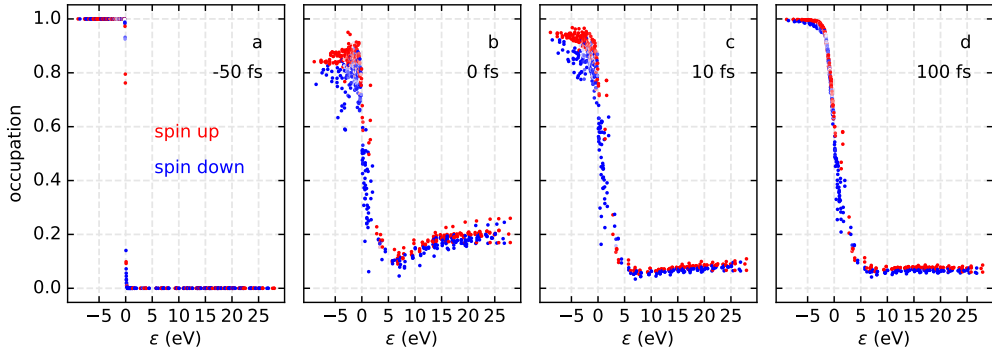


Figure 4.3.: Energy- and spin-resolved mean occupation numbers of eigenstates of the Hamiltonian \hat{H}_0 . The spinpolarization of each eigenstate with respect to the z -axis is represented on a color scale from red (majority spin) to blue (minority spin). Results are shown for times $t = -50$ fs (a), 0 fs (b), 10 fs (c), and 100 fs (d), respectively. The chemical potential is 0 eV.

states below and increased at states above the Fermi energy. The distribution is highly unthermal with a striking amount of occupation in very high-energy states. This phenomenon can be assigned to the discrete nature of the systems' energy spectrum. Since just a limited number of states is available in vicinity to the Fermi energy, the energy delivered by the laser irradiation is distributed to higher energy states. In addition to that, two kinks are visible at about -3 eV and at 0 eV.

Already at 10 fs after the pulse peak the electronic distribution starts to thermalize. Less high-energy states are occupied, but the remarkable structure around the Fermi energy is still visible. The origin of this structure will be discussed in detail in the following section. For now it shall just be pointed towards the prevalence of eigenstates with minority spin character within this structure.

At 100 fs the outstanding kinks have vanished and the distribution has adapted to a high temperature Fermi-Dirac distribution. The electronic system has thermalized. Nevertheless in comparison with a Fermi-Dirac distribution there are still too many excited states at the high-energy tail. A Fermi-Dirac distribution fitted to the almost thermalized distribution belongs to an unphysically high temperature.

Figure 4.3 proves that the electronic temperature is not well defined during the first hundreds of femtoseconds of optical excitation. Therefore a comparison of the perturbedly occupied eigenstates with a Fermi-Dirac distribution is not the best way to estimate the magnitude of the laser excitation and also the three-temperature model is highly questionable throughout this time span. Other approaches to quantify the extent of laser excitation were presented in Section 2.3.2. The number of excited electrons as defined in (2.75) was also applied experimentally by Rhie et al. [69] by evaluating the photoemission intensity above E_F . They found a number of up to 0.5 excited electrons per atom which is within the same order of magnitude as our result

of up to 1.2 excited electrons per atom. In the presented simulation we admittedly applied a rather strong laser excitation causing a strong demagnetization of 60%, but the amount of excited electrons seems still realistic.

4.2.2. Minority spin backflow across the interface

Different explanatory approaches concerning the origin of the spin current at the interface will be discussed in this section. The first explanation concentrates on the excitation of majority carriers by the laser pulse. This approach is mostly used in the context of superdiffusive spin transport [7], [30], [32], [33]. Therein the demagnetization of the ferromagnetic layer is explained by the spin- and energy-dependent velocity and transmittance of the ferromagnetic/nonmagnetic interface. This transmittance is high just for high-energy majority carriers. It is argued that, for this reason, mainly the excited majority carriers can traverse the interface and form a spin current propagating through the nonmagnetic layer. In the same way the difference of spin- and energy-dependent carrier velocities within the nonmagnetic layer is used to substantiate the primacy of the majority carriers. While the minority carriers' velocity stays low over a broad energy range, the majority carriers exhibit up to a five times higher velocity. Because of these reasons, the theory of superdiffusive spin current proclaims the high-energy majority carriers to be the main constituent of the ultrafast spin current, whereas the contribution of minority carriers is supposed to be almost negligible. The contribution of vacancies below the Fermi energy created by the excitation of electrons, namely holes, is not taken into account at all. They are assumed too slow and therefore of no significance.

Indeed the dynamics of holes and refilling of vacancies is of increased importance if the reoccupation between neighboring interface atoms of different species is considered. This kind of redistribution of occupation is for example described by the mechanism of optically induced inter-site spin transfer (OISTR; Ref. [22]). Firstly applied to antiferromagnetic materials it was shown that the laser pulse triggers a transfer of magnetic moments between neighboring sites of antiparallel spin. A possible result is the reversal of magnetic moments in one of the antiferromagnetic layers. This mechanism happens on an even shorter timescale than the ultrafast demagnetization in ferromagnetic bulk materials. The same intersite transfer mechanism could be demonstrated by Hofherr et al. in ferromagnetic alloys [99]. Also ferromagnetic/nonmagnetic interfaces and alloys were investigated. Chen et al. [92] analyzed a CoCu interface, just like presented within this work, while Willems et al. [100] and Borchert et al. [101] used Pt as a nonmagnetic material in combination with Fe, Co or Ni. All these experimental works identify a transfer of minority carriers from the nonmagnetic layer back across the interface into the magnetic layer as a relevant mechanism.

Our simulations establish a similar mechanism and are in agreement with the experimental results. We likewise observe a reflow from the nonmagnetic Cu d orbitals into empty Co minority-spin d orbitals across the interface. Hints towards an importance of this minority backflow mechanism within our results shall be presented in

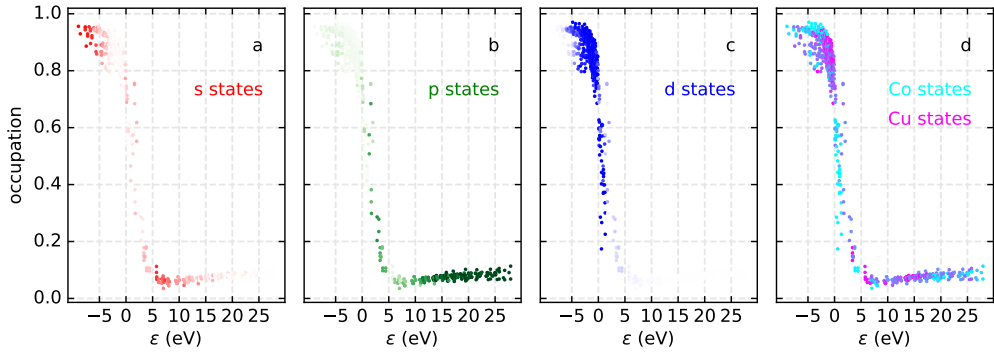


Figure 4.4.: Results of Figure 4.3 Panel c resolved with respect to orbital in Panels a – c: s (red), p (green), and d (blue); and with respect to localization in Panel d: Cu sites (magenta) and Co sites (cyan).

the following.

On this account, we analyze the excited occupation of the system eigenstates presented in the previous section in Figure 4.3. We focus on the distribution of the excited electronic system at 10 fs after the pulse peak (Panel c). It shows a prominent structure within the distribution of minority electrons. To identify the origin of this structure in Figure 4.4 the results are analyzed further by projecting the eigenstates onto the involved orbitals. Eigenstates with s and p character are spread over a broad energy range, with former ones being more centered at low energies and the latter ones more at the very high-energy tail. In contrast, the eigenstates with d orbital character are located within a narrow energy window around and below the Fermi energy. While s and p eigenstates follow approximately a high temperature Fermi-Dirac-distribution the d eigenstates are highly nonthermal by forming the two kinks described before. The projection with respect to the atomic species, Co or Cu, identifies the eigenstates related to the first kink at about -3eV as Cu states and the eigenstates related to the second kink at E_F as Co states. This insight complies with the shape of the corresponding electronic band structures. Within the Cu band structure there are just s bands at the Fermi energy and d bands are at about 3 eV below, whereas in Co the Fermi energy is located right in the middle of the d bands. The Cu d states are completely occupied whereas the Co d states are just partially filled with many empty states available. Therefore also in our simulation a strong depletion of the minority Cu d states can be observed while occupation within the minority Co d states is increased. The reduction of Cu d^\downarrow occupation and the enhancement of Co d^\downarrow occupation hints at a transfer of d^\downarrow electrons from Cu to Co.

These results can also be extracted by studying the time evolution within the local basis set. On this account, we switch from the 2D supercell to a 1D supercell as depicted in Figure 4.5. The new supercell in form of a chain consists of 10 Co and 30 Cu atoms with periodicity parallel to the interface. Both setups resemble a thin fcc Co layer on a Cu substrate with a (100) interface. The elongated geometry facilitates

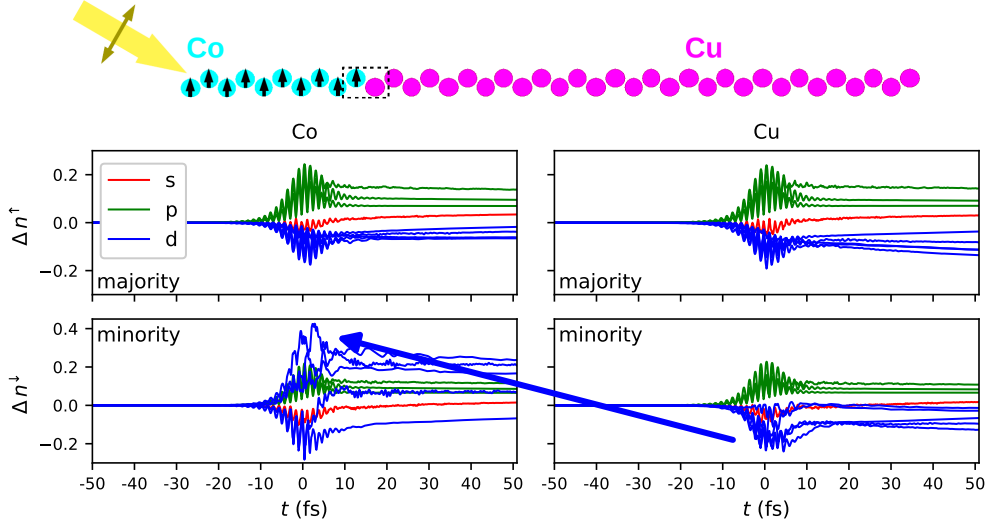


Figure 4.5.: Changes Δn of occupation numbers at a Co (left) and Cu (right) site at the interface. The changes are resolved with respect to spin and orbital angular momentum (s , p , and d : red, green, and blue, respectively). The blue arrow indicates the ‘backflow’ associated with minority-spin d orbitals across the interface (see text). On top the simulated chain with the analyzed sites is sketched.

the analysis of transfer as well as currents passing through the nonmagnetic layer due to the larger extent of the system orthogonal to the interface. All other settings are unchanged.

In Figure 4.5 the change of occupation is shown for two neighboring interface atoms in orbital resolution and for majority and minority occupation separately. A common behavior for majority and minority orbitals as well in Co as in Cu is a depletion of d orbitals and a population of p orbitals, shown in blue and green respectively. The main process and direct influence of the laser pulse is a dipole transition of d electrons into higher-energy p states. The transition from d to p orbitals is further substantiated by similar slopes with opposite sign of both occupation numbers. In contrast the occupation of s orbitals, shown in red, is modified just slightly and with a short time delay. With s orbitals initially not fully occupied and almost empty p orbitals an excitation between s and p orbitals is less probable in the beginning. In comparison between all panels a significant difference can be observed in the time evolution of Co minority occupation. Therein, instead of a depletion an enhancement of d orbital occupation takes place. As pointed out before, this can be ascribed to a transfer of occupation from minority Cu d orbitals to minority Co d orbitals as indicated by the blue arrow between the corresponding panels. An exception are the d_{yz} orbitals. They are not involved in this transfer process because they have minimal overlap in x -direction across the interface. Therefore also a loss of occupation can be

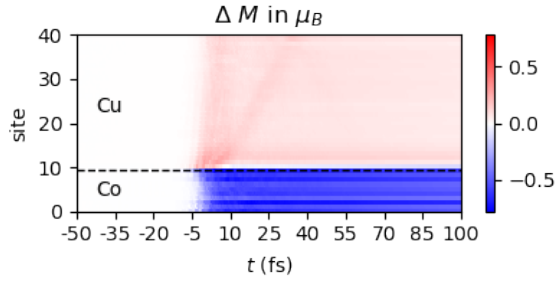


Figure 4.6.: Temporal change of magnetization in spatial resolution. The magnetization of each site is shown in relation to its equilibrium magnetization at $t = -50$ fs. The y -axis represents the extent of the chain.

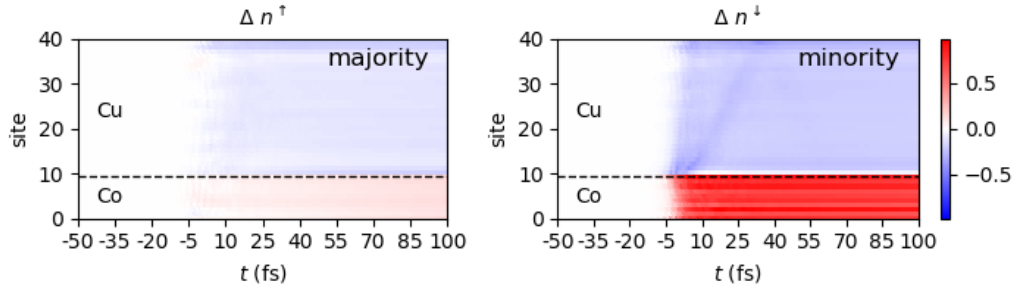


Figure 4.7.: Change of majority and minority occupation along the CoCu chain.

observed in Co minority d_{yz} orbitals.

The larger longitudinal extent of the chain system yields visualization of the propagation of occupation and magnetization throughout the system. Figure 4.6 illustrates the temporal change of magnetization $\Delta M(t, R) = M(t, R) - M_0(R)$ along the chain. While a considerable demagnetization takes place in the Co area, the Cu atoms acquire additional magnetization. Furthermore this dynamics is at first and most distinctly visible at the interface atoms. Only afterwards with a delay of a few femtoseconds it propagates further through the corresponding layer. That is to say, the additional magnetization gained by the Cu interface atoms spreads through the Cu layer and equally the loss of magnetization travels through the Co layer. With the propagation velocity determined by the hopping constants the transferred spin momentum reaches the end of the chains after not more than 5 fs.

These transfer processes can be analyzed furthermore by studying the loss and gain of occupation at each site in spin and orbital resolution. This is realized in Figure 4.7. The changes of majority occupation are much weaker than the changes of minority occupation. But in both cases occupation is lost in the Cu layer and redistributed to the Co layer. While this is just faintly visible in case of majority orbitals, the contrary is the case regarding the change of minority occupation. A distinct gain of occupation can be observed within the Co minority orbitals while

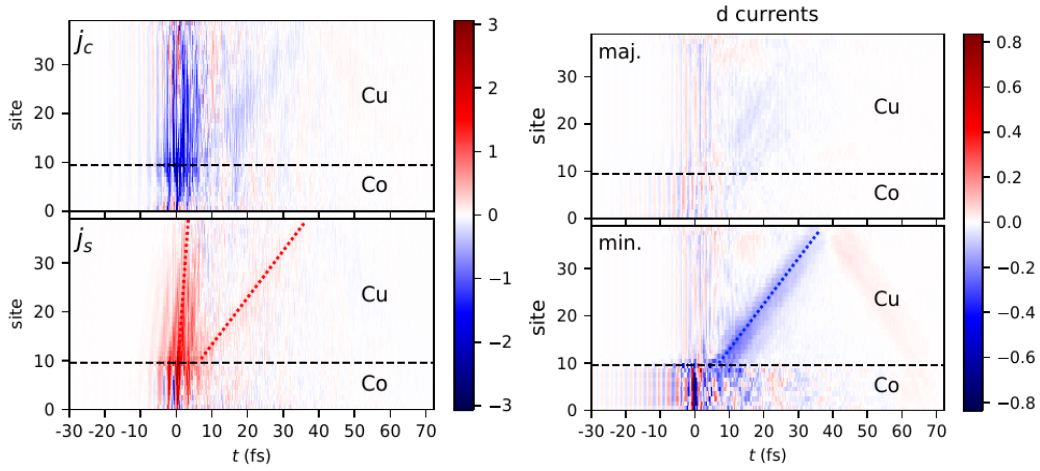


Figure 4.8.: Currents along the extent of the chain (y -axis). Left panel: charge and spin currents. Right panel: currents between majority d orbitals or minority d orbitals only. Note the different color scales in arbitrary units, which also indicates the transport direction towards the upper Cu edge (red) or the lower Co edge (blue) of the sample. The colored dashed lines facilitate an estimation of velocities.

the Cu minority orbitals are depopulated. Just like the previous observations, this disparity within the sample hints to a transfer mechanism between the Co and the Cu layer.

Finally it has to be mentioned, that within a many-body calculation, and also in physical reality, the observed charge accumulation would not persist for such a long time. On the contrary, due to electrostatic repulsion between the electrons an additional redistribution would be observed, which homogenizes any charge accumulation. However, within our effective single-particle-density matrix approach this effect is not yet reproduced.

Currents

Figure 4.8 presents the calculated charge currents and spin currents as well as majority and minority currents within the d orbitals of the CoCu chain. Since the discussed model system is collinear with the spin quantization axis along the z -direction the currents can be calculated according to the definition (3.73) and (3.77). In case of the d currents this summation is restricted to just d orbitals. Both, the charge as well as the spin current are presented in the following without the prefactors shown in the definitions, the site distance and e or $\frac{\hbar}{2}$, respectively. By omitting these factors the currents show the sum or the difference of spin-up and spin-down particle currents. In 2D plots with color maps the results were multiplied by a factor of 100.

For all plots of currents holds: red color represents currents moving along the x -

axis from the FM layer towards the NM layer, whereas areas of blue color reversely represent currents moving from the NM layer back to the FM layer. In Figure 4.8 the left panel shows clear signals from charge and spin currents flowing in opposite directions. While the charge current flows from Cu into Co, a spin current flows from Co into the Cu layer. Both consist of a fast and a slower contribution and are initiated at and centered around the interface. From there both currents expand covering almost the entire sample. This expansion happens at a high velocity of more than 0.9 nm/fs, as indicated by the left dashed red line.

In both cases disturbance at the edges and oscillations occur. Most pronounced such oscillations are visible in s currents shown in Figure 4.15 as alternating blue and red stripes which are evenly distributed throughout the whole chain. The oscillations can be ascribed to components of the electric field of the laser light parallel to the chain direction. These are triggering a motion of electronic charge together with the electromagnetic oscillations. After the laser pulse is gone also the oscillating charge currents rapidly subside.

The currents between d orbitals, shown in the right of Figure 4.8, likewise exhibit some small oscillations during the laser excitation and also some weak dynamics at the interface and the chain edges. However, in the minority d orbitals the propagation from the Cu layer to the Co layer is strongly pronounced and dominates the dynamics. Especially within the Cu layer the currents between minority d orbitals exhibit a distinct structure that reveals a backflow from Cu into Co and is visible as a broad blue stripe. This corroborates the backflow of minority occupation deduced from Figure 4.4. Starting at the interface initially only minority d orbitals of the first Cu atoms are depleted and then refilled by minority d electrons of subsequent Cu atoms creating a current pointing in $-x$ -direction back to the Co layer. In this manner the minority d current propagates through the Cu layer eventually being reflected at the sample edge and finally attenuated and quenched due to dephasing. This reversely also happens within the Co layer where the minority d occupation provided by the Cu layer spreads from the interface to the sample edge. The currents in the Co regions are strongly modulated due to reflection of electrons at the sample's Co edge and at the interface.

The current of minority d electrons flowing from Cu to Co contributes to the spin current in the reverse direction. It is the slow component of the spin current visible in the left panel of Figure 4.8 and indicated by the second dashed red line. With an estimated velocity of 0.26 nm/fs this minority d current is relatively slow compared to the rest of the spin current, as illustrated by the different slopes of the lines. The calculated velocities associated with the ballistic currents in the Cu region agree with energy-dependent velocities calculated for gold and iron (nickel) [30], [102].

By this analysis we distinguished two induced currents within the sample: a flow of hot, highly mobile s and p electrons complemented by a reflow of 'tepid', weakly mobile d electrons. In the presented model system the backflow of minority d electrons seems comparably weak with respect to faster processes. Both contributions will be quantified in Figure 4.24.

Origin of the spin current

The interface can clearly be identified as the source of the spin current, which strongly reinforces the demagnetization in the magnetic layer. But what triggers the transfer mechanism across the interface? In case of diffusive transport particles move along a gradient. In the presented model a conventional global gradient can not be identified. Within this model it is more appropriate to speak instead of local imbalances. Before excitation with the laser the interface occupation reaches an equilibrium situation. Then the laser pulse excites Co and Cu atoms in a different way and thus causes a local imbalance of occupation at the interface atoms. An interface may therefore be regarded as an additional source of nonequilibrium.

Another origin of local imbalances is for example the excitation at a sample edge. Also in this case the local inhomogeneity of occupation at the edge atoms leads to different excitations and can trigger a transfer mechanism. In fact this also happens within the studied model systems but the local imbalances created at the edge are small compared to those at the interface.

Furthermore a gradient within the laser intensity or a gradient of an external magnetic field can cause such transfer mechanisms. This will be discussed in Chapter 4.4.1. However, in case of the presented chain system the same laser intensity was chosen for each atom and no external magnetic field was considered. Therefore none of these effects is present in this simulation.

4.2.3. Quantum state measures

In this section the Quantum state measures, as introduced in Section 2.3.2, will be discussed using the example of an optical excited chain of 10 Co and 30 Cu atoms. Similar results are presented in publication [103].

Figure 4.9 presents all introduced measures together with an outline of the temporal evolution of the electric field of the laser pulse in Panel d. The depiction focuses mainly on the perturbation of the measures under the laser pulse. At longer timescales, not shown here, the system relaxes back to its initial state by interaction with the heat bath and also the QSMs will return back to their initial value.

Panel a in Figure 4.9 shows the number of excited electrons per atom, starting at 0, oscillating under the pulse, then settling at a level of 1.0 before slowly declining towards 0 on longer timescales. The number of excited electrons was used to coarsely adjust the degree of excitation of simulation and experiment ([69]) by varying the applied electric field amplitude.

The distance measures, fidelity in Panel f and trace distance in Panel e, as well as the number of excited electrons exhibit strong oscillations with twice the frequency of the laser pulse. After the laser excitation they settle on a lower value of perturbation and relax back to their initial values afterwards. The redoubled oscillation frequency can be explained by Fermi's golden rule, which states that the transition rate is proportional to the square of the perturbation matrix element. The matrix element (2.35) contains the time dependence, which under the square transforms as

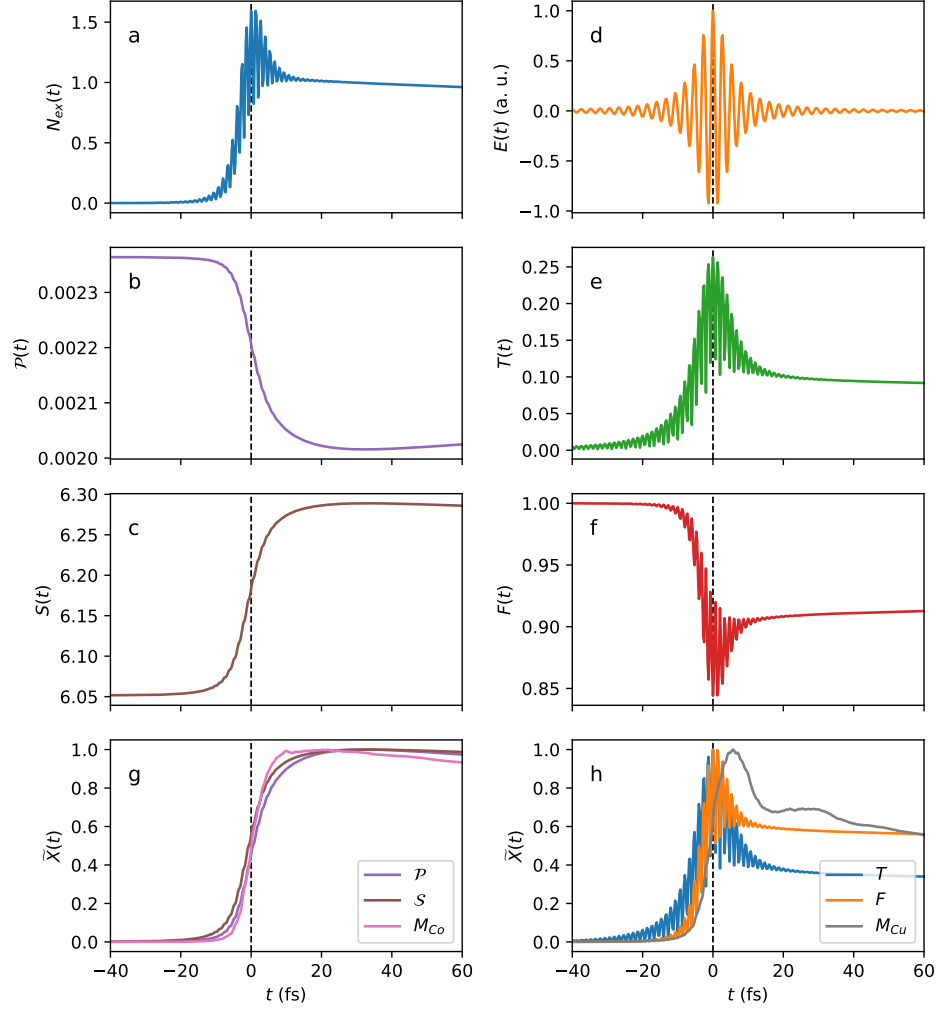


Figure 4.9.: Quantum state measures of a CoCu chain excited by the electric field of a laser pulse (d): number of excited electrons (a), purity (b), von Neumann entropy (c), trace distance (e), fidelity (f) and a comparison of QSMs with the temporal evolution of magnetization in terms of rescaled values $\tilde{X}(t) = |X(t) - X_0| / (\max(|X(t) - X_0|))$ (g, h).

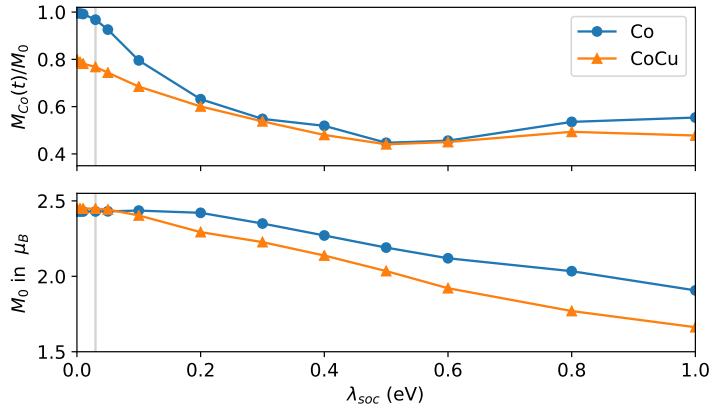


Figure 4.10.: Dependence of initial magnetization (bottom) and demagnetization (top) on the SOC parameter of the d orbitals in a Co and a CoCu chain. The SOC parameter that is used for Co in other calculations is indicated as a grey line. In the CoCu chain, the SOC parameter is set to the same value in both materials.

$|\cos(\omega t)|^2 = \frac{1}{2}[1 + \cos(2\omega t)]$. Therefore the transition probability between initial and final state does not depend on the sign of the electric field. It is largest at the electric field's minimal and maximal values. The electrical dipole matrix elements induce excitation as well as de-excitation, depending on the occupation of participating orbitals. Nevertheless both are not reciprocal, because especially in inhomogeneous samples occupation propagates to neighboring sites.

The purity measures, purity in Panel b and von Neumann entropy in Panel c, exhibit a smooth course from their initial value to the value of excitation, with only very slight oscillations together with the laser pulse.

Finally, Panels g and h compare the time evolution of QSMs with the simulated magnetization in terms of rescaled values. Panel g shows that the purity measures \mathcal{P} and \mathcal{S} exhibit a time evolution very similar to that of M_{Co} . While the time evolution of the distance measures \mathcal{T} and \mathcal{F} shows a similar behavior as M_{Cu} .

In that sense the perturbation of the density matrix can be linked to observables. In the present work QSM are used to identify setups that yield large perturbations. While in quantum information theory, their usual area of application, QSMs are used to identify least possible perturbed setups.

4.2.4. Influence of spin-orbit coupling

To pinpoint the origins of demagnetization it is necessary to tune various parameters. As a coupling between spin and orbital momentum spin-orbit coupling (SOC) is the most promising candidate to affect demagnetization. The influence of SOC on demagnetization is tested by varying SOC parameters in a ferromagnetic system and

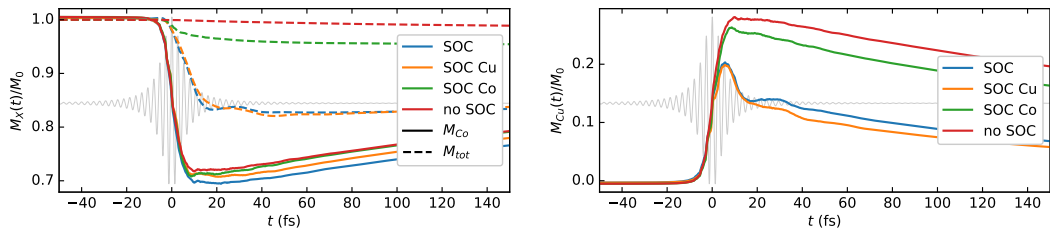


Figure 4.11.: Magnetization dynamics in a CoCu chain calculated with SOC (blue), without SOC (red), with SOC just at Cu atoms (orange) or just at Co atoms (green). Left: demagnetization of the Co layer (full lines) and the total system (dashed lines). Right: Enhancement of magnetization in the Cu layer.

a FM|NM system. These are a chain of 20 Co atoms and a chain of 10 Co and 10 Cu atoms, both with open boundaries in direction of the chain and periodic boundaries otherwise. For this investigation the parameter λ_{soc} is also set up to high values beyond the regime of realistic material parameters considered in this work (cf. 4.23).

Figure 4.10 shows the decrease of initial magnetization M_0 with increasing SOC. The influence of SOC is stronger in CoCu but in both systems almost negligible for small SOC parameters below 0.1 eV, the regime of SOC values of Co or Cu.

As expected in both systems the demagnetization increases with increasing SOC up to almost 40 %. At higher parameter values the demagnetization saturates. Differences between the ferromagnetic system and the bilayer system manifest in the regime of realistic parameters. At $\lambda_{soc} = 0.03$ eV, the material parameter of cobalt, the ferromagnetic setup demagnetizes only by a few percent while the bilayer demagnetizes by more than 20 %. At zero SOC the demagnetization vanishes in the ferromagnetic system. In contrast, in the bilayer system there is a minimal demagnetization of about 20 % even without SOC.

These tests show that in our model the demagnetization of a ferromagnetic system is generated by SOC and can be manipulated by SOC over a broad range (0 - 40 %). This holds also for the demagnetization of the magnetic layer in FM|NM systems, but here the contribution of spin transfer to demagnetization is dominant in the regime of small SOC parameters. This conclusion should similarly hold for antiferromagnetic systems, bilayer or multilayer systems as well as for alloys; for any system in which a transfer of angular momentum can take place between neighboring sites of differing spin polarization. To prove the minor influence of SOC in such systems the simulations of the previous section were repeated without considering SOC. The results thereof are presented in Figure 4.11. It shows the same results as Figure 4.2 but in comparison to calculations with the SOC parameter set to zero for either just Co atoms, just Cu atoms or for both. Again the results of the total system are decomposed into contributions of Co and Cu layer, respectively.

The demagnetizations of the Co layer, shown as full lines in the left panel, coincide

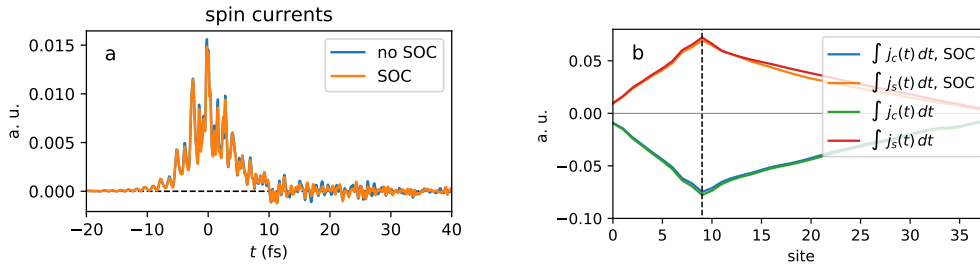


Figure 4.12.: Dependence of interface currents on spin-orbit coupling. Panel a shows the spin currents between the interface atoms of Co and Cu. Panel b shows for each bond along the chain, represented by the x -axis, the transferred charge and spin, respectively.

during the beginning of excitation. Only at about 5 fs after the pulse peak the demagnetization in Co without SOC reaches a level of saturation. If SOC is taken into account the demagnetization continues longer and reaches a lower minimum. These findings are similar to TDDFT calculations presented in Fig. 3 of [92]. The results with SOC in only one of both materials lay in between the other ones and exhibit the same characteristic features. The steep decrease in magnetization at the ultrashort timescale and directly after the laser excitation is however not affected by SOC. This very strong and fast demagnetization is therefore an interface-generated transfer mechanism.

In contrast, the demagnetizations in the total system behave very differently. Without SOC the conservation of angular momentum is only broken by the spin-flip scattering rate γ_{sf} . This results in dynamics on a timescale of several hundred ps and is visible on the presented timescale of 200 fs only as a very slight decrease of the total magnetization, shown as a red dashed line. If this effect is accompanied by SOC, the demagnetization of the total system happens on a timescale of about 10 fs, shown as the blue dashed line.

The steep drop of Co magnetization is mirrored by the steep increase of Cu magnetization, presented in the right of Figure 4.11. In Cu the enhancement of magnetization is largest without any SOC, followed by the setup with SOC only within the Co layer. Simulations with SOC in Cu and SOC in both layers are almost identical and exhibit a lower enhancement together with a stronger subsequent decline of magnetization. In both cases fast enhancement of magnetization is attenuated by the SOC in Cu. It serves as an exchange channel between majority and minority occupation and leads to an equalization of both carrier species. In this way excess magnetization obtained by angular momentum transfer between Co and Cu layers is removed again.

The influence of SOC on the charge and spin currents is illustrated in Figure 4.12. Again, positive values correspond to a current flowing along the x -direction from Co

to Cu, whereas negative values correspond to a current along the opposite direction, from the Cu layer into the Co layer. Panel a shows the time dependence of the spin current between Co and Cu interface atoms. It is strongly centered around the pulse with a maximum already shortly before the pulse peak at 0 fs. This indicates a strong spin current flowing from Co to Cu which builds up and recedes together with the laser pulse.

The above observations equally hold for simulations with and without SOC. However, spin transport seems to be just very slightly weakened by SOC. It shall be emphasized that there is also no acceleration of spin current generation by considering SOC. The time evolution of the spin current in both simulations coincides.

Panel b of Figure 4.12 shows for each site individually the spin and charge currents integrated over the simulation time from -50 fs to 200 fs. Both, the transferred charge as well as the transferred spin, exhibit a similar profile throughout the sample with a maximum directly at the interface and a decrease towards the edges. As in Panel a, there are also no major differences between results for integrated currents with SOC and without SOC.

From the analysis above can be concluded that in the present interface system demagnetization in the magnetic layer and spin current injection into the nonmagnetic layer have the same origin. And this is the transfer of electrons across the interface. This holds true within the very first femtoseconds directly after the optical excitation. Only more than 5 fs after the pulse peak, other mechanisms of demagnetization continue and become dominant. This conclusion differs from the conclusion by Rouzegar et al. [104]. While in our simulation the interface is the main driver of demagnetization, Rouzegar et al. state that already in a pure FM the demagnetization has the same magnitude and temporal evolution and thus the same origin as the spin current generated in an interface system. A possible explanation for this disparity are the different regimes of excitation, with a fluence of 0.1 mJ/cm^2 and a change of electronic temperature of 160 K in the experiment compared to a fluence of 13 mJ/cm^2 in our simulation. A minimal degree of excitation to launch the transfer mechanism at the interface could explain, why a interface-generated demagnetization by spin transfer may be absent in those experiments. On the other hand such minute excitations as in the experiment may be too small to be represented adequately on the discrete energy scale of the simulation even for larger sample sizes.

4.2.5. A comparison with the OISTR mechanism

Results calculated with the EVOLVE code and with TDDFT codes, such as Elk [105], are in very good agreement with respect to timescale and degree of demagnetization if applied to heterogeneous structures, just as FM|NM interfaces [92], [101]. Both approaches are hinting to a strong contribution of a rapid transfer mechanism to the demagnetization, in which minority d electrons are transferred from the nonmagnetic to the ferromagnetic atoms. However, this agreement holds only for pulses with a temporal duration significantly longer than 1 fs. The exact details of the mechanisms implemented in both codes are fundamentally different, which manifests when

considering subfemtosecond timescales.

In `EVOLVE` the transition matrix elements induced by the laser excitation are calculated and added to the ground state Hamiltonian in form of a perturbation matrix. Whereas in TDDFT calculations, as the `Elk` code, the vector potential associated with the laser light is included directly into the system Hamiltonian. As a result not just the optical transition as a complete process is modeled but also the displacement of electron density in accordance with the electric field of the laser light is simulated. An optical perturbation of the electron density needs a specific minimal amount of time to be regarded as a completed transition process. In case of excitation times below this threshold the description of the perturbation by a transition matrix is oversimplifying if not questionable. It describes the results of the completed transition process and not its generating dynamics. The electric dipole approximation as introduced in Section 2.2.2 gives the following limitation of its applicability: the time of the excitation has to be significantly larger than the inverse frequency $\Delta t \gg 1/\omega$. That is to say, to describe the process as an excitation by a sinusoidal perturbation the electric field has to perform at least some oscillatory cycles during the time of oscillation defined by the pulse width. For shorter time intervals the sinusoidal character of the perturbative field is lost and the description in terms of transition elements is no longer applicable [43].

Additionally, in TDDFT simulations the bandstructure and eigenstates are represented in \mathbf{k} -space. Therefore local information has to be extracted by a projection. Due to the mixed atomic character of the eigenstates an optical transition in the band structure-picture does generally include more than one atomic site. If the atomic character of the corresponding eigenstates is different the excitation process can be viewed as a transition between different atoms. Yet this is not to be interpreted as a relocation process but rather as an on-site transfer between overlapping orbitals of neighboring atoms. All together the crucial point in TDDFT simulations is the start of a transfer process directly and simultaneously with the laser pulse.

Within `EVOLVE` we chose a local representation of the system states and only accounted for on-site optical excitation. Therefore, optical transition matrix elements are nonzero only if the interacting orbitals are centered at one and the same atomic site. Thus, the transfer mechanism as depicted in the previous section cannot be achieved directly by an optical excitation. The optical excitation rather introduces a local inhomogeneity within the occupation numbers which acts like a gradient and causes a transfer between the overlapping orbitals centered at neighboring atoms. In the tight-binding model this transfer is realized by the interatomic hopping. In this case the laser induced transfer does not happen simultaneously with the laser excitation but rather as a two-step process of on-site excitation and subsequent interatomic hopping. Within our `EVOLVE` approach the limiting timescale of about one femtosecond for transfer generated demagnetization is therefore determined by the hopping parameter between neighboring atoms. The transfer mechanism is initiated as soon as a perturbation of occupation numbers builds up. Therefore, it can already start and also happen during the optical excitation. For all excitation processes happening on even shorter timescales, like for example attosecond excitation, the transfer

and with it also the demagnetization process will happen mostly when the optical excitation is already over. Within EVOLVE an attosecond optical excitation would exhibit a minimal demagnetization time of about 1 fs. In contrary the demagnetization simulated by the ELK code would mostly happen during the laser pulse.

TDDFT and EVOLVE results therefore can only coincide if the pulse width is long compared to the hopping timescale. This is realized for a pulse width of at least 10 fs.

Keep in mind that the above considerations are true for transfer generated demagnetization processes. In ferromagnetic bulk materials the demagnetization times are mainly determined by the strength of spin-orbit interaction.

4.2.6. Varying laser polarization

The polarization of the applied laser light can be oriented differently with respect to the interface and the magnetization of the sample. As a result the direction of the corresponding electric field in combination with the orbital orientation does enable or forbid certain transitions and therefore allows certain components of spin polarization. If a mirror symmetry $\mathcal{M}_i : (ijk) \rightarrow (-ijk)$ is present in the system it prohibits spin polarization parallel to its mirror plane, in this case in direction j and k . Only \mathcal{S}_i is even under \mathcal{M}_i and allowed in the system. In order to optically induce a spin polarization the electric field of the laser has to break mirror symmetries of the system.

Copper exhibits the symmetries $\mathcal{M}_x, \mathcal{M}_y$ and \mathcal{M}_z . Therefore, no global spin polarization can be achieved if the electric field is aligned parallel to a Cartesian axis. In cobalt the symmetry \mathcal{M}_z is already broken by the finite magnetization M_z and in the bilayer system the symmetry is reduced further by the presence of the interface. A similar symmetry analysis is presented in [88], illustrated by EVOLVE-simulations of Cu, Co and CoCu systems, while an extended analytical analysis can be found in [51]. The above suggests a more effective excitation and demagnetization for electric field directions far away from the symmetry axes of the system. This shall be investigated in the following.

In Figure 4.13 the influence of laser polarization on the demagnetization is investigated systematically. The model system under considerations is the same as in the previous sections: a chain of 10 Co and 30 Cu atoms along the x -direction. In addition a three-dimensional cluster of 16 Co atoms and 16 Cu organized in cubic 4-atomic unit cell is investigated. By choosing this geometry an equal extent of the cluster along all Cartesian axes is ensured. In both geometries the interface normal points along the x -direction and periodic boundaries are applied along y - and z -directions. Certain variations were introduced to the original setup shown in orange. The blue line represents a system with the magnetization of the Co atoms pointing along the x -axis, orthogonal to the interface. The red graph shows results of the optical excitation calculated by the substitution introduced in Section 2.2.2. And the green graph shows demagnetization in a pure Co system. Each system is set up in the same size and geometry as the original CoCu system under consideration and each data point represent the maximal demagnetization generated by the corresponding

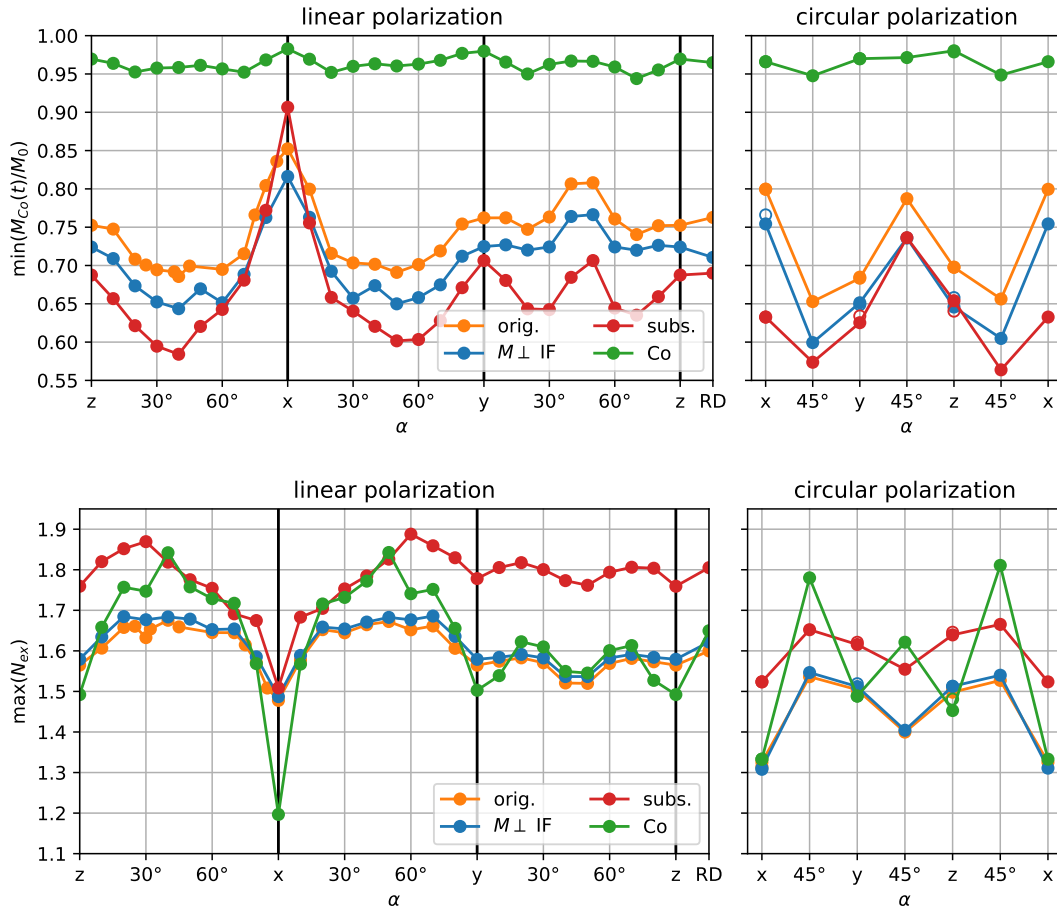


Figure 4.13.: Top: demagnetization in the Co layer of a CoCu chain excited by differently polarized light. In case of linearly polarized light (left), the x -axis shows the direction of the electric field and the angle α with respect to the prior coordinate axis on the left. RD shows the results for one of the space diagonals. Equivalently the incidence direction of the laser is indicated for circularly polarized light. In this case the electric field is orthogonal to the respective direction and empty markers represent the reversed helicity. Bottom: maximal number of excited electrons shown in the same way.

optical excitation.

Unfavorable alignments of the electric field along the symmetry directions are easily visible in Figure 4.13. They are indicated by high values of $\min(M_{Co}(t)/M_0)$ which correspond to small demagnetizations. Throughout all systems the most prominent feature is the minimum of demagnetization for electric fields along the x -axis, pointing along the interface normal. Optimal electric fields are pointing between x - and z - or x - and y -axis, with the exact optimal angle varying between the different setups. Whereas electric field directions between y - and z -axis yield a second minimum of demagnetization. This minimum can be explained by missing links in the corresponding direction in the chain system. The theory of spin polarization, as in Ref. [51], can explain a single minimum or maximum between two axes, as in case of the red and orange lines between z - and x - or x - and y -axis. However, the restricted model geometry that causes several minima or maxima as between the y - and z -axis is beyond the scope of the theory.

In most cases the circularly polarized light induces a demagnetization comparable to that of linearly polarized light with the corresponding electric field components. For example circularly polarized light incident along the x -direction corresponds to linearly polarized light with the electric field between y - and z -directions. Results for different helicities are mostly in good agreement.

The interpretation of the above results is not straightforward as the demagnetization is a consequence of many factors. First, there is the optical excitation of spin polarization, which is favored by a breaking of symmetries. But on the other hand demagnetization is also facilitated by transfer of angular momentum through the interface. Therefore one could assume a high demagnetization by excitation of charge currents along the electric field and through the interface. However, considering the weak demagnetization for $\mathbf{E} = E_x$, the opposite seems to be true.

The main features discussed regarding demagnetization can also be observed when investigating the strength of excitation in terms of $\max(N_{ex})$, the maximal number of excited electrons, in dependence on the laser polarization. This is shown in the bottom of Figure 4.13. The comparison of both quantities reveals that the characteristic maxima and minima of demagnetization result from optima and minima of optical excitation. This suggests a minor influence of the alignment of electric field with possible transfer directions and instead an influence of the restricted dimensionality in a chain system. In other words, the number of sites within the model along a specific direction seems to influence the degree of excitation by an electric field along the same direction. Thus the choice of a specific geometry influences the polarization dependence in our simulations.

To exclude the model-induced dependencies as much as possible, the simulations were repeated with the symmetric 3D cluster in Figure 4.14. Indeed the pronounced structure of the polarization dependence and the protruding character of the electric field $\mathbf{E} = E_x$ have vanished. In the elongated system the demagnetization between different polarizations varied by more than 15%, while it only changes by a few percent in the symmetric 3D cluster. But still electric fields along the Cartesian axes yield less demagnetization than along most other directions.

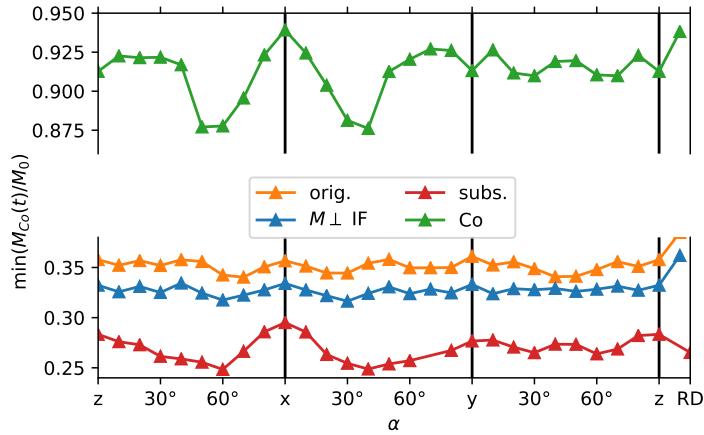


Figure 4.14.: The dependence of demagnetization on the laser polarization is shown as in Figure 4.13 for linearly polarized light, but for a three-dimensional system with a cubic unit cell.

In both geometries the setups with magnetization orthogonal to the interface are demagnetized more strongly, despite showing the same degree of excitation and despite their higher number of mirror symmetries. Without spin transfer across the interface, the pure ferromagnetic setup exhibits the least demagnetization. While the alternative excitation routine, in red, mostly shows higher excitation and demagnetization.

In principle there are two ways to change the vector of spin polarization. First, an electric field can induce spin polarization orthogonal to the magnetization of the material. For example an E-field E_{zx} induces spin polarization along the y -direction. Second, the electric field induces spin polarization parallel or antiparallel to the magnetization, as in case of E_{xy} which induces S_z . This can generate a reduction of $|\mathcal{S}|$, the length of the vector of spin polarization. In contrast, the first scenario corresponds to a tilting of the spin moment out of its equilibrium axis. But in Figure 4.13 those two different scenarios of changing the spin momentum result in almost the same demagnetization.

Figure 4.15 shows the different current dynamics resulting from electric fields along the x - or z -axis, respectively. If the electric field is parallel to the chain direction a current is induced along the chain and its sign oscillates strongly together with the frequency of the laser light. This is clearly visible in case of the s currents. After excitation with an electric field $\mathbf{E} = E_z$ no oscillation of occupation along the chain direction is induced. Accordingly very clear signals of a spin current from Co into Cu and a charge current in opposite direction can be observed. In comparison the signals of charge and spin currents under excitation with $\mathbf{E} = E_x$ are quite blurred, although the overall directions are still recognizable.

The amount of charge and spin transport along the chain is quantified in Fig-

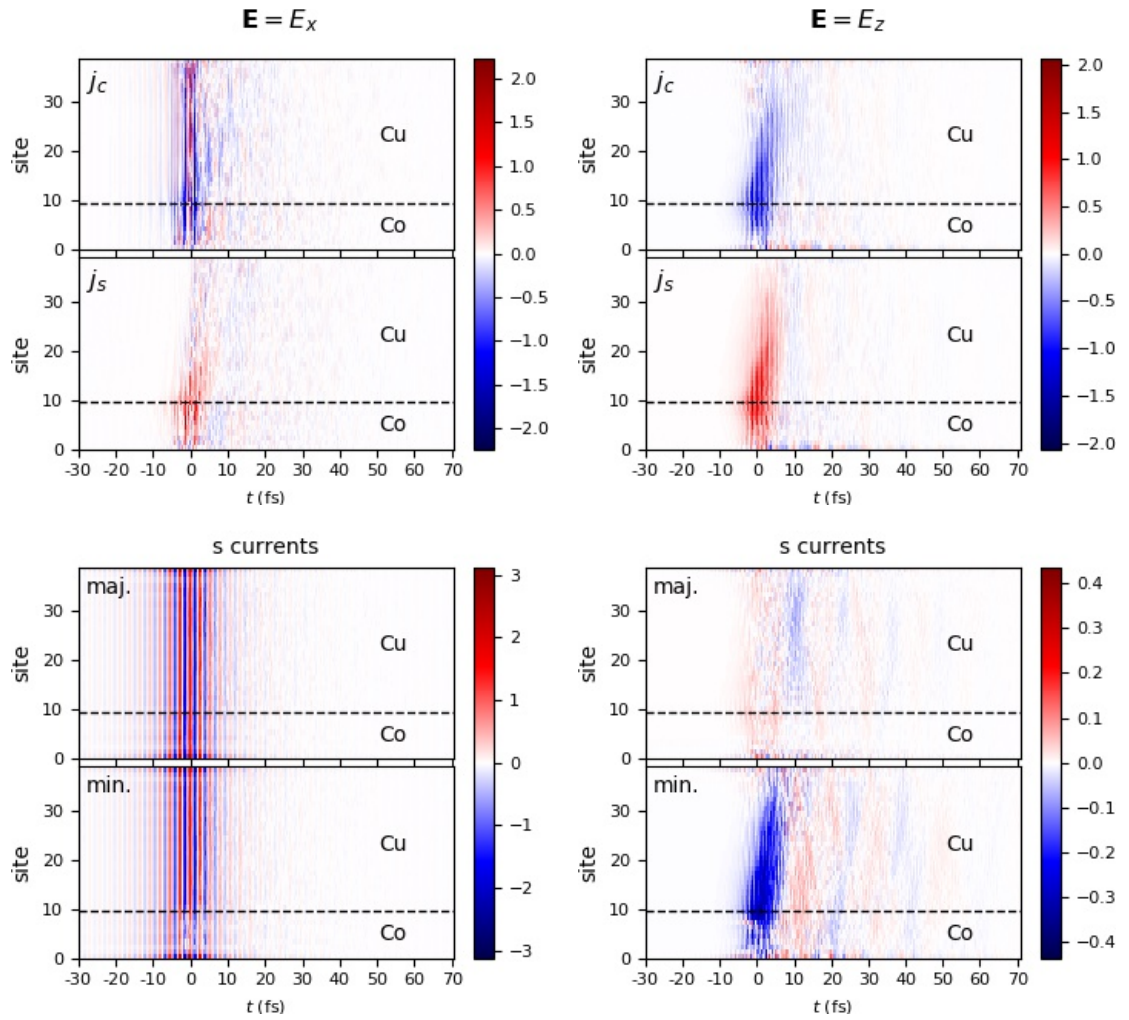


Figure 4.15.: Visualization of currents in a CoCu chain excited with differently polarized light: $\mathbf{E} = E_x$ on the left and $\mathbf{E} = E_z$ on the right. The top row shows charge and spin currents and the bottom row shows majority and minority currents between s orbitals.

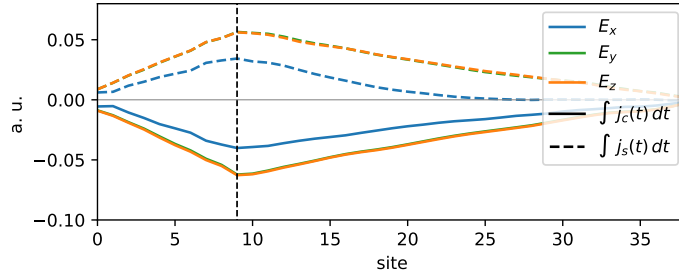


Figure 4.16.: Profile of charge and spin transport through different sites as introduced in Figure 4.12. Here results for differently polarized light are compared. The interface is indicated by the dashed line.

Figure 4.16 for electric fields along the Cartesian axes. Results for electric fields $\mathbf{E} = E_y$ and $\mathbf{E} = E_z$ are almost identical. But for $\mathbf{E} = E_x$ the transport through the interface as well as along the chain is less efficient despite strongly oscillating charge currents visible in Figure 4.15. Also, in this case the spin current into the Cu layer seems to subside quite fast, just about 10 sites away from the interface. The reduced spin transport for $\mathbf{E} = E_x$ is in good agreement with the weakened excitation and demagnetization observed in Figure 4.13.

In summary, the dependencies on polarization presented in Figures 4.13, 4.15 and 4.16 are mainly caused by the restricted geometry of the model system. In a symmetric setup (Fig. 4.14) and in experiments the degree of excitation and demagnetization is barely perturbed by changes of the laser polarization.

4.2.7. Varying photon energy

The frequency of the applied laser light does crucially determine the details of the initiated excitation process. The frequency is proportional to the photon energy (2.57) and allows for transitions between states with corresponding energy difference. By varying the frequency the excitation occurs between different regions of the band structure. Therefore one might assume that the exact frequency of the applied laser light can drastically affect the magnetization dynamics. In fact the opposite seems to be true. At least in the linear regime the demagnetization process appears to be fairly robust with respect to changes of the applied frequency. This was demonstrated for ferromagnetic/nonmagnetic layers in [106] and [107] and by Chekhov et al. with optical and terahertz pulses in a homogeneous iron layer [108]. As this variation is not just a slight but a drastic change in frequency, the resemblance of the respective demagnetization behavior is even more remarkable. Despite the very distinct details of the excitation process the magnetization dynamics were found to be identical. This indicates the importance of the amount of introduced energy in contrary to the details of excitation and thermalization of the distribution.

We simulate the experiments on Fe by Chekhov et al. but also on CoCu clusters. In comparison to the experiments we use relatively high excitation energies.

material	CoCu 1d			CoCu 3d			Fe	
E_{ph} in eV	0.1	1.5	3.1	0.1	1.5	3.1	$4 \cdot 10^{-3}$	3.1
τ in fs	50	10	10	50	10	10	3000	100
F in mJ/cm ²	0.1	10.6	33.6	0.18	13.1	33.6	$2 \cdot 10^{-4}$	32.9

Table 4.1.: Fluences applied in simulations with different photon energies and pulse widths shown in Figures 4.17 and B.2.

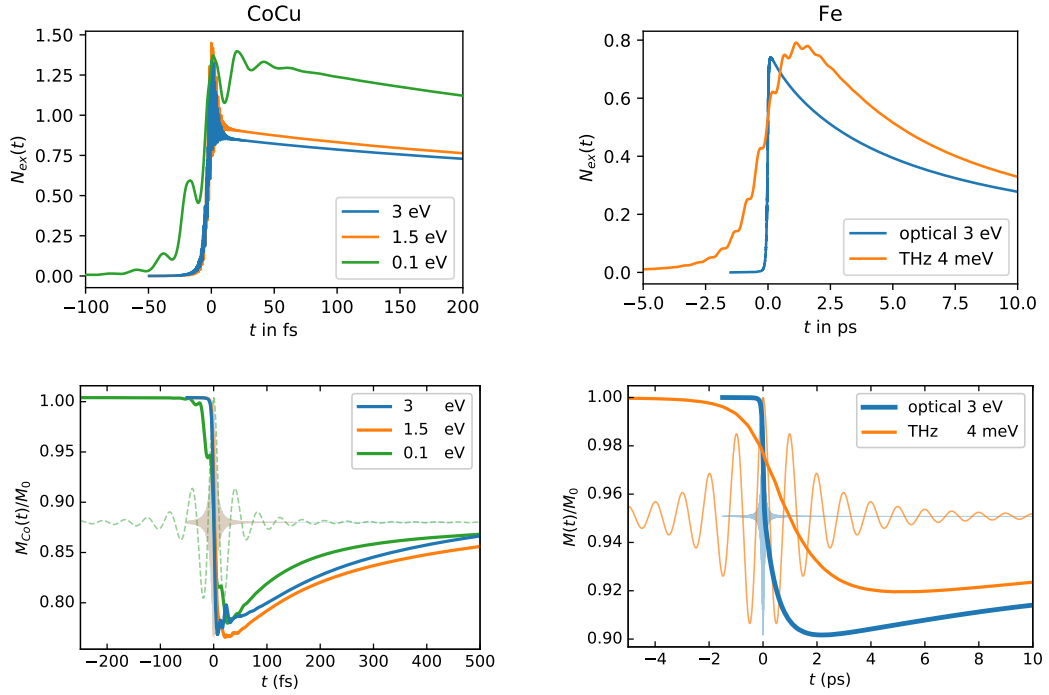


Figure 4.17.: On the left the number of excited electrons in a CoCu layer is shown together with demagnetization of the Co layer for selected photon energies. On the right the respective results for an Fe cluster under optical and THz excitation are presented. The laser pulses are indicated as thin, dashed lines.

Table 4.1 lists applied frequencies and fluences for systems under examination: a CoCu chain and a 3D CoCu cluster as introduced before and a 10×2 -atomic bcc iron cluster. The fluences were chosen as to receive a consistent degree of excitation. For this purpose the maxima of $N_{ex}(t)$ were compared. The corresponding graphs are presented in Figure 4.17 together with the temporal evolution of magnetization. For low frequencies longer pulse widths were chosen with a sufficient number of optical cycles. The different pulse widths are indicated by faint lines. Unlike in [108] the temporal magnetization signal was not refolded. Therefore in case of a broader pulse width also the magnetization dynamics are stretched over a longer time span. Apart from this the time evolution of demagnetization coincides very well throughout all simulations. In CoCu three different photon energies were applied: 0.1 eV, the default value in this thesis of 1.5 eV and 3 eV. While the Fe sample was excited with an optical radiation of 3 eV and a THz radiation of 4 meV. This corresponds to an enormous difference in timescales. In this case very broad pulses were applied and the dynamics are shown on the scale of picoseconds. But nevertheless a comparable demagnetization was achieved for both frequencies. A small delay in de- and re-magnetization can be explained by the broader pulse width. Further results can be found in Figure B.2 in the appendix.

To conclude, the `EVOLVE` code can simulate also very low excitation frequencies if pulse width and amplitude are tuned accordingly. Furthermore the statement of [108] is corroborated: Throughout different excitation regimes the underlying microscopic processes may be quite different but a similar demagnetization is generated, if the amount of absorbed energy is comparable.

4.2.8. Varying bath parameters

The bath comprises the interaction of the electron system with other quasiparticles. In our simulation such scattering events are not accounted for microscopically but in form of transition probabilities. The bath yields the possibility to include relaxation into the simulation of magnetization dynamics by mediating transitions between eigenstates at different energies. An important feature of the bath is therefore to take the laser energy out of the system and to enable a simulation of remagnetization.

The coupling to an external heat bath also introduces dephasing, a reduction of coherences embodied in the offdiagonal elements of the occupation matrix (cf. Section 2.3 and Ref. [57]). The excitation triggers such coherences that manifest for example as currents and yield oscillations of the occupation in the atomic orbitals. In realistic systems reflections of currents at the edges and the interface and also scattering events with impurities destroy the coherence of the quantum mechanical states. The dephasing damps the currents and establishes a locally stable situation. In this sense the dephasing contribution is within the current implementation and at the timescales observed, a crucial effect of the external bath.

The interaction with the bath is simulated without considering the details of the underlying microscopic scattering processes. The bath is implemented on the level of eigenstates and information of atomic character and localization are not taken into

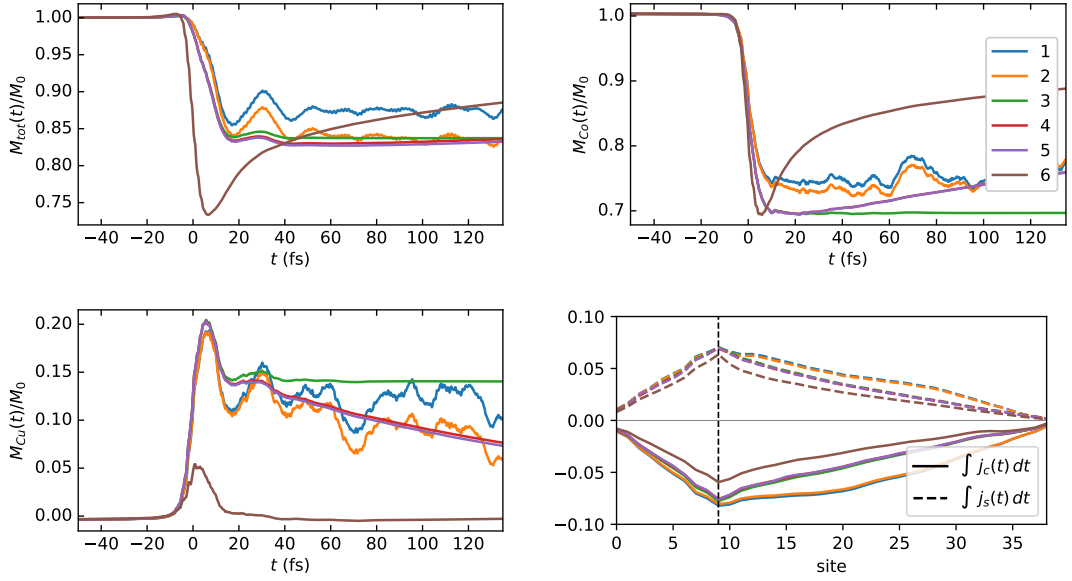


Figure 4.18.: Magnetization dynamics of the total system (top left), of the Co layer (top right) and of the Cu layer (bottom left), after excitation in a chain of 10 Co and 30 Cu atoms. The colors represent different bath parameters which are specified in Table 4.2. In the lower right panel the integrated currents are compared as introduced in Figure 4.12.

account. In other words, the transition probability just depends on the energy, the occupation and the spin character of the corresponding eigenstates. Eigenstates can be distributed over several atoms or localized at various specific positions within the sample. Therefore a bath-generated transition between different eigenstates can at the same time also be a local displacement of occupation or a redistribution between different atomic species. These can, to a certain degree, be considered unphysical effects.

Since the bath operates on longer timescales, changes of corresponding parameters have just minor impact on the demagnetization which happens on much shorter time scales. Instead the transition rates influence the subsequent remagnetization behavior. Within the applied setting (see Section 4.1), the pure dephasing contribution is the only fast acting component of the bath with a timescale of about $\gamma_{\text{dp}}^{-1} = 20$ fs. This contribution is energy conserving and does not imply any transition or yield any remagnetization dynamics as a direct effect. It only suppresses oscillations of occupation and magnetization, as can be clearly seen in Figures 4.18 and 4.19.

These Figures demonstrate the influence of various bath parameters on magnetization dynamics in the CoCu chain introduced before. While in Figure 4.19 only the dephasing parameter γ_{dp} is varied independently, in Figure 4.18 each graph represents a coupling to the bath, specified in Table 4.2. The mentioned oscillations are

	1	2	3	4	5	6
γ_{sc} (ps ⁻¹)	0.0	0.2	0.0	0.2	0.2	2.0
γ_{sf} (ps ⁻¹)	0.0	0.002	0.0	0.0	0.002	2.0
γ_{dp} (fs ⁻¹)	0.0	0.0	0.05	0.05	0.05	0.05

Table 4.2.: Bath parameters applied in Figure 4.18 as defined in (3.61). The first row shows the spin conserving transition rate, the second row the spin-flip transition rate and the third row the dephasing rate.

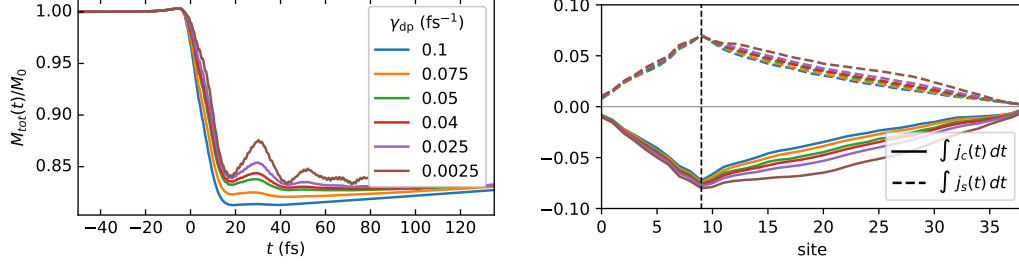


Figure 4.19.: Magnetization dynamics of the total system (left) and integrated currents as in Figure 4.18 for varying γ_{dp} .

clearly visible in Graph 1 (blue) and Graph 2 (orange). They represent calculations without and with a coupling to the heat bath, but both without a pure dephasing contribution. In all other settings the oscillations are present merely in form of a delicate modulation during or directly after optical excitation.

The counterparts of Graphs 1 and 2 are Graph 3 (green) and Graph 5 (purple), which are both calculated including a pure dephasing. This correspondence is slightly visible in the magnetization dynamics of the Cu layer. In calculations with a coupling to the heat bath (Graphs 2 and 5) the excess magnetization therein is reduced, while in Settings 1 and 3 no energy is lost to the environment and the magnetization stays at an reduced level in Co and an enhanced level in Cu. Setting 5 corresponds to the default parameters that were used throughout the previous sections. The corresponding results are almost identical to Graph 4 (red), where no bath mediated spin-flip transitions are allowed. Within the investigated time regime the spin-flip parameter does almost not influence the dynamics.

The strongest demagnetization is observed at Graph 6 (brown), with an unrealistic high coupling to the bath associated to high transition rates on the order of 2 ps^{-1} . But it also exhibits the lowest accumulation of magnetization within the Cu layer. The demagnetization of the total system follows the demagnetization of the Co layer almost instantly. The strong coupling to the bath seems to immediately remove the excess magnetization in the Cu layer. In this setting the magnetization can exceed the initial magnetization during the remagnetization process. In this case, a gain of magnetization is an unphysical phenomenon, which reveals a limitation of our model.

In general the demagnetization of the total system is slightly enhanced together with pure dephasing or the transition rates, while the accumulation of magnetization in the Cu layer is slightly decreased. The transport of spin across the interface stays constant for a broad range of parameters. Only its extent into the respective layers is slightly reduced for higher dephasing parameter values. Figure 4.18 shows that the transport across the interface is instead reduced by large transition rates γ_{sc} and γ_{sf} . The weakest demagnetization is observed if no coupling to the bath is applied at all. Bath-generated transitions described by γ_{sc} and γ_{sf} accordingly seem to enhance the demagnetization of the total system. But they only have a minor effect on the demagnetization within the Co layer.

A possible improvement of our model is the usage of an energy-dependent electron-phonon scattering probability to calculate the transition rates. In an even further elaborated approach the atomic character of the corresponding eigenlevels is taken into account and an energy- and material-dependent scattering probability can be applied.

4.3. Other material combinations

Throughout the preceding sections the physical mechanisms at an FM|NM interface were investigated using the example of a cobalt-copper bilayer system. In this section further material combinations shall be examined. Apart from copper also aluminum, platinum and gold are used as nonmagnetic materials, while nickel replaces cobalt as magnetic layer in some simulations. As described in Section 4.1 the interface was constructed in a simplistic manner. No relaxation of the lattice was taken into account and the interfacial hopping parameters were taken as the mean value of both materials. To simulate an interface realistically a more sophisticated model is needed. The ambition of this section is not to claim technical feasibility or correctness of the interface model, but to identify different mechanisms of spin transport and demagnetization.

The simulations were performed for the geometries presented in the previous sections: a chain of 10 magnetic and 30 nonmagnetic atoms, and a two-dimensional cluster of 20 magnetic and 20 nonmagnetic atoms. Both setups exhibit periodic boundaries parallel to the interface. First the time evolution of magnetization is studied and it follows an analysis of spin and charge currents through the chain systems.

4.3.1. Comparison of magnetization dynamics

The results for the magnetization dynamics are shown in Figures 4.20 and 4.22 and are analyzed as described in Equation (4.3). The contributions of the total system, the magnetic layer and the nonmagnetic layer to the change of magnetization are each shown with respect to the initial magnetization of the total system M_0 . In this way these figures show the percental change of magnetization in the respective layer.

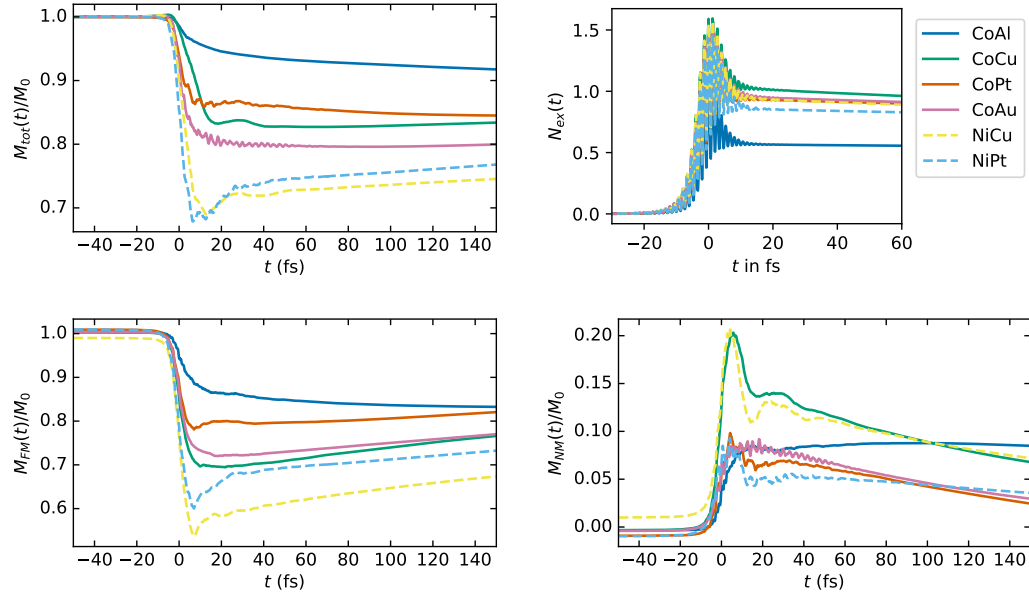


Figure 4.20.: Magnetization dynamics in a chain after laser excitation centered at 0 fs for different material combinations. Total magnetization and number of excited electrons are shown in the top row left and right; magnetization of FM (NM) layer is shown in the bottom row left (right).

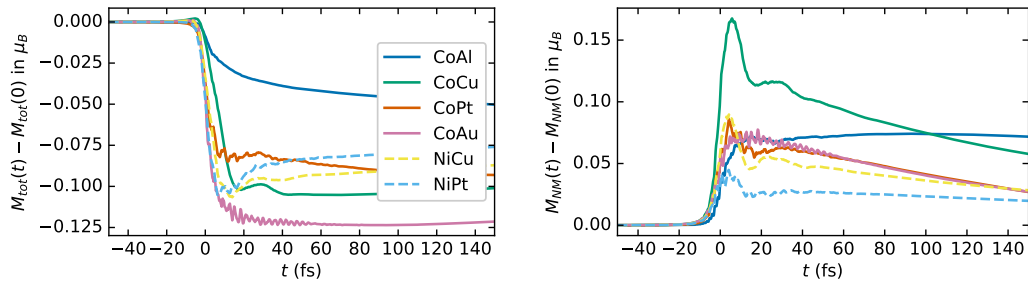


Figure 4.21.: Results of Figure 4.20 presented as changes to their initial value in μ_B . The time evolution of magnetization in the FM (NM) layer is shown on the left (right).

Since Co and Ni exhibit different initial magnetic moments, additionally the absolute change of magnetization is presented in Figure 4.21. EVOLVE simulations of FM|NM chains yield magnetic moments of about $2.4\mu_B$ for Co and $1.3\mu_B$ for Ni atoms. Those values are a little higher than values from literature of $1.8\mu_B$ and $0.7\mu_B$ for Co and Ni bulk systems, respectively [109], but show a correct tendency. The simulated as well as the measured magnetic moments change with the cluster geometry. The restricted geometry of the chain-like supercell explains the deviation between values from literature and simulation. Despite the significant difference of initial magnetization Ni as well as Co layers exhibit a comparable degree of absolute demagnetization, shown in the left of Figure 4.21. Though in terms of percental changes as in Figure 4.20 the Ni layers exhibit the largest demagnetization. Similarly the excess magnetization in the NM layer is quite large in combination with Ni, when compared to M_0 . But in terms of μ_B this translates to rather small values (Fig. 4.21 right). In the following mostly the percental changes will be discussed.

The observation of Figure 4.11 is confirmed by a comparison of all material combinations, which reveals the importance of the spin-orbit coupling of both layers for the degree of demagnetization. The respective strength of the SOC within the various materials is visualized in the right-hand side of Figure 4.23. Of all magnetic materials nickel exhibits the strongest SOC. Therefore a higher demagnetization can be achieved in equivalent systems just by replacing Co with Ni atoms. SOC introduces spin-mixing into the Hamiltonian which converts majority-spin to minority-spin electrons and vice versa. In addition to the strong demagnetization by spin transfer across the interface a high SOC yields a considerable demagnetization by spin flips already within the magnetic layer.

But on top of that also a strong SOC within the nonmagnetic layer generates a higher demagnetization. The nonmagnetic layer serves as a reservoir for angular momentum transferred to it from the magnetic layer either as a majority current from or a minority current into the magnetic layer. This leads to an accumulation of majority electrons or a depletion of the minority orbitals within the nonmagnetic layer, respectively. In this way the corresponding transfer process across the interface is mitigating itself in its progress. The SOC on the other hand counteracts the depletion or filling of only one spin channel. The coupling between both spin channels distributes the accumulation or depletion from one to both spin channels. In this way the transfer mechanism across the interface can proceed as there are empty majority orbitals or occupied minority orbitals available in the NM layer for a longer time.

The simulations of both geometries, depicted in Figures 4.20 and 4.22, corroborate the assumption about the importance of SOC in the nonmagnetic material. In the two-dimensional setup, shown in Figure 4.22, the strength of demagnetization displays precisely the strength of SOC in the nonmagnetic layer. The weakest demagnetization is observed by far in CoAl. In CoCu the demagnetization is roughly twice as strong, followed by even higher demagnetizations in CoPt and CoAu. Also the setups with Ni exhibit a stronger demagnetization if Pt is used instead of Cu. These results are in line with the order of SOC strengths displayed in Figure 4.23.

In the one-dimensional setup this order is slightly disturbed. The CoCu chain

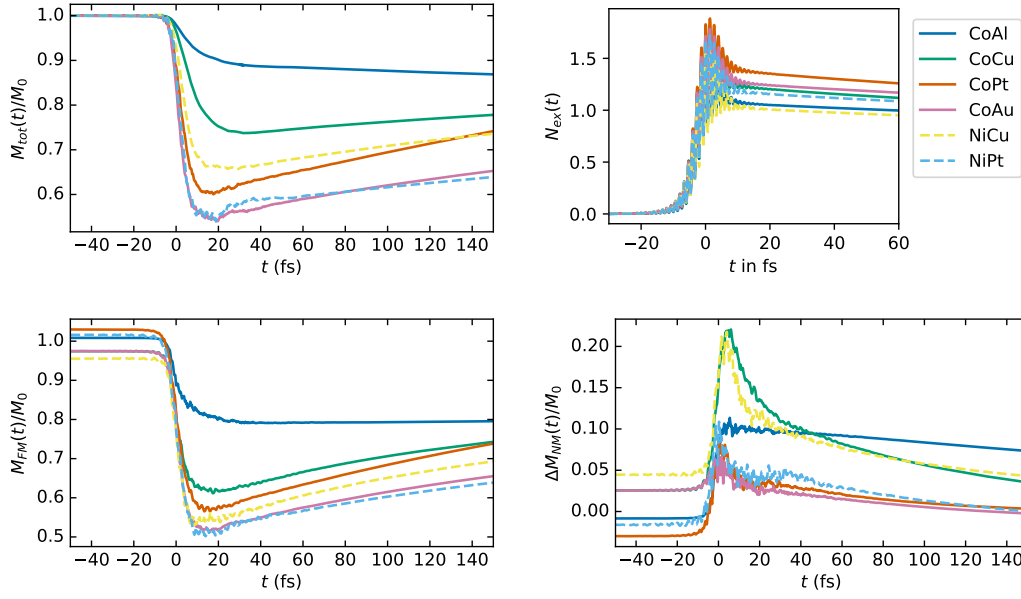


Figure 4.22.: A comparison of different material combinations as presented in Fig. 4.20 but for a two-dimensional setup.

exhibits an especially strong demagnetization, almost of the same order as in the CoAu chain. Possibly this is due to a particularly large spin transfer or effective excitation in the CoCu chain. The degree of excitation quantified by the number of excited electrons is depicted in the upper right of Figures 4.20 and 4.22, while transfer mechanisms and currents will be compared in the following section.

The number of excited electrons shows moreover also a weak excitation in CoAl. The reason thereof is the orbital occupation of aluminum with 3 valence electrons distributed mainly within the s orbitals and also sparsely in the p orbitals. In this case an electric dipole transition primarily happens between the s and p orbitals. Thus there are only few available orbital pairs with possible optical transitions. The optical excitation is thus less efficient than in materials with occupied d and vacant p orbitals. An excitation of electrons to higher energy orbitals and creation of empty orbitals in the NM layer facilitates the transport across the interface. In that sense the degree of optical excitation of the NM material is also relevant for the demagnetization of the FM layer. Therefore the outstanding orbital occupation of aluminum amongst the other nonmagnetic materials affects demagnetization by influencing the transfer mechanism across the interface.

The magnetization dynamics of the nonmagnetic layer is presented in the lower right of Figures 4.20 to 4.22. As for CoCu, an enhancement of magnetization in the nonmagnetic layer together with the demagnetization of the magnetic layer can also be observed for the other material combinations. Again the CoAl system stands

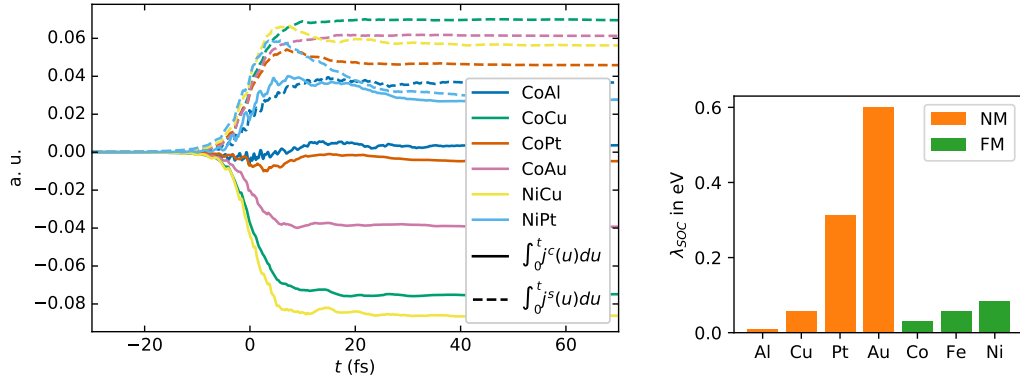


Figure 4.23.: Left: Charge currents (solid lines) and spin currents (dashed lines) through the interface integrated up to a time t , represented by the x -axis. Right: SOC parameters in d orbitals of different materials.

out among the other material combinations. The magnetization in the Al layer is enhanced similarly as in the other materials. But in contrast to the other materials the acquired magnetization in Al is not removed again right afterwards. Instead it exhibits a long lasting behavior. For one thing, the very small SOC parameter of Al retards the spin flip mechanism. For another, as visible in Figure 4.26, the occupation of Al changes mainly in the s and p orbitals and only slightly within the d orbitals. While the SOC is already very small in the aluminum d orbitals it is negligible in s and p orbitals. Therefore SOC induced spin-flips can only happen in the very scarcely occupied d orbitals.

Among the other material combinations those with a nonmagnetic Cu layer exhibit the strongest enhancement of magnetization followed by a rapid reduction of the same. In terms of absolute changes as shown in Figure 4.21 the CoCu system stands out even more clearly, also against the NiCu system. In Pt and Au layers with a very high SOC the magnetization exhibits a similar behavior. Here the quenching of excess magnetization manifests even more in the two-dimensional system. In the gold layer it exhibits a very strong and seemingly instantaneous quenching and drops even below the initial value. This is clear in contrast to the long-lasting excess magnetization in Al with minor SOC.

In summary, a stronger SOC in the FM layer and a stronger SOC in the NM both intensify the demagnetization. A strong SOC in the NM layer leads to a fast quenching of the magnetization received from the FM layer. While a weak SOC in the NM layer results in a long lasting excess magnetization.

4.3.2. Comparison of interface currents and spin transport

To shed more light on the underlying mechanisms of demagnetization it is necessary to also analyze the currents between both materials. Both, spin and charge current

across the interface are strongly oscillating (cf. Fig. B.3 in the appendix). To better quantify the importance of the currents for demagnetization both currents were integrated over time. Even though the currents are presented as sum or difference of spin-up and spin-down particle currents, for convenience the terms “transported charge” and “transported spin” will be used for the integrated values.

Transported spin by time

The integrated currents at the interface bond of the chain systems are presented in Figure 4.23 for a varying upper bound of the integration. The graph shows the amount of spin or charge transported through the interface up to a time t . Before the pulse no transport has happened yet and all graphs equal zero. The transport happens primarily during the laser excitation, where the biggest changes are visible in the signals. After the pulse at about 10 fs only weak currents are flowing through the interface, visible as minor changes. At 40 fs after the pulse peak the signal stays constant: the currents have disappeared.

The integrated spin current has a positive sign: It is flowing from the ferromagnetic into the nonmagnetic layer in all material combinations. The integrated charge current however shows a diverse behavior. In CoCu, NiCu and CoAu it shows a clear negative signal. In these cases the direction of the charge transport is opposite to the spin transport. The opposite signs together with very similar absolute values of charge and spin transport hints towards an almost pure minority current, flowing from the nonmagnetic into the magnetic layer.

In CoPt and CoAl, there is almost no net charge transport, while NiPt even shows a charge transport parallel to the spin transport. This suggest that in those cases the majority currents become relevant or even dominant. However, in those samples there is less net spin transport across the interface. The largest net spin transport is observed across the interface in CoCu, followed by CoAu and NiCu chains. A pure minority or majority current seems favorable for a large spin transport. Also it is noteworthy that, while both Ni systems exhibit a high peak value of transported spin, they are not among the systems with high absolute demagnetization (Fig. 4.21).

In case of the NiPt chain the amount of transported spin reaches a fairly high value during optical excitation. But afterwards it decreases and in the end it shows the lowest net spin transport of the investigated material combinations. This behavior can be explained by a strong spin current from Ni to Pt followed by a weaker spin current in the opposite direction. This reversal of the spin current direction can be observed also in NiCu, although less pronounced.

Finally in comparison with Figure 4.20 one can observe that a high net spin transport across the interface not necessarily corresponds to a high demagnetization and vice versa. On the contrary, NiCu, the system with the least net spin transport across the interface exhibits the largest total demagnetization. It seems that the crucial magnitude in Figure 4.23 is not the final value but the slope during optical excitation. The graphs with the fastest increase of transported spin show the strongest demagnetization within the ferromagnetic layer. A better correspondence

with the net transported spin can be found in comparison to the peak of excess magnetization in the nonmagnetic layer, shown in the bottom right of Figure 4.20. However, in case of a high SOC in the nonmagnetic layer, as CoAu and CoPt, this correspondence fails.

Site- and orbital-resolved spin transport

Further detailed information about the currents is presented in Figure 4.24. For each material combination it shows the local distribution of the integrated currents. As in Panel b of Figure 4.12 the integration was constrained to the relevant time interval, starting at the beginning of the simulation, 50 fs before the pulse, until 70 fs after the pulse peak when the currents have vanished. The values at the interface are identical to those shown in Figure 4.23 at $t = 70$ fs.

In addition, the orbital composition of the involved currents is shown for this interface bond. Each bar represents the amount of occupation transported by currents between specific orbitals. For example j^{sp} shows the amount of occupation transported by currents flowing from s to p orbitals and vice versa. The color of the bars highlights the spin character of the orbitals, while the sign gives the direction of the transport. Therefore the sum of all contributions translates to the integrated charge current at the interface, displayed by the blue line, while the difference of contributions from spin-up and spin-down currents translates to the integrated spin current at the interface, displayed by the orange line.

Throughout all material combinations the transport of spin along the x -direction, from the magnetic into the nonmagnetic layer, is maximal at the interface. This substantiates again the importance of the interface as source and origin of spin current. In Cu and Al layers the maximal value at the interface decreases slowly, almost linearly towards the boundary of the sample. Therefore in the middle of the Cu layer, far away from the interface, there is still a significant spin transport happening along the chain direction. Within the Au layer the amount of transported spin decays at first very abruptly and then also almost linearly with the distance from the interface.

In Pt layers the behavior of spin transport is more irregularly and vanishes already at about 15 sites away from the interface. After reaching a maximum the integrated spin current in NiPt decreases (Figure 4.23). This behavior suggests the existence of a spin current in Pt counteracting the dominant spin current in x -direction at later times. Therefore the results from Figure 4.24 are reevaluated in Figure 4.25 with the upper bound of the integration reduced to $t = 5$ fs after the pulse peak. In this way just the immediate dynamics during the pulse peak contribute to the result, while the subsequent dynamics is excluded. The color plot in the left-hand side of Figure 4.25 visualizes in red the strong initial spin current along the x -direction from Ni into Pt, followed by a weaker spin current in opposite direction in blue. The new results of the integration are shown on the right-hand side. Therein, the irregular behavior and the fast decay visible in Figure 4.24 are absent. Instead the amount of transported spin and charge decays almost linearly from the interface towards the end of the Pt layer, with a prominent peak directly at the interface. From this it is

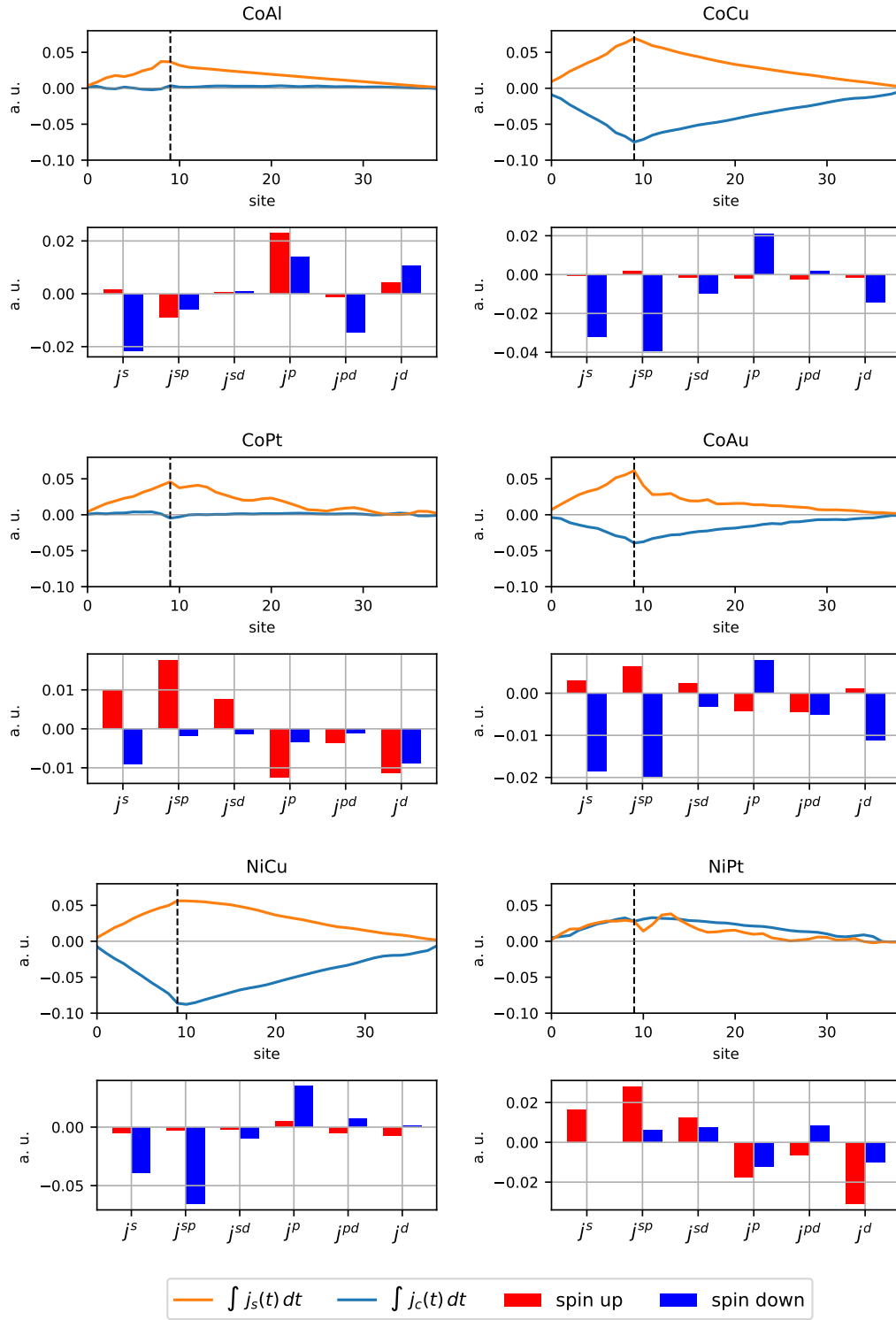


Figure 4.24.: Local distribution of transported spin (charge) depicted as orange (blue) lines for each bond along the chain. For the current between the interface sites (dashed line) the orbital contributions are shown.

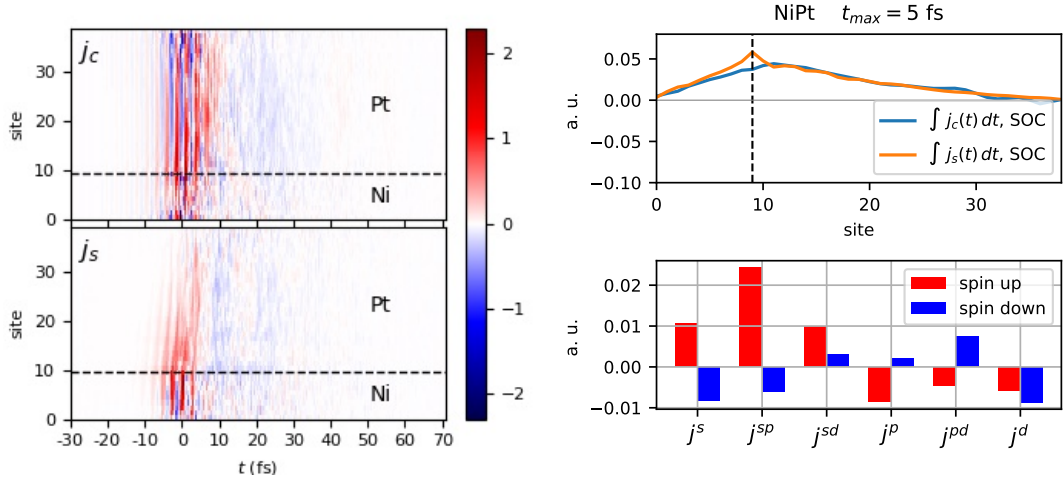


Figure 4.25.: Charge and spin currents in a NiPt chain (left) and the local distribution and orbital composition of transported carriers up to $t = 5$ fs after the laser pulse (right).

evident that the irregular behavior and fast drop of the signal within the Pt layer is caused by the contribution of the secondary spin currents flowing back from Pt into Ni. Furthermore, the agreement of signals from spin and charge transport reveals that in this sample the early dynamics is almost solely caused by majority currents from Ni into Pt. Indeed the breakdown of the orbital composition shows a major contribution of majority sp currents along x -direction, followed by s and sd currents.

This is in clear contrast to other material combinations (CoCu, CoAu and NiCu), where the spin transport is contrasted by a charge transport in the opposite direction, indicating a spin transport dominated by minority carriers flowing in $-x$ -direction instead of majority carriers in x -direction. In these materials the orbital breakdown shows almost no transport between majority orbitals. Especially in CoCu and NiCu only the minority currents determine the dynamics. Mostly sp followed by s and sd minority currents in $-x$ -direction are the driving force of the spin current in $+x$ -direction. While minority p currents are flowing from the FM into the NM material, thereby counteracting the dominant spin transport.

The minority d currents that were discussed for a CoCu chain in connection with Figure 4.8 are also visible. However, their contribution to the spin current is significantly smaller than the contributions of minority s and sp currents. Minority d currents flowing from the NM into the FM material are strongest in CoAu. CoCu, CoPt and NiPt exhibit weaker minority d currents. While in NiCu they cannot be observed at all. This difference can be attributed to the band structure of nickel. In comparison with cobalt in nickel there are less available empty minority d orbitals. Therefore the transfer of minority electrons is weaker from Cu into Ni than from Cu into Co. Borchert et al. [101] discussed the amount of empty minority d orbitals

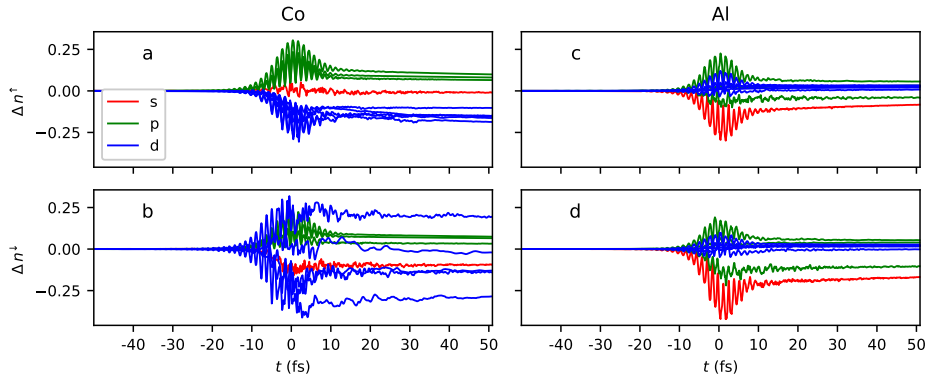


Figure 4.26.: Change of occupation in spin and orbital resolution in a chain of Co and Al atoms. On the left side majority (a) and minority (b) orbitals in Co and on the right side majority (c) and minority (d) orbitals in Al are shown. The orbital character is indicated by the color.

in the ferromagnetic material to explain the difference in demagnetization of NiPt, CoPt and FePt. And indeed by comparing CoPt and NiPt we find a stronger minority d current in CoPt. Nevertheless this minority d current is not the only transfer process that generates a fast and strong demagnetization. As discussed before, in NiPt instead majority currents are dominant. So that in the end the simulated demagnetization is even higher in the NiPt chain than in the CoPt chain.

In CoPt and CoAl current contributions in x - and in $-x$ -direction are balanced. Therefore, there is no significant charge transfer in these samples. The transfer processes in CoPt are similar to those in NiPt whereas CoAl shows a very unique behavior. This is due to the electronic structure of aluminum which is a light metal with only three valence electrons in contrast to the other nonmagnetic materials which are heavy metals with 10 or 11 valence electrons. The d levels in Al are located at high energies. They are unoccupied before the laser excitation and d currents can just flow from Co into Al. Therefore, compared to other NM materials, the minority d current in Al can only be observed along the reversed direction, counteracting the spin transfer from Co to Al. Analogously to Figure 4.5 for CoCu, Figure 4.26 shows the change of orbital occupation at the interface sites of a CoAl chain. In Al the laser pulse induces transitions from occupied s orbitals to unoccupied p orbitals, visible as loss of occupation in s orbitals (in red) and gain of occupation in p orbitals (in green). An optical transition between p and d orbitals becomes relevant only in later times, when enough occupation was already excited to the p orbitals. The loss in one of the Al p orbitals can be attributed to the minority pd current flowing from Al into Co. Figure 4.24 shows that the spin current from Co into Al seems to be generated by minority s and minority pd currents in $-x$ -direction and by a majority p current in x -direction. All in all the less favorable transport conditions in aluminum explain also the less efficient demagnetization.

Finally, it must be noted that the transport properties are depending also on the dimensionality of the simulated system. In the paragraphs above chain systems were analyzed. Here only one nearest neighbor link connects both materials across the interface. While at a real two-dimensional (100) interface transport can happen along more links and along links pointing not just in xz - but also in xy -direction. Those differences in cluster geometry and their influence on simulated transport have yet to be analyzed.

In summary, there is a multitude of parameters that influence the demagnetization and transport behavior of FM|NM systems under optical excitation. The electronic structure of the materials determines available occupied and empty orbitals. This does not only influence the efficiency of excitation but also the efficiency of transport across the interface. The major factor in demagnetization is the strength of spin-orbit coupling. Furthermore, a strong transport across the interface also promotes demagnetization. In this it is important to consider not only the total net transport but also subsequent transfer processes. An orbital breakdown of these transfer processes reveals a variety of mechanisms. While in some systems minority currents are dominant, in others it is majority currents or a mixture of both. Therefore there is no simple scheme, which attributes the degree of demagnetization to the number of occupied or unoccupied states of just one spin or orbital character. Instead all orbitals and associated currents have to be taken into account.

4.4. Ferromagnetic systems - extending the model

During the previous sections it was shown that simulations with *EVOLVE* yield good and interesting results for FM|NM systems in a regime of relatively strong excitation. However, in case of pure ferromagnetic systems the model does not sufficiently represent the relevant physics of demagnetization.

An approach to simulate more realistic demagnetizations is the so-called feedback effect. It involves a reduction of exchange splitting and will be examined in Section 4.4.3.

Further discussed mechanisms are enhanced spin precession and enhanced stochastic dynamics as simulated in atomistic spin dynamics simulations and, coming along with this, a breakdown of nearest neighbor spin correlation. On the other hand a collective rearrangement of the spin orientation axis is interpreted as demagnetization by magnon generation. For both cases it would be necessary to incorporate a dynamical tilting of the spin axis into the simulation. As a first step towards a dynamic spin orientation axis it is necessary to extend the model to static noncollinear setups. With this it is possible to account for “initial magnetic disorder” [48]. A finite tilting of the local spin quantization axis with respect to the global quantization axis results in additional spin-mixed Hamiltonian elements and can thus lead to enhanced ultrafast demagnetization.

A third approach explains demagnetization on the basis of spin currents. Here the magnetic moment is not decreased in the first place, rather it is primarily redistributed to other parts of the sample and eventually reduced by subsequent spin-flip

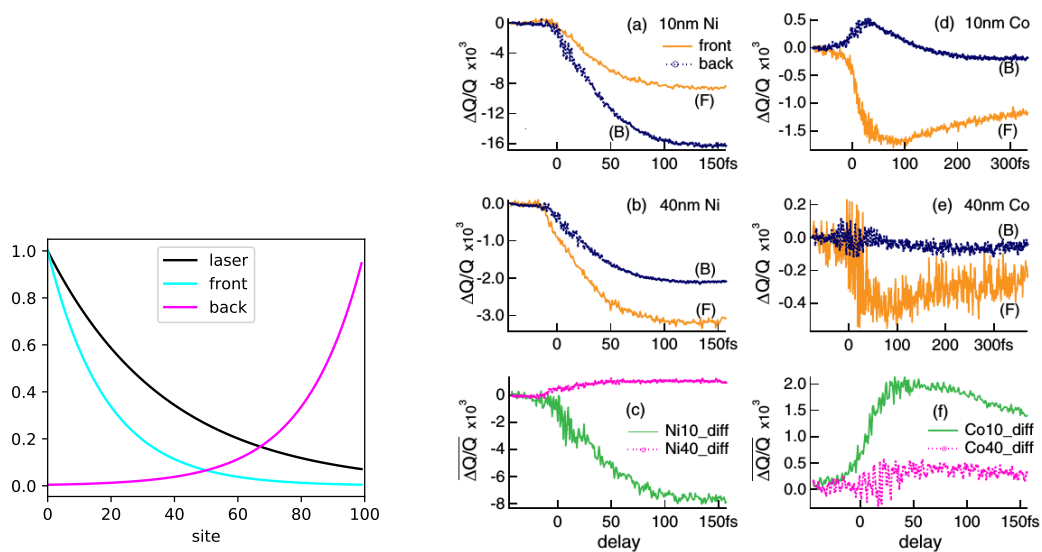


Figure 4.27.: The left graphic shows as a black line the decrease of the electric field throughout the sample as applied in simulations and as colored lines the weighting profile to segregate contributions from the front- and backside of the sample. On the right, results from [17] show the demagnetization measured at front- and backsides of Co and Ni samples.

processes. Such a spin current is always driven by a gradient. In the bilayer systems discussed in the previous sections, this gradient was the local imbalance of excited occupation at the interface. In a homogeneous ferromagnetic systems the dominant gradient is the decay of laser intensity with the distance to the surface. By shrinking the length scales this mechanism can also be investigated with EVOLVE despite the limited cluster sizes. The corresponding results will be presented in the following Section 4.4.1.

4.4.1. Spin current generated demagnetization in ferromagnets - excitation with an intensity profile

Within an authentic simulation a sample of several monolayer width is not excited by the laser homogeneously. Instead the laser intensity decreases as in every layer of the sample some laser light is absorbed. Within in a large metallic system therefore a gradient of excitation is present, which can influence the subsequent dynamics. Due to this gradient a transport takes place and contributes to the demagnetization at the foremost layers. For irradiation in x -direction the intensity of the light is attenuated exponentially while passing through a medium

$$I(x) = e^{-\alpha x} \quad , \quad \text{with} \quad \alpha = \frac{4\pi\kappa(\lambda)}{\lambda} . \quad (4.4)$$

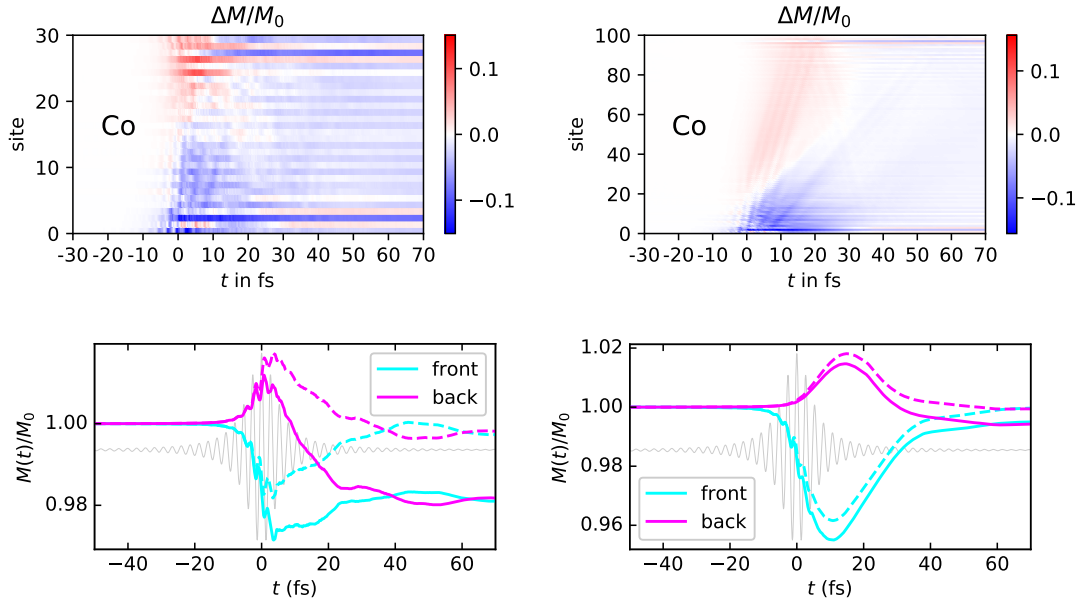


Figure 4.28.: Magnetization dynamics in a chain of 30 (left) and 100 (right) atoms of Co. The applied laser intensity decays towards the backside of the layer. The dashed lines show results calculated without SOC.

Its penetration depth depends on its wavelength and can be calculated from the absorption coefficient $\kappa(\lambda)$, the imaginary part of the material-dependent complex refractive index $\underline{n}(\lambda) = n(\lambda) + i\kappa(\lambda)$. The laser intensity is proportional to the square of the electric field. Accordingly the electric field amplitude decreases with

$$E_0(x) = e^{-\frac{\alpha}{2}x} E_0 . \quad (4.5)$$

Values for $\kappa(\lambda)$ can be found in material databases [110], [111]. In the considered transition metals the amplitude is typically reduced to 50% in the range of 18 nm to 30 nm. For test simulations a laser profile as presented in Figure 4.27 is chosen and applied to Co and Ni layers likewise. The damping of a much thicker layer can be modeled by applying an artificially strong absorption coefficient. In this way the influence of the gradient in excitation is more pronounced in the simulation results. By this procedure thick layers can be simulated, which are otherwise not treatable with the EVOLVE code in reasonable computational time.

Figures 4.28 and 4.29 present simulation results for pure Co and pure Ni chains. By applying periodic boundary conditions orthogonal to the chain and a tetragonal unit cell as in the previous sections, those setups correspond to layers of various thickness as used by Shokeen et al. [17] (Figure 4.27 right). In an experimental setup magneto-optical measurements average over many sites, with the contribution of the sites also decaying exponentially from the front to the interior of the sample. To observe the enhancement of magnetization by transport, a measurement at the

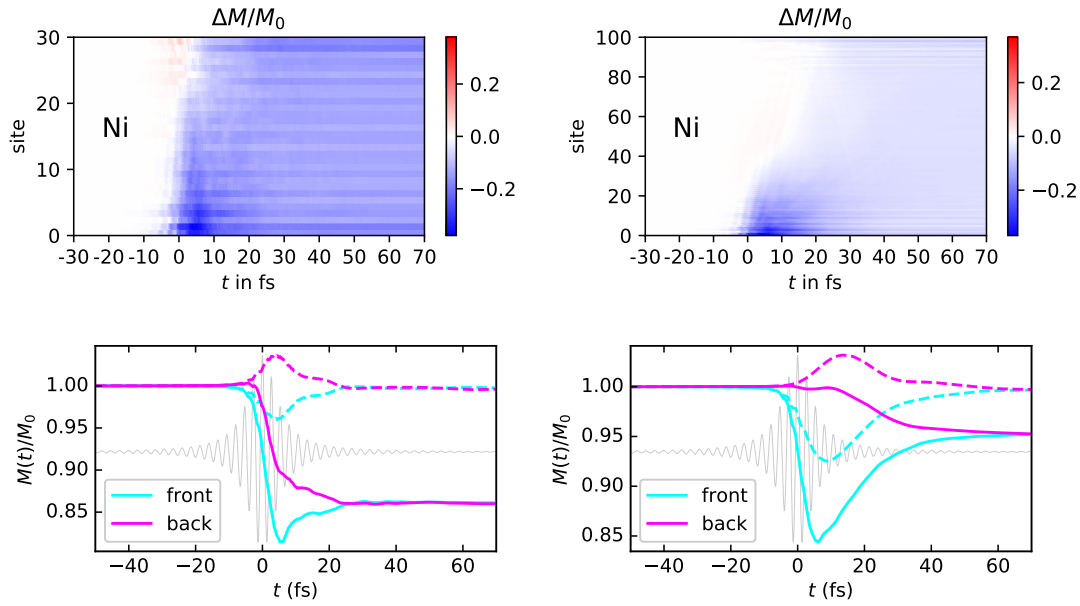


Figure 4.29.: Magnetization dynamics in a chain of 30 Ni atoms (left) and 100 Ni atoms (right). As in Figure 4.28 the dashed lines show results without consideration of SOC.

backside of the sample is necessary. In accordance to those optical measurements of front- and backside, also the results of the simulation are separated into a front- and a backside signal. To that end the contribution of each site along the chain is multiplied with a weighting function as shown in Figure 4.27.

In the case of a thin Co layer (10 nm) Shokeen et al. measured a demagnetization at the front and enhanced magnetization at the back of the sample. A similar magnetization behavior was measured in a thicker Co layer (40 nm). However in this case no clear enhancement of magnetization could be observed at the backside. The simulation results presented in Figure 4.28 nicely reproduce the decrease of magnetization at the front and enhancement of magnetization at the backside of the layer. However, within the simulation both thicknesses are in good agreement to the thin layer experiments, while the thick layer is not reproduced as well. Additionally in the simulations a uniform contribution of magnetization is visible already after 50 fs. In the model the dephasing contribution acts on a timescale of 20 fs and smoothes local imbalances. Therefore front- and backside signal become identical on a similar timescale. In the experiment front- and backside magnetizations keep a distinct difference also for times longer than 300 fs.

Calculations of a Ni sample excited with a decreasing laser pulse are in good agreement with the experiment, too. Results from the simulation in Figure 4.29 as well as from the experiment exhibit no significant enhancement of magnetization at the backside, as they did in the Co sample. Instead a strong demagnetization

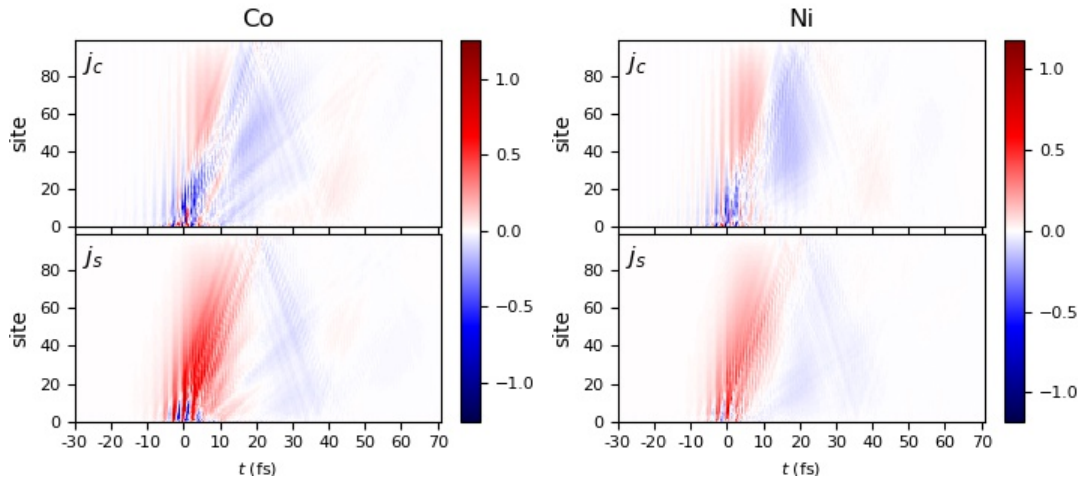


Figure 4.30.: Charge and spin currents in chains of Co and Ni, with 100 atoms each.

is observed at both sides. In the thin Ni layer even a stronger demagnetization is measured at the backside of the sample. In contradiction to that the simulation shows slightly stronger demagnetization at the frontside, even though front- and backside signal are quite similar and meet already at 25 fs. In the thick layer the demagnetization at the backside is much weaker than at the frontside, which is again in good agreement with the experiment. In general in Ni the overall dynamics is governed by a strong demagnetization at every site of the chain. This is caused by a relatively strong spin-orbit coupling.

In this simulation two different mechanisms contribute to the ultrafast demagnetization of the front-side: transfer of spin momentum to the backside and SOC induced spin-flips. The only global channel of ultrafast demagnetization is the SOC, besides the bath which works on longer timescales. To compare the importance of spin transport and SOC-induced spin-flip for demagnetization, calculations without SOC were performed. They are represented by dashed lines in Figures 4.28 and 4.29. In homogeneously excited systems no demagnetization is expected without SOC. But by using a decreasing laser profile also calculations without SOC exhibit a finite demagnetization at the frontside. In Co calculations with and without SOC are almost identical, while a huge difference is visible in case of Ni. Both signals of demagnetization coincide at the beginning of time evolution and optical excitation. They differ when the contribution of SOC starts to dominate the dynamics. This happens very early, a few fs after the pulse peak. In this sense we do not really find two separate time regimes as is claimed in [17]. Instead both mechanisms, SOC and spin transport, are visible from the beginning of excitation. However, on longer timescales demagnetization by SOC determines the temporal evolution.

The transport through Co and Ni layers can also be studied in terms of spin and

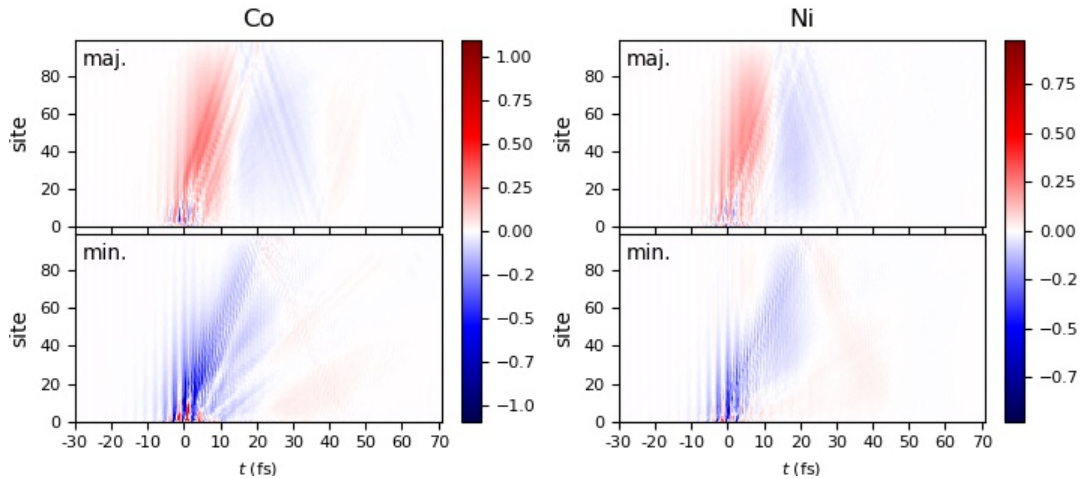


Figure 4.31.: Majority and minority currents in chains of Co and Ni, respectively.

charge currents, shown in Figure 4.30. In both materials a spin current starting at the frontside and propagating to the backside is clearly visible. This proves, that there is a strong spin transfer from the frontside to the backside in Ni as well. But in Ni both currents are slightly weaker than in Co. Figure 4.31 shows majority and minority currents in both systems. It is noteworthy that in both materials majority and minority currents contribute equally to the spin transport and not just majority currents as proclaimed by the theory of superdiffusive spin currents. Indeed the contribution of minority currents, especially between s orbitals is even bigger than of majority currents. This is apparent also from the analysis of orbital contributions in Figure 4.32. On the other hand the majority currents seem to extend over the whole chain, while the minority currents are located more at the frontside. Also the influence of SOC on spin and charge currents is shown by comparing solid and dashed lines in the top panels of Figure 4.32. While without SOC both currents do not change in Co, in Ni the spin current is visibly reduced by SOC. But even without SOC spin currents in Ni are weaker than in Co. On top of this the amount of transported spin is remarkable in both materials. Its magnitude is comparable to that of interface generated transport presented in Figure 4.24.

The different signals from Co and Ni therefore arise from differences in SOC and transport behavior of both materials. Already without SOC Ni develops a weaker spin transfer to the backside, which is suppressed further by the presence of SOC. On top of that the strong SOC in Ni generates a stronger overall demagnetization and superimposes any other behavior. Demagnetization by transport is thus less or not visible.

The above leads to the following conclusions: Upon excitation with a declining laser profile in homogeneous ferromagnets spin transport and SOC both contribute

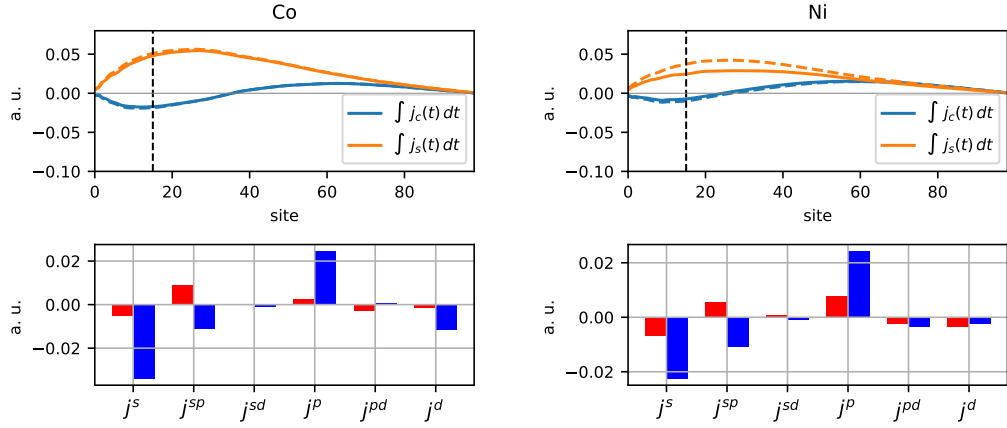


Figure 4.32.: Charge and spin currents integrated from -30 fs to 10 fs through bonds along a chain of 100 Co (left) and 100 Ni (right) atoms. Calculations without SOC are depicted as dashed colored lines. Orbital contributions to currents through the bond indicated by the dashed black line are represented by the bar charts.

to the demagnetization at the frontside. In general spin transport is the dominant contribution, but it is more important for materials with weak SOC. The magnitude of spin transport generated by a decreasing laser profile is comparable to the magnitude of spin transport generated by an FM|NM interface.

Finally it shall be noted, that in principle any kind of inhomogeneity in a system yields an inhomogeneously excited occupation. This in turn translates to a local gradient of occupation numbers which can generate spin transport. The decreasing laser intensity generates a uniform gradient in excitation and therefore is an important source of spin transport in every experiment. On the other hand inhomogeneities of occupation at surfaces mostly generate an oscillating profile of excited occupation and yield a disruptive signal in addition to the dominant signal. The importance of interfaces as sources of spin transfer was already discussed extensively. In addition a magnetic field gradient could be a further possibility to generate a uniform gradient in excitation and generates similar transfer results as presented above.

4.4.2. Noncollinearity

So far all spins were aligned along the z -axis. This constraint has to be eliminated in order to simulate also noncollinear structures. On the one hand noncollinear antiferromagnets are a promising material class for further investigation, on the other hand noncollinearity is needed to simulate initial disorder of the spin alignment as described by Chen et al. [48].

In a noncollinear spin texture each site i has its individual, local coordinate system and its z -axis is the local spin quantization axis (SQA). In the global frame the

local SQA points along \mathbf{n}_i , a vector that is tilted towards the global z -axis by an azimuthal angle φ_i and a polar angle θ_i . In the local frame of site i $\chi_i^{+\text{loc}} = (1, 0)^\top$ and $\chi_i^{-\text{loc}} = (0, 1)^\top$ are eigenspinors of σ^z . In the global frame the up and down spinors obey

$$+\chi_i^{\uparrow \text{gl}} = \mathbf{n}_i \cdot \boldsymbol{\sigma} \chi_i^{\uparrow \text{gl}}, \quad -\chi_i^{\downarrow \text{gl}} = \mathbf{n}_i \cdot \boldsymbol{\sigma} \chi_i^{\downarrow \text{gl}}. \quad (4.6)$$

They are eigenspinors of $\mathbf{n}_i \cdot \boldsymbol{\sigma}$, with the vector of Pauli matrices $\boldsymbol{\sigma}$. The components of these new eigenspinors are comprised in the matrix [112]

$$D(\varphi, \vartheta) = \begin{pmatrix} e^{-i\varphi/2} \cos(\vartheta/2) & -e^{-i\varphi/2} \sin(\vartheta/2) \\ e^{i\varphi/2} \sin(\vartheta/2) & e^{i\varphi/2} \cos(\vartheta/2) \end{pmatrix}, \quad \chi_i^{\text{gl}} = D(\varphi_i, \theta_i) \chi_i^{\text{loc}}. \quad (4.7)$$

It transforms a spinor from local into global frame. Its inverse $D^{-1} = D^\dagger$ transforms a spinor from global back into local frame.

The Hamiltonian and the eigenenergies as well as all observables are calculated within the global frame. Therein the z -axis is the SQA for the basis set of all atomic orbitals. Therefore the hopping elements stay unchanged in the global frame also in noncollinear structures.

However, the spin-split on-site energies apply to the local frame, in which the SQA is parallel to the z -axis of the local coordinate system and the on-site energies are diagonal with respect to spin. Therefore in the global frame of a noncollinear set-up the on-site energies can become spin-mixed. The on-site energy of an orbital α at site i is

$$\epsilon_\alpha = \langle \chi_\alpha^{\text{loc}} | \hat{E}_\alpha^{\text{loc}} | \chi_\alpha^{\text{loc}} \rangle = \langle \chi_\alpha^{\text{loc}} D_i^\dagger | D_i \hat{E}_\alpha^{\text{loc}} D_i^\dagger | D_i \chi_\alpha^{\text{loc}} \rangle = \langle \chi_\alpha^{\text{gl}} | \hat{E}_\alpha^{\text{gl}} | \chi_\alpha^{\text{gl}} \rangle \quad (4.8)$$

with according matrix representations

$$\mathbf{E}_\alpha^{\text{loc}} = \begin{pmatrix} E_\alpha^\uparrow & 0 \\ 0 & E_\alpha^\downarrow \end{pmatrix} \quad \text{and} \quad \mathbf{E}_\alpha^{\text{gl}} = D_i \mathbf{E}_\alpha^{\text{loc}} D_i^\dagger. \quad (4.9)$$

The latter one can be expressed as

$$\mathbf{E}_\alpha^{\text{gl}} = \begin{pmatrix} E + \Delta \cos(\theta_i) & \Delta e^{-i\varphi_i} \sin(\theta_i) \\ \Delta e^{i\varphi_i} \sin(\theta_i) & E - \Delta \cos(\theta_i) \end{pmatrix} \quad (4.10)$$

by means of spin-independent on-site energies and spin splitting

$$E = \frac{E_\alpha^\uparrow + E_\alpha^\downarrow}{2}, \quad \Delta = \frac{E_\alpha^\uparrow - E_\alpha^\downarrow}{2}. \quad (4.11)$$

For example in case of an SQA along the x -axis the spin-dependent energy splitting is completely contained in the off-diagonal elements. Whereas, if a site is aligned along the $-z$ -axis, there are no off-diagonal elements, instead the on-site energies change roles.

	1	2	3	4	5	6	7
δ	0°	0.5°	1°	3°	4.9°	9.7°	22°
M_0/M_0^{col} in %	100	99.996	99.99	99.9	99.74	99.0	95.6

Table 4.3.: Noncollinear configurations presented in Figures 4.34, 4.36 and 4.35: The average angle δ between two sites and the reduced initial magnetization.

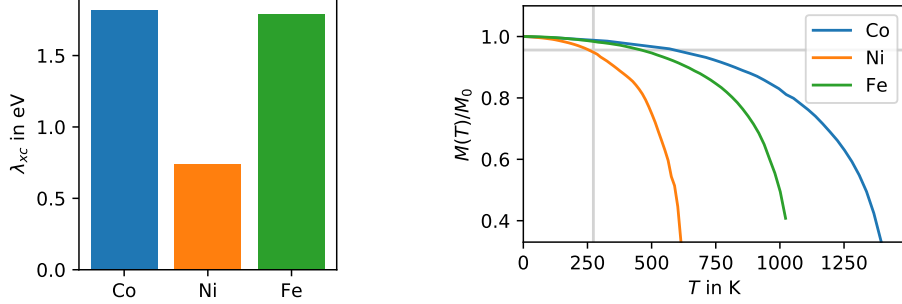


Figure 4.33.: For Co, Ni, and Fe it is shown on the left the exchange splitting within the on-site energies of d orbitals and on the right the temperature dependence of magnetization [115]. The room temperature and the reduced magnetization of Configuration 7 are indicated as grey lines.

To obtain a thermal configuration of SQAs the von Mises-Fisher distribution (Eq. (B.1) in the appendix) was used to generate a set of vectors on the unit sphere distributed randomly around the z -axis [113], [114]. This results in a reduced initial magnetization M_0/M_0^{coll} , the initial magnetization of the disordered configuration in comparison to that of the collinear alignment.

Table 4.3 gives for a specific set of SQAs the reduced initial magnetization in percentage of the collinear case, as well as the average angle δ between SQAs of two different sites. Simulation results can differ for small numbers of 20 to 40 randomly distributed vectors. Therefore results for different realizations of Configuration 7 are shown in the appendix in Figure B.5. Also a different arrangement of SQAs is calculated in form of a Co cluster with an alternative geometry (Table 4.4). These tests ensure that the chosen configuration and geometry are representative for the dynamics.

By comparing with experimental $M(T)$ curves, the reduced magnetization can be ascribed to an ambient temperature. However, this assignment is quite rough as the $M(T)$ curve is very flat in the regime of low temperatures. Figure 4.34 presents the exchange splitting and the $M(T)$ curves of Co, Ni, and Fe. The horizontal grey line indicates the reduced magnetization of Configuration 7, the set with the highest tilting. In case of Ni this configuration corresponds to room temperature, also indicated as a grey line. The exchange splittings of Co and Fe are more than twice as large as the one of Ni and a high magnetization survives up to higher

material	Co A	Co B	Ni A	Ni B	Fe
atoms	$2 \times (3 \times 2 \times 2)$	$2 \times (5 \times 2 \times 1)$	$2 \times (3 \times 2 \times 2)$	$2 \times (3 \times 2 \times 2)$	$3 \times 3 \times 3$
F in mJ/cm ²	13.1	13.1	14.1	3.5	13.2

Table 4.4.: For each ferromagnetic cluster of various size and material the extent in terms of lattice vectors is given as well as the applied fluence F.

temperatures. Therefore in Co and Fe Configuration 7 corresponds to significantly higher temperatures. But with respect to the Curie temperature Configuration 7 leads to a similar value of $T/T_C \approx 40$ % in all three materials.

In this way for each material and each set in Table 4.3 a temperature can be estimated. This temperature is based on the average tilting of the sites and therefore represents the temperature of the magnetic system in thermodynamic equilibrium. To completely represent this magnetic temperature of course the inter-site tilting should be dynamic. Note that within the following simulations all noncollinear configurations are static.

The assignment of a temperature to a specific set of SQAs and its reduced magnetization is very inaccurate. Therefore in the simulations the temperature of the heat bath and with it the initial electronic temperature are left at room temperature. In thermodynamic equilibrium the electronic temperature, the temperature of the heat bath and the magnetic temperature should coincide. However, the influence of the initial electronic temperature is negligible and the bath temperature only becomes important for remagnetization at very low temperatures. In this sense the following simulations show only the dependence on the magnetic temperature in terms of random static tilting, but should not differ to much from simulations of full temperature dependence in our framework.

In the following simulation results of noncollinear setups of cobalt, nickel and iron will be presented. Table 4.4 provides an overview of all simulated setups. In this section calculations are performed without the coupling to an external heat bath. Selected results of simulations with a heat bath are shown in the appendix. The laser parameters were chosen in order to achieve a comparable optical excitation in terms of the maximal number of excited electrons as shown in Figure 4.34 on the right. The corresponding fluences as well as the geometry of the respective cluster are listed in Table 4.4. In the fcc setups Co A and Ni A and in the bcc setup of Fe the degree of excitation coincides.

Figure 4.34 shows the demagnetization in the setup Co A for different noncollinear configurations. Table 4.3 lists the corresponding data. The demagnetization is clearly enhanced already for the smallest tilting of SQAs. In case of the collinear configuration of Co, depicted as a blue line, a demagnetization can not be calculated with our code, while Configuration 2 shows a tiny demagnetization of about 3 % upon optical excitation. By introducing a minute tilting of 0.5° between two neighbouring sites, this configuration is still almost collinear with an initial magnetization of 99.996 %

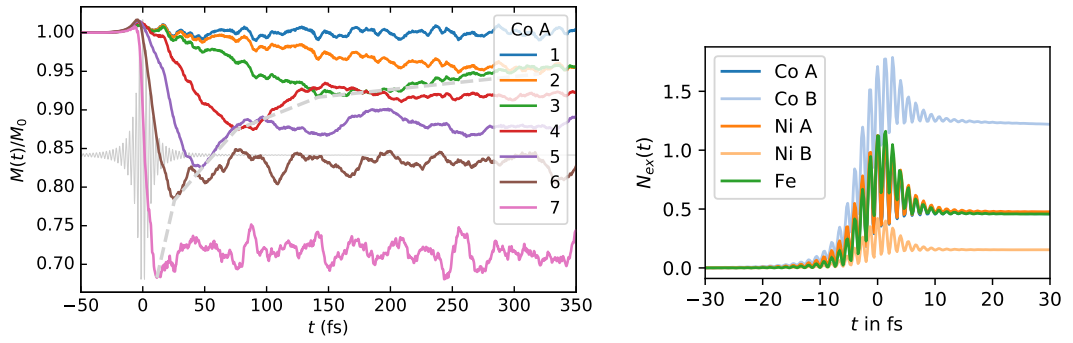


Figure 4.34.: The left graphic shows the enhancement of demagnetization by disordered alignment of initial SQAs in the cluster Co A. The time dependence of the laser pulse is indicated in grey. Likewise the position of minima is indicated by a dashed grey line. The right graphic shows the number of excited electrons within the collinear configuration for all setups listed in Table 4.4.

compared to the collinear setup. However, already a minute tilting introduces finite spin-mixed elements in the on-site energy (4.9) and thereby also the demagnetization is enhanced or even enabled. By introducing a higher inter-site tilting the demagnetization is enhanced further. But also the process of demagnetization is accelerated. This is visualized by a dashed grey line through the positions of minima. Finally for Configuration 7 with an angle of about 22° between two sites and a reduced initial magnetization of 95.6 % a demagnetization of almost 20 % is simulated, which is already comparable to experimental values. These results are verified by simulations of alternative realizations of Configuration 7 and of the alternative geometry Co B in B.5.

While the improvement of the simulation seems to work quite well for a Co cluster,

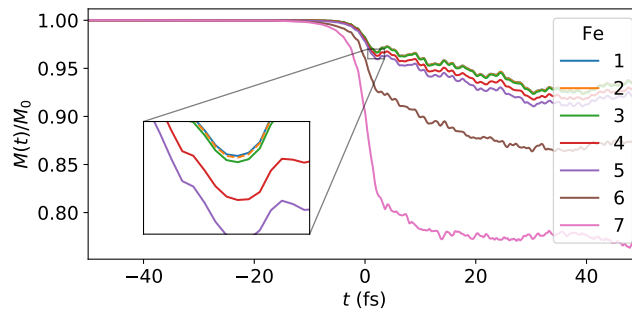


Figure 4.35.: Demagnetization in noncollinear configurations (see Table 4.3) of Fe after optical excitation.

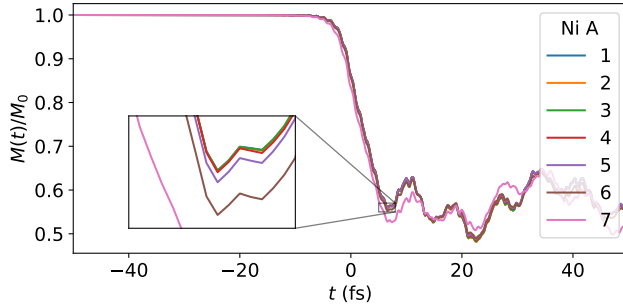


Figure 4.36.: Demagnetization in noncollinear configurations (see Table 4.3) of Ni after strong optical excitation (setup Ni A).

the results for Fe and Ni clusters are not so evident.

The setup for a bcc Fe lattice is a three-dimensional cluster of 27 atoms, three along the direction of each lattice vector. Figure 4.35 shows that also in case of Fe a remarkable enhancement of demagnetization can be achieved, from about 10 % up to almost 40 % for an inter-site angle of 22° . However, in case of small tiltings almost no changes are visible.

The Ni cluster, shown in Figure 4.36, exhibits already a very strong demagnetization without introducing any noncollinearity. Large tiltings add only slightly to the demagnetization of about 40 %. This also holds for smaller excitations (Ni B in B.4) just at a lower demagnetization.

The demagnetization in collinear configurations follows the strength of spin orbit coupling (Figure 4.23). Co with a small SOC shows only a faint demagnetization of less than 3 %. Fe already exhibits a demagnetization of 10 %, which goes up to 40 % in Ni. Furthermore the tilting induced spin-mixing elements in (4.10) are proportional to the exchange splitting $\Delta \sim \lambda_{xc}$. In Ni for small tiltings the SOC is larger and dominates the demagnetization. Only in Configurations 6 and 7 the spin-mixed elements (4.10) become comparably large or larger than the SOC and a difference in magnetization dynamics is visible. In case of Co and Fe with a large exchange splitting and a weaker SOC in almost all configurations the tilting induced spin-mixed elements exceed the spin-mixing by SOC and thus dominate demagnetization. In Fe this holds only for Configurations 5 to 7, while configurations with smaller tiltings lead to comparable magnitudes of SOC and tilting induced spin-mixed elements.

In summary, the influence of inter-site tilting on demagnetization depends on the ratio of SOC and exchange splitting. A minimal inter-site angle to observe an influence can be estimated as $\delta_{min} = \sin^{-1}(\lambda_{soc}/\lambda_{xc})$. This corresponds roughly to minimal angles of 1° in Co, 2° in Fe and 8° in Ni and is in good agreement with the above results. The dependence of demagnetization on inter-site tilting is stronger for materials with weak SOC and strong exchange splitting. If the static tilting is interpreted as an ambient temperature, the dependence of demagnetization on that ambient temperature is stronger for materials with weak SOC, while the influence

of λ_{xc} on the temperature dependence is smaller. Because on one hand a high exchange splitting increases the influence of the tilting, but on the other hand it tends to correspond to a higher Curie temperature and thus a weaker tilting at the same temperature.

The temperature dependence of Ni was investigated experimentally by Roth et al. [116]. At small temperatures almost no different demagnetization behavior could be observed. At room temperature the demagnetization is only slightly enhanced while it is enhanced significantly at higher temperatures. This is in good agreement with the above results calculated with the EVOLVE-code, but could not be reproduced as well by simulations based on a magnetic three-temperature-model [116] or the Boltzmann equation [20]. Both give very good results primarily in the higher temperature regime. Simulations presented in rt-TDDFT calculations using "initial magnetic disorder" [48] seem to show significant changes for angles bigger than 30° but also an enhancement of demagnetization from 15 % to 20 % between a zero temperature and a room temperature scenario.

4.4.3. Dynamical exchange splitting

Finally it shall be mentioned, that a so-called feedback effect is also discussed as an important mechanism of demagnetization. The implementation of a dynamical exchange splitting was tested and proposed in [20], [117]. The idea is to use a dynamical magnetization-dependent exchange splitting. If the magnetization is reduced by optical excitation, also the exchange splitting is reduced which in turn reduces the magnetization. Thus a feedback loop is unleashed which enhances the simulated demagnetization.

This effect can also be realized within our framework. Similar to (4.11) the Hamiltonian

$$H_0(t) = \begin{pmatrix} \tilde{H} - H_\Delta(t) & H_0^{\uparrow\downarrow} \\ H_0^{\downarrow\uparrow} & \tilde{H} + H_\Delta(t) \end{pmatrix} \quad (4.12)$$

is divided into a spin-independent and a spin-dependent part

$$\tilde{H} = \frac{1}{2}(H_0^{\uparrow\uparrow} + H_0^{\downarrow\downarrow}) \quad \text{and} \quad H_\Delta(t) = \frac{1}{2}(H_0^{\uparrow\uparrow} - H_0^{\downarrow\downarrow}) \cdot \lambda(t). \quad (4.13)$$

The latter one contains the exchange splitting and acquires a time dependence by the factor $\lambda(t)$. This factor introduces the feedback effect by scaling the energy splitting in dependence on the magnetization

$$\lambda(t) = f\left(\frac{M(t)}{M_0}\right) = \left(\frac{M(t)}{M_0}\right)^\alpha. \quad (4.14)$$

At the beginning of time evolution it is $\lambda = 1.0$. According to the above definitions H_0 and with it all eigenvalues and eigenvectors become time-dependent and have to be updated in every time step.

Included into the EVOLVE simulations this approach indeed yields a significant enhancement of demagnetization. With this also in pure ferromagnets realistic values

of demagnetization can be reached. However, the detailed results depend on the system and on the chosen function f . For example, in some setups $\alpha \geq 4$ is a necessary condition for the enhancement of demagnetization. In principle also dependencies other than (4.14) are possible [20], [117]. For some forms of f this approach introduces steps into the time evolution of demagnetization, which are probably unphysical artifacts. Beyond that the choice of the dependence is somewhat arbitrary. It seems that calculating a change of the electronic structure can more validly be achieved by *ab initio* calculations.

Based on the abovementioned reasons we did not pursue this approach further, although the mechanisms can be reproduced in our framework and can yield high demagnetizations.

5. Summary

Throughout the previous chapters a versatile approach to address ultrafast magnetization dynamics was presented. It is a real-space tight-binding model which treats optical excitation in terms of the electromagnetic dipole approximation. Coupling to an external heat bath simulates the exchange of energy with the environment. The time evolution of the system and the observables are studied by means of an occupation matrix. All this was implemented in the computational framework EVOLVE.

The functionality of the code was demonstrated using the example of a CoCu bilayer system. Upon optical excitation demagnetization was simulated and influences of the external bath, SOC, photon energy and polarization were analyzed. Detailed information about the underlying dynamics can be achieved by analyzing the system in the basis of atomic orbitals as well as in the eigenbasis.

Spin transport across the interface was studied on the basis of ultrafast spin currents. It was found to be the dominant contribution to demagnetization in the CoCu bilayer system. The breakdown of the spin current into contributions from individual orbitals reveals the underlying mechanisms: a current of minority carriers from Cu into Co. An analysis of material combinations shows however a diverse behavior with dominant majority currents in other cases. Throughout all material combinations demagnetization was favored by a high SOC.

Spin transport was also studied in inhomogeneously excited systems without an interface. Its contribution to demagnetization was significant and its magnitude comparable to that of spin currents generated at an interface. The extension of the code to noncollinear magnetism allows a better simulation of homogeneous ferromagnetic materials. Especially in case of weaker spin orbit couplings the spin transport due to a gradient in excitation and finite tilting are important contributions to demagnetization and should be taken into account.

The presented approach EVOLVE can easily be modified to include new mechanisms. The observed mechanism depends on the exact parametrization. This is not a disadvantage. Instead, underlying mechanisms can be revealed clearly due to the ability to flexibly manipulate the corresponding parameters. EVOLVE can treat large inhomogeneous systems and offers access to microscopic processes. The present approach may be improved by including electron-electron interaction to prevent unphysical charge imbalance. Furthermore the interaction with the external bath can be realized with energy-dependent scattering rates based on *ab initio* calculations.

EVOLVE offers plenty opportunities for further investigation. Ongoing works consider for example spin polarization and spin currents beyond the two current model as well as orbital polarization and orbital currents [118], [119].

A. Additional derivations

A.1. Influence of the envelope function

The vector potential (already without local dependence) of a laser pulse is

$$\mathbf{A}(t) = A_0 \boldsymbol{\epsilon} \sin(\omega t) \exp\left(-\frac{2(t-t_0)^2}{\tau^2}\right). \quad (\text{A.1})$$

Its derivative is

$$-\mathbf{E}(t) = \frac{\partial}{\partial t} \mathbf{A}(t) = A_0 \boldsymbol{\epsilon} \exp\left(-\frac{2(t-t_0)^2}{\tau^2}\right) \left(\omega \cos(\omega t) - 4 \sin(\omega t) \frac{t-t_0}{\tau^2} \right). \quad (\text{A.2})$$

The second term inside the bracket results from deriving the Gaussian envelope function. To estimate its influence, the full expression is compared with a reduced version of $\mathbf{E}(t)$, which does not include the second term.

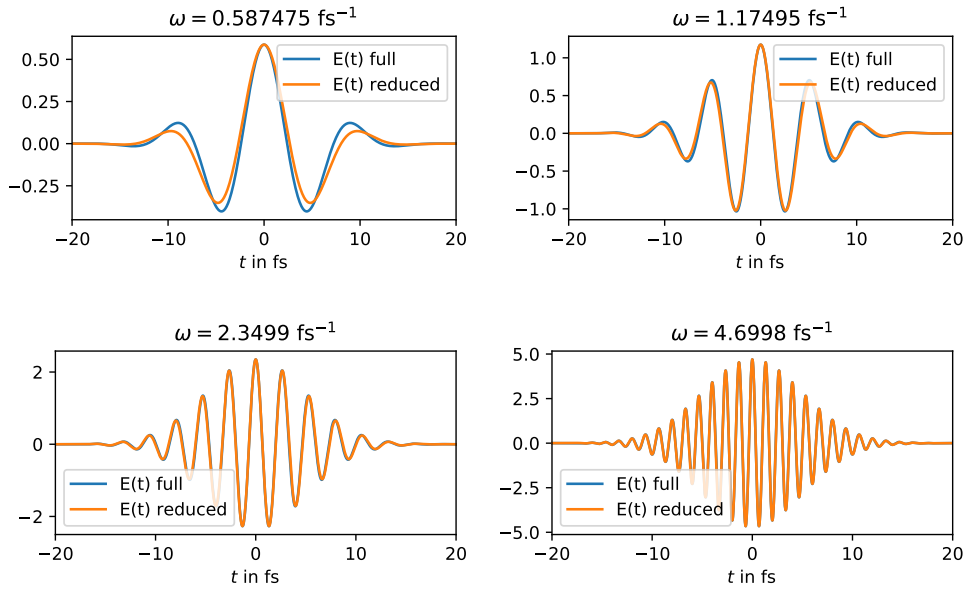


Figure A.1.: Full and reduced expression of the electric field of the laser pulse.

The left illustration in the bottom of Figure A.1 shows the usual configuration with $\tau = 10$ fs and $\omega = 2\pi \cdot 0.374\text{fs}^{-1}$, with almost no visible deviation. The neglected term becomes only important if the frequency is too low compared with the pulse width, as can be seen in the top row. Therefore it is justified to neglect the derivative of the envelope function in (2.25) if configurations are restricted to those with a sufficiently broad pulse width.

A.2. Modifying the Redfield equation

All terms within the Redfield equation (3.41) are written explicitly by expanding the commutators

$$\begin{aligned} \frac{d}{dt}\hat{\rho}(t) = & -\alpha^2 \text{tr}_{\text{B}} \int_0^\infty ds \left(\hat{\text{H}}_{\text{I}}(t)\hat{\text{H}}_{\text{I}}(t-s)\hat{\rho}(t) \otimes \hat{\rho}_{\text{B}}(0) - \hat{\text{H}}_{\text{I}}(t)\hat{\rho}(t) \otimes \hat{\rho}_{\text{B}}(0)\hat{\text{H}}_{\text{I}}(t-s) \right. \\ & \left. - \hat{\text{H}}_{\text{I}}(t-s)\hat{\rho}(t) \otimes \hat{\rho}_{\text{B}}(0)\hat{\text{H}}_{\text{I}}(t) + \hat{\rho}(t) \otimes \hat{\rho}_{\text{B}}(0)\hat{\text{H}}_{\text{I}}(t-s)\hat{\text{H}}_{\text{I}}(t) \right). \end{aligned} \quad (\text{A.3})$$

The decomposition into the eigenoperators $\hat{\text{S}}_i(\omega)$ is used to rewrite the interaction Hamiltonians in one of the two forms

$$\hat{\text{H}}_{\text{I}}(t) = \sum_{i,\omega} e^{+i\omega t} \hat{\text{S}}_i^\dagger(\omega) \otimes \hat{\text{B}}_i^\dagger(t) = \sum_{i,\omega} e^{-i\omega t} \hat{\text{S}}_i(\omega) \otimes \hat{\text{B}}_i(t). \quad (\text{A.4})$$

In the first and third term of (A.3) we replace

$$\hat{\text{H}}_{\text{I}}(t) = \sum_{i,\omega'} e^{+i\omega' t} \hat{\text{S}}_i^\dagger(\omega') \otimes \hat{\text{B}}_i^\dagger(t) \quad \text{and} \quad \hat{\text{H}}_{\text{I}}(t-s) = \sum_{j,\omega} e^{-i\omega(t-s)} \hat{\text{S}}_j(\omega) \otimes \hat{\text{B}}_j(t-s) \quad (\text{A.5})$$

and in the second and fourth term we set

$$\hat{\text{H}}_{\text{I}}(t) = \sum_{j,\omega'} e^{+i\omega' t} \hat{\text{S}}_j(\omega') \otimes \hat{\text{B}}_j(t) \quad \text{and} \quad \hat{\text{H}}_{\text{I}}(t-s) = \sum_{i,\omega} e^{+i\omega(t-s)} \hat{\text{S}}_i^\dagger(\omega) \otimes \hat{\text{B}}_i^\dagger(t-s). \quad (\text{A.6})$$

Inserting the introduced decompositions into (A.3) leads to

$$\begin{aligned} \frac{d}{dt}\hat{\rho}(t) = & -\alpha^2 \sum_{\substack{i,j \\ \omega,\omega'}} \text{tr}_{\text{B}} \int_0^\infty ds \\ & \left(e^{+i\omega' t} \hat{\text{S}}_i^\dagger(\omega') \otimes \hat{\text{B}}_i^\dagger(t) e^{-i\omega(t-s)} \hat{\text{S}}_j(\omega) \otimes \hat{\text{B}}_j(t-s) \hat{\rho}(t) \otimes \hat{\rho}_{\text{B}}(0) \right. \\ & - e^{-i\omega' t} \hat{\text{S}}_j(\omega') \otimes \hat{\text{B}}_j(t) \hat{\rho}(t) \otimes \hat{\rho}_{\text{B}}(0) e^{+i\omega(t-s)} \hat{\text{S}}_i^\dagger(\omega) \otimes \hat{\text{B}}_i^\dagger(t-s) \\ & - e^{-i\omega(t-s)} \hat{\text{S}}_j(\omega) \otimes \hat{\text{B}}_j(t-s) \hat{\rho}(t) \otimes \hat{\rho}_{\text{B}}(0) e^{+i\omega' t} \hat{\text{S}}_i^\dagger(\omega') \otimes \hat{\text{B}}_i^\dagger(t) \\ & \left. + \hat{\rho}(t) \otimes \hat{\rho}_{\text{B}}(0) e^{+i\omega(t-s)} \hat{\text{S}}_i^\dagger(\omega) \otimes \hat{\text{B}}_i^\dagger(t-s) e^{-i\omega' t} \hat{\text{S}}_j(\omega') \otimes \hat{\text{B}}_j(t) \right). \end{aligned} \quad (\text{A.7})$$

By exploiting the invariance of cyclic permutation under the trace the factor Γ_{ij} defined in (3.47) can be separated from the system dynamics.

B. Additional results

B.1. Polarization dependence

Similar features are visible in the polarization dependence of the total number of excited electrons as observed for the demagnetization in the Co layer.

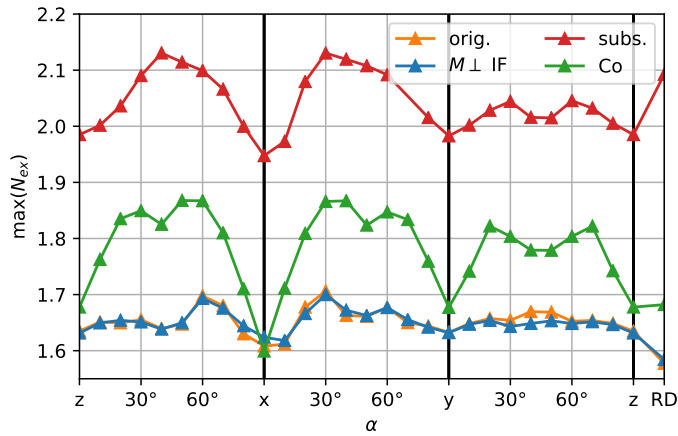


Figure B.1.: The dependence of the number of excited electrons on the laser polarization is shown as the demagnetization of the three-dimensional cluster in Figure 4.14.

B.2. Frequency dependence

Also for an alternative geometry of the CoCu cluster a comparable demagnetization was simulated for three different photon energies.

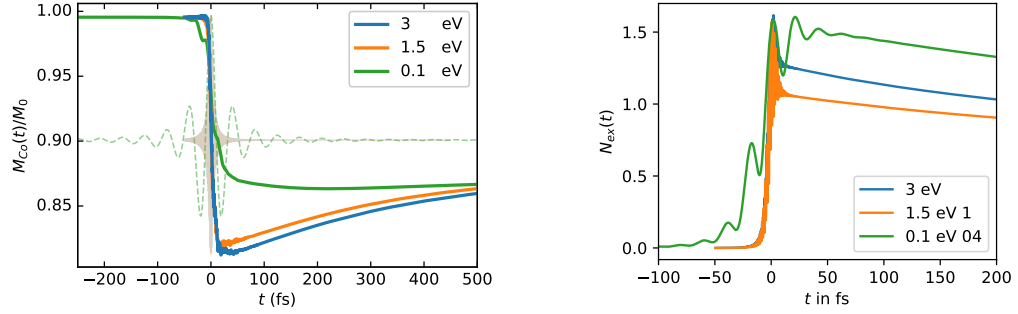


Figure B.2.: The results of Figure 4.17 calculated for a three-dimensional system of 16 Co and 16 Cu atoms. The left panel shows the demagnetization of the Co layer in a 2D CoCu cluster excited by laser light with different frequencies. The laser pulses of different frequencies are indicated as thin dashed lines. The right panel presents the corresponding number of excited electrons.

B.3. Interface currents

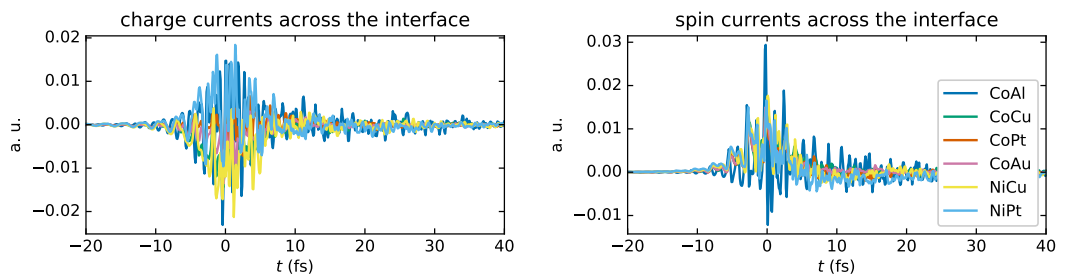


Figure B.3.: Charge and spin currents across the interface from the ferromagnetic into the nonmagnetic layer.

B.4. Noncollinear setups

The von Mises-Fisher probability density function for a random vector \mathbf{x} on the unit sphere is defined as [114]

$$f(\mathbf{x}; \kappa) = \left(\frac{\kappa}{2}\right)^{0.5} \frac{1}{\Gamma(1.5)I_{0.5}(\kappa)} \exp(\kappa \mathbf{e}_z^T \mathbf{x}) . \quad (\text{B.1})$$

$I_a(\kappa)$ are the modified Bessel functions. The resulting vectors are distributed with the concentration parameter κ around \mathbf{e}_z . A low value of κ corresponds to a low expectation value $\langle \mathcal{S}_z \rangle$.

Figure B.5 confirms the results of Section 4.4.2. The simulations presented in Figure 4.34 are recalculated with a coupling to a heat bath, and additionally for a different shape of the two-dimensional Co cluster, labeled Co B in Table 4.4. In both cases the behavior as shown in Figure 4.34 is repeated. With the coupling to a heat bath the strong oscillations of magnetization after the optical excitation vanish, but the degree of demagnetization remains unchanged. In case of the alternative setup, Co B, also the completely collinear configuration exhibits a small demagnetization. Apart from this the enhancement of demagnetization by increasing the tilting of SQAs is completely equivalent to the setup Co A. Different realizations of Configuration 7 exhibit a similar qualitative behavior.

In agreement to Figure 4.36 simulations of weakly excited Ni show an influence only for large initial tiltings.

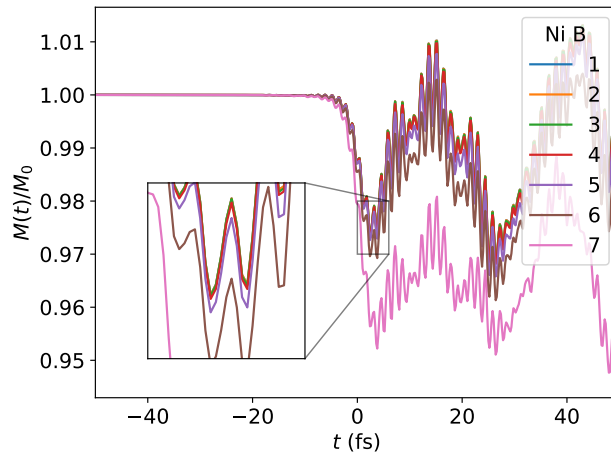


Figure B.4.: The simulations of Figure 4.36 are repeated with a weak excitation (setup Ni B in Table 4.4).

[120]

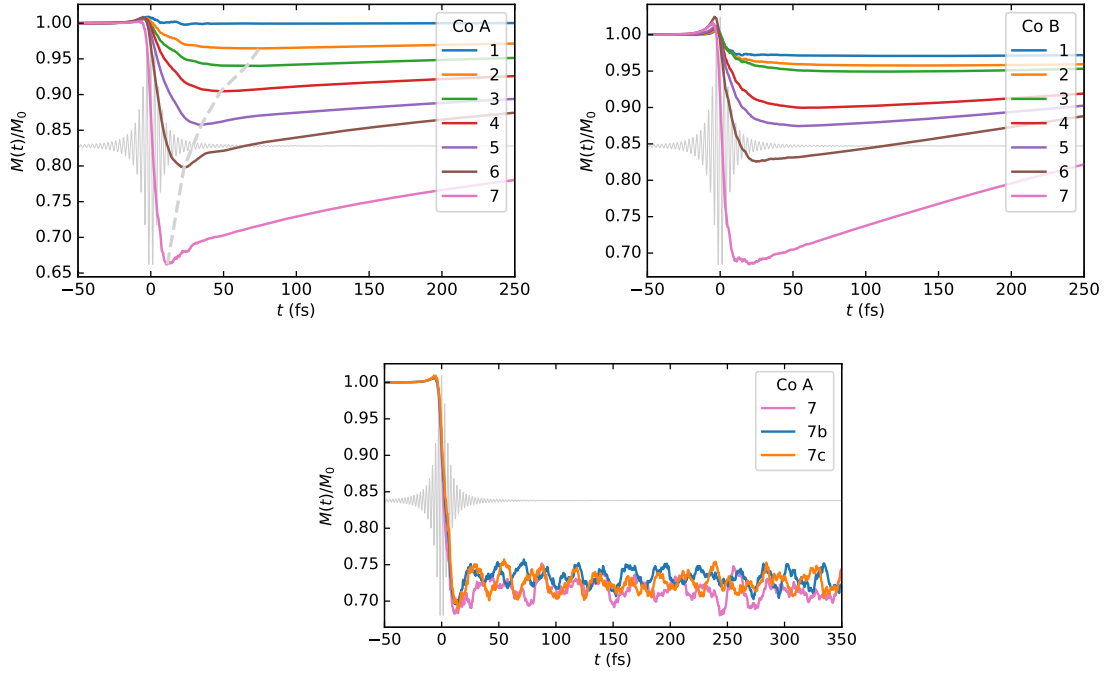


Figure B.5.: Demagnetization in Co clusters with a finite inter-site tilting as presented in Figure 4.34, but with coupling to an external heat bath. On the left the calculations of the setup Co A are repeated. On the right results for an alternative geometry of Co atoms (setup Co B) are shown. The numbers refer to noncollinear configurations specified in Table 4.3. In the bottom row different realizations of Configuration 7 in the Co A cluster are compared without coupling to a heat bath.

Bibliography

- [1] J. Heidmann and A. Taratorin, “Magnetic Recording Heads”, en, in *Handbook of Magnetic Materials*, vol. 19, Elsevier, 2011, pp. 12–42.
- [2] H. W. Schumacher, C. Chappert, R. C. Sousa, P. P. Freitas, and J. Miltat, “Quasiballistic Magnetization Reversal”, en, *Phys. Rev. Lett.*, vol. 90, no. 1, p. 017 204, Jan. 2003.
- [3] H. W. Schumacher, C. Chappert, R. C. Sousa, and P. P. Freitas, “Current-induced precessional magnetization reversal”, en, *Applied Physics Letters*, vol. 83, no. 11, pp. 2205–2207, Sep. 2003.
- [4] E. Beaurepaire, J.-C. Merle, A. Daunois, and J.-Y. Bigot, “Ultrafast Spin Dynamics in Ferromagnetic Nickel”, en, *Physical Review Letters*, vol. 76, no. 22, pp. 4250–4253, May 1996.
- [5] I. Radu, K. Vahaplar, C. Stamm, T. Kachel, N. Pontius, H. A. Dürr, T. A. Ostler, J. Barker, R. F. L. Evans, R. W. Chantrell, A. Tsukamoto, A. Itoh, A. Kirilyuk, T. Rasing, and A. V. Kimel, “Transient ferromagnetic-like state mediating ultrafast reversal of antiferromagnetically coupled spins”, en, *Nature*, vol. 472, no. 7342, pp. 205–208, Apr. 2011.
- [6] J. Gorchon, C.-H. Lambert, Y. Yang, A. Patabi, R. B. Wilson, S. Salahuddin, and J. Bokor, “Single shot ultrafast all optical magnetization switching of ferromagnetic Co/Pt multilayers”, en, *Appl. Phys. Lett.*, vol. 111, no. 4, p. 042 401, Jul. 2017.
- [7] A. Alekhin, I. Razdolski, N. Ilin, J. P. Meyburg, D. Diesing, V. Roddatis, I. Rungger, M. Stamenova, S. Sanvito, U. Bovensiepen, and A. Melnikov, “Femtosecond Spin Current Pulses Generated by the Nonthermal Spin-Dependent Seebeck Effect and Interacting with Ferromagnets in Spin Valves”, *Phys. Rev. Lett.*, vol. 119, no. 1, 2017.
- [8] T. Kampfrath, M. Battiato, P. Maldonado, G. Eilers, J. Nötzold, S. Mährlein, V. Zbarsky, F. Freimuth, Y. Mokrousov, S. Blügel, M. Wolf, I. Radu, P. M. Oppeneer, and M. Münzenberg, “Terahertz spin current pulses controlled by magnetic heterostructures”, en, *Nature Nanotechnology*, vol. 8, no. 4, pp. 256–260, Apr. 2013.

- [9] T. Seifert, S. Jaiswal, U. Martens, J. Hannegan, L. Braun, P. Maldonado, F. Freimuth, A. Kronenberg, J. Henrizi, I. Radu, E. Beaupaire, Y. Mokrousov, P. M. Oppeneer, M. Jourdan, G. Jakob, D. Turchinovich, L. M. Hayden, M. Wolf, M. Münzenberg, M. Kläui, and T. Kampfrath, “Efficient metallic spintronic emitters of ultrabroadband terahertz radiation”, en, *Nature Photonics*, vol. 10, no. 7, pp. 483–488, Jul. 2016.
- [10] T. S. Seifert, S. Jaiswal, J. Barker, S. T. Weber, I. Razdolski, J. Cramer, O. Gueckstock, S. F. Maehrlein, L. Nadvornik, S. Watanabe, C. Ciccarelli, A. Melnikov, G. Jakob, M. Münzenberg, S. T. B. Goennenwein, G. Woltersdorf, B. Rethfeld, P. W. Brouwer, M. Wolf, M. Kläui, and T. Kampfrath, “Femtosecond formation dynamics of the spin Seebeck effect revealed by terahertz spectroscopy”, en, *Nature Communications*, vol. 9, no. 1, Dec. 2018.
- [11] U. Nandi, M. S. Abdelaziz, S. Jaiswal, G. Jakob, O. Gueckstock, S. M. Rouze-gar, T. S. Seifert, M. Kläui, T. Kampfrath, and S. Preu, “Antenna-coupled spintronic terahertz emitters driven by a 1550 nm femtosecond laser oscillator”, en, *Applied Physics Letters*, vol. 115, no. 2, p. 022405, Jul. 2019.
- [12] G. Torosyan, S. Keller, L. Scheuer, R. Beigang, and E. T. Papaioannou, “Optimized Spintronic Terahertz Emitters Based on Epitaxial Grown Fe/Pt Layer Structures”, en, *Scientific Reports*, vol. 8, no. 1, Dec. 2018.
- [13] K. Carva, P. Baláž, and I. Radu, “Laser-Induced Ultrafast Magnetic Phenomena”, en, in *Handbook of Magnetic Materials*, vol. 26, Elsevier, 2017, pp. 291–463.
- [14] B. Y. Mueller and B. Rethfeld, “Relaxation dynamics in laser-excited metals under nonequilibrium conditions”, en, *Physical Review B*, vol. 87, no. 3, Jan. 2013.
- [15] L. Willig, “Ultraschnelle Magneto-Optische Studien der Remagnetisierungsdynamik von Übergangsmetallen Ultrafast magneto-optical studies of remagnetisation dynamics in transition metals”, en, PhD thesis, Universität Potsdam, 2020.
- [16] J. Wiczorek, A. Eschenlohr, B. Weidtmann, M. Rösner, N. Berggard, A. Tarasevitch, T. O. Wehling, and U. Bovensiepen, “Separation of ultrafast spin currents and spin-flip scattering in Co/Cu(001) driven by femtosecond laser excitation employing the complex magneto-optical Kerr effect”, en, *Physical Review B*, vol. 92, no. 17, Nov. 2015.
- [17] V. Shokeen, M. Sanchez Piaia, J.-Y. Bigot, T. Müller, P. Elliott, J. K. Dewhurst, S. Sharma, and E. K. U. Gross, “Spin Flips versus Spin Transport in Nonthermal Electrons Excited by Ultrashort Optical Pulses in Transition Metals”, en, *Physical Review Letters*, vol. 119, no. 10, Sep. 2017.

- [18] S. Eich, M. Plötzing, M. Rollinger, S. Emmerich, R. Adam, C. Chen, H. Kapteyn, M. M. Murnane, L. Plucinski, D. Steil, B. Stadtmüller, M. Cinchetti, M. Aeschlimann, C. M. Schneider, and S. Mathias, “Band structure evolution during the ultrafast ferromagnetic-paramagnetic phase transition in cobalt”, en, *Sci. Adv.*, vol. 3, no. 3, e1602094, Mar. 2017.
- [19] E. Turgut, D. Zusin, D. Legut, K. Carva, R. Knut, J. M. Shaw, C. Chen, Z. Tao, H. T. Nembach, T. J. Silva, S. Mathias, M. Aeschlimann, P. M. Oppeneer, H. C. Kapteyn, M. M. Murnane, and P. Grychtol, “Stoner versus Heisenberg: Ultrafast exchange reduction and magnon generation during laser-induced demagnetization”, en, *Phys. Rev. B*, vol. 94, no. 22, p. 220 408, Dec. 2016.
- [20] B. Y. Mueller, A. Baral, S. Vollmar, M. Cinchetti, M. Aeschlimann, H. C. Schneider, and B. Rethfeld, “Feedback Effect during Ultrafast Demagnetization Dynamics in Ferromagnets”, en, *Physical Review Letters*, vol. 111, no. 16, Oct. 2013.
- [21] W. Töws and G. M. Pastor, “Many-Body Theory of Ultrafast Demagnetization and Angular Momentum Transfer in Ferromagnetic Transition Metals”, en, *Physical Review Letters*, vol. 115, no. 21, Nov. 2015.
- [22] J. K. Dewhurst, P. Elliott, S. Shallcross, E. K. U. Gross, and S. Sharma, “Laser-Induced Intersite Spin Transfer”, *Nano Lett.*, vol. 18, no. 3, pp. 1842–1848, 2018.
- [23] F. Töpler, J. Henk, and I. Mertig, “Ultrafast spin dynamics in inhomogeneous systems: A density-matrix approach applied to Co/Cu interfaces”, *New J. Phys.*, vol. 23, no. 3, p. 033 042, Mar. 2021.
- [24] B. Koopmans, J. J. M. Ruigrok, F. D. Longa, and W. J. M. de Jonge, “Unifying Ultrafast Magnetization Dynamics”, en, *Phys. Rev. Lett.*, vol. 95, no. 26, p. 267 207, Dec. 2005.
- [25] B. Y. Mueller, T. Roth, M. Cinchetti, M. Aeschlimann, and B. Rethfeld, “Driving force of ultrafast magnetization dynamics”, *New Journal of Physics*, vol. 13, no. 12, p. 123 010, Dec. 2011.
- [26] E. Carpene, E. Mancini, C. Dallera, M. Brenna, E. Puppini, and S. De Silvestri, “Dynamics of electron-magnon interaction and ultrafast demagnetization in thin iron films”, en, *Phys. Rev. B*, vol. 78, no. 17, p. 174 422, Nov. 2008.
- [27] A. B. Schmidt, M. Pickel, M. Donath, P. Buczek, A. Ernst, V. P. Zhukov, P. M. Echenique, L. M. Sandratskii, E. V. Chulkov, and M. Weinelt, “Ultrafast Magnon Generation in an Fe Film on Cu(100)”, en, *Phys. Rev. Lett.*, vol. 105, no. 19, p. 197 401, Nov. 2010.
- [28] U. Ritzmann, P. Baláž, P. Maldonado, K. Carva, and P. M. Oppeneer, “High-frequency magnon excitation due to femtosecond spin-transfer torques”, en, *Phys. Rev. B*, vol. 101, no. 17, p. 174 427, May 2020.

- [29] B. Koopmans, G. Malinowski, F. Dalla Longa, D. Steiauf, M. Fähnle, T. Roth, M. Cinchetti, and M. Aeschlimann, “Explaining the paradoxical diversity of ultrafast laser-induced demagnetization”, en, *Nature Materials*, vol. 9, no. 3, pp. 259–265, Mar. 2010.
- [30] D. M. Nenko, B. Rethfeld, and H. C. Schneider, “Particle-in-cell simulation of ultrafast hot-carrier transport in Fe/Au heterostructures”, *Phys. Rev. B*, vol. 98, no. 22, p. 224416, 2018.
- [31] S. Kaltenborn, Y.-H. Zhu, and H. Schneider, “Wave-diffusion theory of spin transport in metals after ultrashort-pulse excitation”, en, *Physical Review B*, vol. 85, no. 23, Jun. 2012.
- [32] M. Battiato, K. Carva, and P. M. Oppeneer, “Superdiffusive Spin Transport as a Mechanism of Ultrafast Demagnetization”, *Phys. Rev. Lett.*, vol. 105, no. 2, 2010.
- [33] M. Battiato, “Superdiffusive Spin Transport and Ultrafast Magnetization Dynamics: Femtosecond spin transport as the route to ultrafast spintronics”, OCLC: 940636548, PhD thesis, University Uppsala, Uppsala, 2013.
- [34] K. Krieger, J. K. Dewhurst, P. Elliott, S. Sharma, and E. K. U. Gross, “Laser-Induced Demagnetization at Ultrashort Time Scales: Predictions of TDDFT”, en, *Journal of Chemical Theory and Computation*, vol. 11, no. 10, pp. 4870–4874, Oct. 2015.
- [35] W. Töws and G. M. Pastor, “Tuning the laser-induced ultrafast demagnetization of transition metals”, en, *Physical Review B*, vol. 100, no. 2, Jul. 2019.
- [36] J. C. Slater and G. F. Koster, “Simplified LCAO Method for the Periodic Potential Problem”, en, *Physical Review*, vol. 94, no. 6, pp. 1498–1524, Jun. 1954.
- [37] J. C. Slater, “Atomic shielding constants”, *Phys. Rev.*, vol. 36, pp. 57–64, 1 Jul. 1930.
- [38] K. Takegahara, Y. Aoki, and A. Yanase, “Slater-Koster tables for f electrons”, *J. Phys. C: Solid State Phys.*, vol. 13, no. 4, pp. 583–588, Feb. 1980.
- [39] A. Nussbaum, “Crystal Symmetry, Group Theory, and Band Structure Calculations”, en, in *Solid State Physics*, vol. 18, Elsevier, 1966, pp. 165–272.
- [40] D. A. Papaconstantopoulos, *Handbook of the Band Structure of Elemental Solids*, en. Boston, MA: Springer US, 2015.
- [41] M. Jaffe and J. Singh, “Inclusion of spin-orbit coupling into tight binding bandstructure calculations for bulk and superlattice semiconductors”, en, *Solid State Communications*, vol. 62, no. 6, pp. 399–402, May 1987.
- [42] M. D. Jones and R. C. Albers, “Spin-orbit coupling in an f -electron tight-binding model: Electronic properties of Th, U, and Pu”, en, *Phys. Rev. B*, vol. 79, no. 4, p. 045107, Jan. 2009.

- [43] C. Cohen-Tannoudji, B. Diu, C. Henkel, F. Laloë, J. Streubel, J. Balla, and K. Lippert, *Quantenmechanik : Band 2 / Claude Cohen-Tannoudji, Bernard Diu, Franck Laloë*. Jan. 2019.
- [44] W. Greiner and J. Dreitlein, “Quantum Mechanics: An Introduction”, *American Journal of Physics*, vol. 58, no. 12, pp. 1217–1218, 1990, Publisher: American Association of Physics Teachers.
- [45] R. Peierls, “Zur Theorie des Diamagnetismus von Leitungselektronen”, de, *Z. Physik*, vol. 80, no. 11-12, pp. 763–791, Nov. 1933.
- [46] J. M. Luttinger, “The Effect of a Magnetic Field on Electrons in a Periodic Potential”, en, *Phys. Rev.*, vol. 84, no. 4, pp. 814–817, Nov. 1951.
- [47] P. van der Straten and H. Metcalf, *Atoms and Molecules Interacting with Light: Atomic Physics for the Laser Era*. Cambridge: Cambridge University Press, 2016.
- [48] Z. Chen and L.-W. Wang, “Role of initial magnetic disorder: A time-dependent ab initio study of ultrafast demagnetization mechanisms”, en, *Sci. Adv.*, vol. 5, no. 6, eaau8000, Jun. 2019.
- [49] S. Savasta and R. Girlanda, “The particle-photon interaction in systems described by model Hamiltonians in second quantization”, en, *Solid State Communications*, vol. 96, no. 7, pp. 517–522, Nov. 1995.
- [50] W. H. Louisell, *Quantum statistical properties of radiation*. John Wiley and Sons, Inc., New York, 1973.
- [51] J. Henk, T. Scheunemann, S. V. Halilov, and R. Feder, “Magnetic dichroism and electron spin polarization in photoemission: Analytical results”, *Journal of Physics: Condensed Matter*, vol. 8, no. 1, p. 47, Jan. 1996.
- [52] J. A. Gaunt, “IV. The triplets of helium”, en, *Phil. Trans. R. Soc. Lond. A*, vol. 228, no. 659-669, pp. 151–196, Jan. 1929.
- [53] E. J. Weniger and E. O. Steinborn, “Programs for the coupling of spherical harmonics”, en, *Computer Physics Communications*, vol. 25, no. 2, pp. 149–157, Feb. 1982.
- [54] M. W. Sigrist, *Laser: Theorie, Typen und Anwendungen*. Springer, 2018.
- [55] G. D. Mahan, *Many-Particle Physics*. Boston, MA: Springer US, 2000.
- [56] R. Citro and F. Mancini, *Out-of-Equilibrium Physics of Correlated Electron Systems*. Springer, 2018.
- [57] M. A. Schlosshauer, *Decoherence: and the quantum-to-classical transition*. Springer Science & Business Media, 2007.
- [58] E. P. Wigner, “On the Quantum Correction for Thermodynamic Equilibrium”, en, in *Part I: Physical Chemistry. Part II: Solid State Physics*, A. S. Wightman, Ed., Berlin, Heidelberg: Springer Berlin Heidelberg, 1997, pp. 110–120.

- [59] J. v. Neumann, “Wahrscheinlichkeitstheoretischer Aufbau der Quantenmechanik”, *Nachrichten von der Gesellschaft der Wissenschaften zu Göttingen, Mathematisch-Physikalische Klasse*, vol. 1927, pp. 245–272, 1927.
- [60] L. Landau, “The damping problem in wave mechanics”, *Z. Phys*, vol. 45, no. 63, pp. 430–441, 1927.
- [61] Y. V. Pershin, Y. Dubi, and M. Di Ventra, “Effective single-particle order-N scheme for the dynamics of open noninteracting many-body systems”, en, *Physical Review B*, vol. 78, no. 5, Aug. 2008.
- [62] A. J. Coleman, “Structure of Fermion Density Matrices”, en, *Rev. Mod. Phys.*, vol. 35, no. 3, pp. 668–686, Jul. 1963.
- [63] K. Head-Marsden and D. A. Mazziotti, “Satisfying fermionic statistics in the modeling of non-Markovian dynamics with one-electron reduced density matrices”, en, *The Journal of Chemical Physics*, vol. 151, no. 3, p. 034111, Jul. 2019.
- [64] R. Chakraborty and D. A. Mazziotti, “Noise-assisted energy transfer from the dilation of the set of one-electron reduced density matrices”, en, *The Journal of Chemical Physics*, vol. 146, no. 18, p. 184101, May 2017.
- [65] H.-P. Breuer and F. Petruccione, *The theory of open quantum systems*. Oxford ; New York: Oxford University Press, 2002, OCLC: ocm49872077.
- [66] J. Von Neumann, “Thermodynamik quantenmechanischer gesamtheiten”, *Nachrichten von der Gesellschaft der Wissenschaften zu Göttingen, Mathematisch-Physikalische Klasse*, vol. 1927, pp. 273–291, 1927.
- [67] A. Uhlmann, “The “transition probability” in the state space of a \ast -algebra”, en, *Reports on Mathematical Physics*, vol. 9, no. 2, pp. 273–279, Apr. 1976.
- [68] S. Barnett, *Quantum information*. Oxford University Press, 2009, vol. 16.
- [69] H.-S. Rhie, H. A. Dürr, and W. Eberhardt, “Femtosecond Electron and Spin Dynamics in Ni / W (110) Films”, en, *Physical Review Letters*, vol. 90, no. 24, Jun. 2003.
- [70] S. Nakajima, “On Quantum Theory of Transport Phenomena: Steady Diffusion”, en, *Prog. Theor. Phys.*, vol. 20, no. 6, pp. 948–959, Dec. 1958.
- [71] R. Zwanzig, “Ensemble Method in the Theory of Irreversibility”, en, *The Journal of Chemical Physics*, vol. 33, no. 5, pp. 1338–1341, Nov. 1960.
- [72] A. Kossakowski, “On quantum statistical mechanics of non-Hamiltonian systems”, en, *Reports on Mathematical Physics*, vol. 3, no. 4, pp. 247–274, Dec. 1972.
- [73] G. Lindblad, “On the generators of quantum dynamical semigroups”, en, *Communications in Mathematical Physics*, vol. 48, no. 2, pp. 119–130, Jun. 1976.
- [74] V. Gorini, A. Kossakowski, and E. C. G. Sudarshan, “Completely positive dynamical semigroups of N-level systems”, en, *Journal of Mathematical Physics*, vol. 17, no. 5, p. 821, 1976.

- [75] D. Manzano, “A short introduction to the Lindblad master equation”, en, *AIP Advances*, vol. 10, no. 2, p. 025 106, Feb. 2020.
- [76] R. Alicki, “Invitation to Quantum Dynamical Semigroups”, in *Dynamics of Dissipation*, R. Beig, B. -G. Englert, U. Frisch, P. Hänggi, K. Hepp, W. Hillebrandt, D. Imboden, R. L. Jaffe, R. Lipowsky, H. v. Löhneysen, I. Ojima, D. Sornette, S. Theisen, W. Weise, J. Wess, J. Zittartz, P. Garbaczewski, and R. Olkiewicz, Eds., vol. 597, Series Title: Lecture Notes in Physics, Berlin, Heidelberg: Springer Berlin Heidelberg, 2002, pp. 239–264.
- [77] P. Pearle, “Simple derivation of the Lindblad equation”, *European Journal of Physics*, vol. 33, no. 4, pp. 805–822, Jul. 2012.
- [78] R. Alicki and K. Lendi, *Quantum dynamical semigroups and applications*, ser. Lecture notes in physics 717. Berlin ; New York: Springer-Verlag, 2007.
- [79] M.-D. Choi, “Completely positive linear maps on complex matrices”, en, *Linear Algebra and its Applications*, vol. 10, no. 3, pp. 285–290, Jun. 1975.
- [80] K. Kraus, “General state changes in quantum theory”, en, *Annals of Physics*, vol. 64, no. 2, pp. 311–335, Jun. 1971.
- [81] L. Li, M. J. W. Hall, and H. M. Wiseman, “Concepts of quantum non-Markovianity: A hierarchy”, en, *Physics Reports*, vol. 759, pp. 1–51, Oct. 2018.
- [82] E. B. Davies, “Markovian master equations”, en, *Commun.Math. Phys.*, vol. 39, no. 2, pp. 91–110, Jun. 1974.
- [83] A. G. Redfield, “On the theory of relaxation processes”, *IBM Journal of Research and Development*, vol. 1, no. 1, pp. 19–31, 1957, Publisher: IBM.
- [84] R. Rosati, R. C. Iotti, F. Dolcini, and F. Rossi, “Derivation of nonlinear single-particle equations via many-body Lindblad superoperators: A density-matrix approach”, en, *Phys. Rev. B*, vol. 90, no. 12, p. 125 140, Sep. 2014.
- [85] R. Alicki and J. Messer, “Nonlinear quantum dynamical semigroups for many-body open systems”, *Journal of Statistical Physics*, vol. 32, no. 2, pp. 299–312, 1983.
- [86] Q. Sun and X. Xie, “Definition of the spin current: The angular spin current and its physical consequences”, en, *Phys. Rev. B*, vol. 72, no. 24, p. 245 305, Dec. 2005.
- [87] J. Shi, P. Zhang, D. Xiao, and Q. Niu, “Proper Definition of Spin Current in Spin-Orbit Coupled Systems”, en, *Physical Review Letters*, vol. 96, no. 7, Feb. 2006.
- [88] O. Busch, F. Ziolkowski, I. Mertig, and J. Henk, “Ultrafast dynamics of electrons excited by femtosecond laser pulses: Spin polarization and spin-polarized currents”, *arXiv preprint arXiv:2303.09291*, 2023.

- [89] D. Pescia, G. Zampieri, M. Stampanoni, G. L. Bona, R. F. Willis, and F. Meier, “Ferromagnetism of thin epitaxial fcc cobalt films on Cu(001) observed by spin-polarized photoemission”, en, *Physical Review Letters*, vol. 58, no. 9, pp. 933–936, Mar. 1987.
- [90] M. Singh, C. Wang, and J. Callaway, “Spin-orbit coupling, fermi surface, and optical conductivity of ferromagnetic iron”, *Physical Review B*, vol. 11, no. 1, p. 287, 1975.
- [91] C. Barreteau, D. Spanjaard, and M.-C. Desjonquères, “An efficient magnetic tight-binding method for transition metals and alloys”, en, *Comptes Rendus Physique*, vol. 17, no. 3-4, pp. 406–429, Mar. 2016.
- [92] J. Chen, U. Bovensiepen, A. Eschenlohr, T. Müller, P. Elliott, E. K. U. Gross, J. K. Dewhurst, and S. Sharma, “Competing Spin Transfer and Dissipation at Co / Cu (001) Interfaces on Femtosecond Timescales”, *Phys. Rev. Lett.*, vol. 122, no. 6, 2019.
- [93] Töws, W., “Many-body theory of laser-induced ultrafast demagnetization and angular momentum transfer in ferromagnetic transition metals”, PhD thesis, Kassel, 2014.
- [94] P. Bogacki and L. F. Shampine, “A 3(2) pair of Runge - Kutta formulas”, en, *Applied Mathematics Letters*, vol. 2, no. 4, pp. 321–325, 1989.
- [95] G. Malinowski, F. Dalla Longa, J. H. H. Rietjens, P. V. Paluskar, R. Huijink, H. J. M. Swagten, and B. Koopmans, “Control of speed and efficiency of ultrafast demagnetization by direct transfer of spin angular momentum”, en, *Nature Physics*, vol. 4, no. 11, pp. 855–858, Nov. 2008.
- [96] D. Rudolf, C. La-O-Vorakiat, M. Battiato, R. Adam, J. M. Shaw, E. Turgut, P. Maldonado, S. Mathias, P. Grychtol, H. T. Nembach, T. J. Silva, M. Aeschlimann, H. C. Kapteyn, M. M. Murnane, C. M. Schneider, and P. M. Oppeneer, “Ultrafast magnetization enhancement in metallic multilayers driven by superdiffusive spin current”, en, *Nature Communications*, vol. 3, no. 1, Jan. 2012.
- [97] E. Turgut, C. La-o-vorakiat, J. M. Shaw, P. Grychtol, H. T. Nembach, D. Rudolf, R. Adam, M. Aeschlimann, C. M. Schneider, T. J. Silva, M. M. Murnane, H. C. Kapteyn, and S. Mathias, “Controlling the Competition between Optically Induced Ultrafast Spin-Flip Scattering and Spin Transport in Magnetic Multilayers”, en, *Phys. Rev. Lett.*, vol. 110, no. 19, p. 197 201, May 2013.
- [98] A. Melnikov, I. Razdolski, T. O. Wehling, E. T. Papaioannou, V. Roddatis, P. Fumagalli, O. Aktsipetrov, A. I. Lichtenstein, and U. Bovensiepen, “Ultrafast Transport of Laser-Excited Spin-Polarized Carriers in Au / Fe / MgO (001)”, en, *Physical Review Letters*, vol. 107, no. 7, Aug. 2011.

- [99] M. Hofherr, S. Häuser, J. K. Dewhurst, P. Tengdin, S. Sakshath, H. T. Nembach, S. T. Weber, J. M. Shaw, T. J. Silva, H. C. Kapteyn, M. Cinchetti, B. Rethfeld, M. M. Murnane, D. Steil, B. Stadtmüller, S. Sharma, M. Aeschliemann, and S. Mathias, “Ultrafast optically induced spin transfer in ferromagnetic alloys”, en, *Sci. Adv.*, vol. 6, no. 3, eaay8717, Jan. 2020.
- [100] F. Willems, C. von Korff Schmising, C. Strüber, D. Schick, D. Engel, J. D., P. Elliott, S. Sharma, and S. Eisebitt, “Optical inter-site spin transfer probed by energy and spin-resolved transient absorption spectroscopy”, en, *Nature Communications*, vol. 11, no. 1, Dec. 2020.
- [101] M. Borchert, C. von Korff Schmising, D. Schick, D. Engel, S. Sharma, and S. Eisebitt, “Manipulation of ultrafast demagnetization dynamics by optically induced intersite spin transfer in magnetic compounds with distinct density of states”, arXiv:2008.12612 [cond-mat], 2020.
- [102] V. P. Zhukov, E. V. Chulkov, and P. M. Echenique, “Lifetimes and inelastic mean free path of low-energy excited electrons in Fe, Ni, Pt, and Au: *Ab initio* GW + T calculations”, en, *Physical Review B*, vol. 73, no. 12, Mar. 2006.
- [103] F. Ziolkowski, O. Busch, I. Mertig, and J. Henk, “Ultrafast spin dynamics: Complementing theoretical analyses by quantum state measures”, *J. Phys.: Condens. Matter*, Jan. 2023.
- [104] R. Rouzegar, L. Brandt, L. Nádvorník, D. A. Reiss, A. L. Chekhov, O. Gueckstock, C. In, M. Wolf, T. S. Seifert, P. W. Brouwer, G. Woltersdorf, and T. Kampfrath, “Laser-induced terahertz spin transport in magnetic nanostructures arises from the same force as ultrafast demagnetization”, en, *Phys. Rev. B*, vol. 106, no. 14, p. 144427, Oct. 2022.
- [105] *The Elk Code*, <http://elk.sourceforge.net/>.
- [106] R. I. Herapath, S. M. Hornett, T. S. Seifert, G. Jakob, M. Kläui, J. Bertolotti, T. Kampfrath, and E. Hendry, “Impact of pump wavelength on terahertz emission of a cavity-enhanced spintronic trilayer”, en, *Applied Physics Letters*, vol. 114, no. 4, p. 041107, Jan. 2019.
- [107] R. Beigang, E. Papaioannou, L. Scheuer, S. Keller, G. Torosyan, M. Rahm, D. Sokoluk, M. Talara, Y. Oda, H. Kitahara, J. Afalla, V. K. Mag-usara, and M. Tani, “Efficient terahertz generation using Fe/Pt spintronic emitters pumped at different wavelengths”, in *Terahertz, RF, Millimeter, and Submillimeter-Wave Technology and Applications XII*, L. P. Sadwick and T. Yang, Eds., San Francisco, United States: SPIE, Mar. 2019, p. 23.
- [108] A. Chekhov, Y. Behovits, J. Heitz, C. Denker, D. Reiss, M. Wolf, M. Weinelt, P. Brouwer, M. Münzenberg, and T. Kampfrath, “Ultrafast Demagnetization of Iron Induced by Optical versus Terahertz Pulses”, en, *Phys. Rev. X*, vol. 11, no. 4, p. 041055, Dec. 2021.

- [109] A. Jain, S. Ong, G. Hautier, W. Chen, W. Richards, S. Dacek, S. Cholia, D. Gunter, D. Skinner, G. Ceder, and K. Persson, “Commentary: The Materials Project: A materials genome approach to accelerating materials innovation”, *APL Materials*, vol. 1, no. 1, p. 011002, Jul. 2013. eprint: https://pubs.aip.org/aip/apm/article-pdf/doi/10.1063/1.4812323/13163869/011002_1_online.pdf.
- [110] M. N. Polyanskiy, *Refractive index database*, <https://refractiveindex.info>, Accessed on 2022-10-21.
- [111] P. B. Johnson and R. W. Christy, “Optical constants of transition metals: Ti, v, cr, mn, fe, co, ni, and pd”, *Phys. Rev. B*, vol. 9, pp. 5056–5070, 12 Jun. 1974.
- [112] M. E. Rose, “Relativistic Electron Theory”, en, *American Journal of Physics*, vol. 29, no. 12, pp. 866–866, Dec. 1961.
- [113] R. Fisher, “Proceedings of the royal society of london. series a”, *Mathematical and Physical Sciences.*, vol. 217, no. 1130, p. 295, 1953.
- [114] D. Whittenbury, *von-Mises-Fisher-Sampling*, <https://github.com/dlwhittenbury/von-Mises-Fisher-Sampling>; (25.11.2022).
- [115] J. Crangle and G. M. Goodman, “The magnetization of pure iron and nickel”, *Proceedings of the Royal Society of London. A. Mathematical and Physical Sciences*, vol. 321, no. 1547, pp. 477–491, 1971.
- [116] T. Roth, A. J. Schellekens, S. Alebrand, O. Schmitt, D. Steil, B. Koopmans, M. Cinchetti, and M. Aeschlimann, “Temperature Dependence of Laser-Induced Demagnetization in Ni: A Key for Identifying the Underlying Mechanism”, en, *Physical Review X*, vol. 2, no. 2, May 2012.
- [117] G. P. Zhang, Y. H. Bai, and T. F. George, “Ultrafast reduction of exchange splitting in ferromagnetic nickel”, *J. Phys.: Condens. Matter*, vol. 28, no. 23, p. 236004, Jun. 2016.
- [118] O. Busch, F. Ziolkowski, I. Mertig, and J. Henk, “Ultrafast dynamics of electrons excited by femtosecond laser pulses: Spin polarization and spin-polarized currents”, *arXiv preprint arXiv:2303.09291*, 2023.
- [119] O. Busch, F. Ziolkowski, I. Mertig, and J. Henk, “Ultrafast dynamics of orbital angular momentum of electrons induced by femtosecond laser pulses: Generation and transfer across interfaces”, *Phys. Rev. B*, vol. 108, p. 104408, 10 Sep. 2023.

List of publications

- [F1] F. Töpler, A. Hönemann, K. Tauber, D. V. Fedorov, M. Gradhand, I. Mertig, and A. Fert, “Nonlocal anomalous hall effect in ternary alloys based on noble metals,” *Physical Review B*, vol. 94, no. 14, Oct. 19, 2016.
- [F2] V. Popescu, P. Kratzer, P. Entel, C. Heiliger, M. Czerner, K. Tauber, F. Töpler, C. Herschbach, D. V. Fedorov, M. Gradhand, I. Mertig, R. Kováčik, P. Mavropoulos, D. Wortmann, S. Blügel, F. Freimuth, Y. Mokrousov, S. Wimmer, D. Ködderitzsch, M. Seemann, K. Chadova, and H. Ebert, “Spin caloric transport from density-functional theory,” *Journal of Physics D: Applied Physics*, vol. 52, no. 7, p. 073 001, Feb. 13, 2019.
- [F3] T. Rauch, F. Töpler, and I. Mertig, “Local spin hall conductivity,” *Phys. Rev. B*, vol. 101, p. 064 206, 6 Feb. 2020.
- [F4] F. Töpler, J. Henk, and I. Mertig, “Ultrafast spin dynamics in inhomogeneous systems: A density-matrix approach applied to Co/Cu interfaces,” *New J. Phys.*, vol. 23, no. 3, p. 033 042, Mar. 2021.
- [F5] F. Ziolkowski, O. Busch, I. Mertig, and J. Henk, “Ultrafast spin dynamics: Complementing theoretical analyses by quantum state measures,” *J. Phys.: Condens. Matter*, Jan. 2023.
- [F6] O. Busch, F. Ziolkowski, I. Mertig, and J. Henk, “Ultrafast dynamics of electrons excited by femtosecond laser pulses: Spin polarization and spin-polarized currents,” *Physical Review B*, vol. 108, no. 18, p. 184 401, Nov. 2, 2023.
- [F7] O. Busch, F. Ziolkowski, I. Mertig, and J. Henk, “Ultrafast dynamics of orbital angular momentum of electrons induced by femtosecond laser pulses: Generation and transfer across interfaces,” *Phys. Rev. B*, vol. 108, p. 104 408, 10 Sep. 2023.
- [F8] O. Busch, F. Ziolkowski, B. Göbel, I. Mertig, and J. Henk, “Ultrafast orbital hall effect in metallic nanoribbons,” *arXiv preprint arXiv:2307.08444*, 2023.

Curriculum vitae

Personal data

name Franziska Ziolkowski geb. Töpler

Education

1999-2003 Heinz-Sielmann-Grundschule Niedersachswerfen
2003-2011 Wilhelm-von-Humboldt-Gymnasium Nordhausen
2011-2012 European Voluntary Service in Białystok, Poland
2012-2015 Studies of Physics at Martin-Luther-Universität Halle-Wittenberg,
Bachelor of Science in Physics, thesis: “Der anomale Hall-Effekt in
ternären Legierungen”
2015-2018 Studies of Physics at Martin-Luther-Universität Halle-Wittenberg,
Master of Science in Physics, thesis: “Der Einfluss von Grenzflächen
auf den Spin-Hall-Effekt”
since 08/2018 PhD studies at Martin-Luther-Universität Halle-Wittenberg
10/2021-09/2022 parental leave

Academic work experience

2015-2018 Student assistant, Institutes of Mathematics and Physics
since 08/2018 Research assistant Institute of Physics MLU, CRR 227

Scholarships and awards

2011 Abitur award of DPG
2012-2018 Scholarship of Studienstiftung des deutschen Volkes
2015-2017 Gustav Mie Bachelor award of the Institute of Physics, MLU

Acknowledgements

Whilst writing this acknowledgements I am not only looking back on the time of my PhD but on my entire time in the group of *Quantum Theory of the Solid State*, on my time of studying physics at the Martin-Luther-Universität Halle-Wittenberg.

I am grateful for all the inspiring people that accompanied me along this way: my friends and my family as well as my colleagues and tutors. They influenced my development, enriched my life and were pleasant and amusing company.

First of all I want to thank Ingrid who provided the formal frame and found interesting as well as challenging topics in connection with various theoretical methods for my scientific work. Her style of thorough and detailed discussion taught me to analyze my results in a fundamental way and from a broader view.

Beginning with my Bachelor thesis a long list of skillful and capable advisors introduced me to the work of a scientist; from careful analysis of data, appropriate graphical and textual presentation of results to scientific talks. I want to thank especially Jürgen for his initial ideas and computational support that brought this project to life. He has always inspirations for new promising directions of investigation.

Equally I want to thank my colleagues and office mates Albert, who reviewed my manuscript, and Thorsten, as well as Paul and Duc for the sweet supply and Micha and Nicki who provided the freshest news about our institute. Likewise I thank all the other group members for interesting discussions in our coffee breaks and seminars.

During my PhD time two big changes occurred: First Covid changed our working style and working habits. The second was a more joyful change in my private life: the birth of my son.

I am thankful that throughout these changes the work on my PhD could continue in a good way, that I could resume my work after one year of parental leave and that this job provides me the flexibility that is needed for a life with a child.

Eidesstattliche Erklärung

Hiermit erkläre ich an Eides statt, dass ich die vorliegende Arbeit

**Modelling ultrafast demagnetization:
A real-space tight-binding approach**

selbstständig und ohne fremde Hilfe verfasst, keine anderen als die von mir angegebenen Quellen und Hilfsmittel benutzt und die den benutzten Werken wörtlich oder inhaltlich entnommenen Stellen als solche kenntlich gemacht habe. Desweiteren erkläre ich, dass ich die Angaben wahrheitsgemäß gemacht und weder diese noch eine andere Dissertation an einer anderen wissenschaftlichen Einrichtung zur Erlangung eines akademischen Grades eingereicht habe.

Halle (Saale), 21. Juni 2024
Franziska Ziolkowski